UNIVERSITY OF CALIFORNIA
Santa Barbara

Pushing the envelope of magnetic tweezer resolution

A Dissertation submitted in partial satisfaction
of the requirements for the degree of

Doctor of Philosophy

in

Materials

by

Bob Lansdorp

Committee in Charge:

Professor Omar A. Saleh, Chair

Professor Cyrus R. Safinya

Professor Jacob N. Israelachvili

Professor Everett A. Lipman

March 2016

The Dissertation of
Bob Lansdorp is approved:

Professor Cyrus R. Safinya

Professor Jacob N. Israelachvili

Professor Everett A. Lipman

Professor Omar A. Saleh, Committee Chairperson

December 2015

Pushing the envelope of magnetic tweezer resolution

by

Bob Lansdorp

I would like to dedicate this thesis to my parents for showing that big risks can reap big rewards, and to Olga for being a great sister.

Acknowledgements

First of all, I would like to acknowledge my advisor, Professor Omar Saleh for making this thesis possible. His organization of the group into independent but related projects, his in-depth chalk-board lectures, and seemingly infinite patience with my project have been both a fantastic learning experience and an enjoyable one.

The Saleh Lab members have been great collaborators and friends: John Berezney, Olivier Bertrand, Andrew Dittmore, Dan Nguyen, Dustin McIntosh, Noah Ribeck, Jun Lin, Shawn Tabrizi, David Jacobson, and Chang-Young Park. Thanks to former lab members Noah Ribeck and Kipom Kim for leaving their work well-documented. The weekly group meetings with Professor Valentine and her group members Dezhi Yu, Burgra Katanyi, Ben Lopez and Jamie Wilcox were a stimulating source of ideas, as well as fruitful discussions. Thanks to Zachary Hockenbery for simulating magnets in COMSOL.

Thank you to the UCSB Materials Department Staff who have been very kind and helpful: Tawny Hernandez, Jocelyn Guzman, and Oura Neak, and Budd Jamieson.

I'd like to acknowledge Andy Weinberg in the COE machine shop, who has been incredibly generous with his time and expertise, as well as being one of the most friendly people I have met at UCSB.

Brian Thibeault helped design the Pt deposition for a spatial filter, and Jeff Dutter in UCSB Physics machine shop helped manufacture the copper cooling blocks.

A big thanks to Professor Sumita Pennathur and Tom Wynne for use of their high-speed CMOS (hs-CMOS) cameras during my first year. Without a high-speed camera, I don't know where my thesis would be today!

I would like to thank the Canadian taxpayers and government for awarding me an NSERC-PGSD fellowship to pursue my studies at UCSB. I hope to be able to repay you one day for your investment in me. I'd also like to thank the UCSB Graduate Division for the financial support in the form of a Fellowship, but also for hosting the Grad Slam.

And last but not least, I'd like to thank my wonderful girlfriend Fernanda Henderikx Freitas, who has been an infinite source of happiness and inspiration during our many coffee breaks.

Abstract

Pushing the envelope of magnetic tweezer resolution

Bob Lansdorp

The magnetic tweezer is a single molecule instrument that can measure the extension of biomolecules by tracking tethered probe particles. Due to its experimental simplicity and ability to apply a constant external force to probe particles, the magnetic tweezer is ideally suited to measuring single molecule dynamics under applied tension. In this thesis, I push the resolution of magnetic tweezers to angstrom spatial resolution by using a high-speed camera which can achieve more than 10 kHz temporal resolution.

I investigate the fundamental limits to magnetic tweezer resolution from basic principles, and investigate different types of light coherence to arrive on a new choice of light source for the magnetic tweezer: the superluminescent diode. I explore Langevin dynamics of tethered probe particles using the Allan variance, a more intuitive take on thermal fluctuations than the Power Spectral Density. I push the achievable resolution limits by using smaller beads, introduce higher gradient magnets to apply biologically relevant forces on these smaller beads, and introduce a Fourier filter system to achieve higher spatial resolution.

Contents

Chapter 1

Introduction

> *Nothing tends so much to the advancement of knowledge as the application of a new instrument.* -Sir Humphry Davy, 1812

Single-molecule manipulation (SMM) instruments such as the magnetic tweezer, optical tweezer, and atomic force microscope (AFM) measure individual biomolecules and their interactions with salt, proteins, and other molecules. [1–3] The development of high-resolution SMM instruments, in particular optical tweezers with sub-nanometer resolution at a bandwidth of hundreds of hertz, has catalyzed the discovery of many new bio-physical phenomena. [4–9] New instrumental techniques that allow for the measurement of many molecules in parallel with improved accuracy will continue to provide insights into the nature of biological machines at the nanoscale. [10, 11] In this thesis, I aim to determine the fundamental limits to one such instrument, the magnetic tweezer, in the pursuit of the ultimate instrumental resolution.

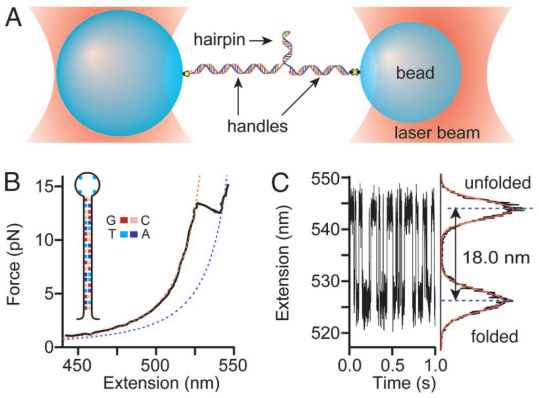

Figure 1.1: Optical tweezer measurements can reveal the force-extension and hopping behavior of single DNA hairpins [12]

Optical and magnetic tweezers can be contrasted in how they apply force to probe particles. Whereas an optical tweezer typically traps a probe particle in an energetic potential well, a magnetic tweezer applies a constant force to the probe particle, even as the particle moves through space. A constant force avoids complications arising from changes to the potential energy landscape that are generated by molecular motions against a changing load. [13] Furthermore, since the bead displacement signal-to-noise ratio is independent of trapping stiffness, [14] a constant force instrument can measure single molecule activity without the added complication of careful alignment to an anharmonic region of the optical trap [13, 15] or feedback control [16] to keep the anharmonic region centered on the bead for dynamic systems. Although the magnetic tweezer has traditionally been the lower-resolution companion to the optical tweezer [2] it could rival the

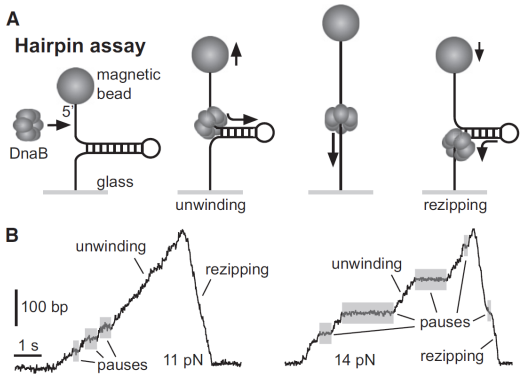

Figure 1.2: Magnetic tweezer measurements can reveal helicase activity on DNA hairpins [11]

optical tweezer if the spatial and temporal resolution of the magnetic tweezer could be improved.

Both optical and magnetic tweezers use beads to measure the position of probe particles. The approximately micron-sized probe particles used undergo diffusive (Brownian) motion at short time scales that obscure the underlying molecular motion, resulting in a thermal source of noise. Thermal noise can be minimized for an instrument of a given bandwidth by using small beads with lower drag coefficients, and higher stiffness tethers [14].

In addition to thermal noise, there is also instrument noise in a magnetic tweezer. The first type of instrument noise that is encountered at the shortest time-scales is the shot-noise caused by the quantized nature of photon detection which results in a per-frame tracking error between actual bead position and measured bead position. Attempts have been made to increase the spatial resolution of the magnetic tweezer using specially coated beads (see Figure 1.3), but

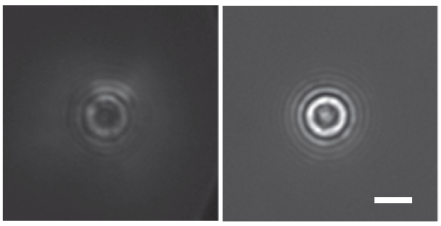

Figure 1.3: The addition of metal coatings to magnetic beads enhances contrast for improved particle tracking resolution [17]

these attempts have thus far been incapable of the low thermal noise required of high-resolution tracking because the coatings were incompatible with small magnetic beads due to a higher relative surface roughness to bead diameter of smaller beads. [17] Sensitivity to thermal noise beyond the Nyquist frequency is possible using strobed light sources; [18] however, for non-stationary processes such as motor protein stepping, light strobing cannot be used to artificially enhance the data acquisition rate. Therefore, what is desired is a means of high per-frame tracking resolution that is also compatible with the small beads. In this thesis I examine the theoretical limits to particle tracking and introduce a spatial-filter system that improves the per-frame tracking error.

At longer timescales ($t \approx 0.01$ s), mechanical vibration of the sample stage starts to become significant. In this thesis, I add a mechanically rigid sample stage with a tube-lens focus system to replace the conventional piezoelectric objective focusing system to reduce mechanical vibration and still allow for the creation of calibration images used in particle tracking.

At yet longer timescales ($t \approx 0.1$ s) drift due to thermal expansion of components becomes significant. In addition to mechanically moving the particle, low frequency drift of optical components creates a low-frequency speckle noise: a slow modulation of speckle patterns on the image detector which interferes with particle tracking. To reduce speckle in video-based particle tracking, experimentalists have utilized a variety of illumination sources including thermal light sources [19] to pulsed laser diodes [20]. In this thesis, I examine the physical basis for speckle from an examination of both spatial and temporal coherence. I use a superluminescent diode, which provides sufficient light for high-speed tracking and has reduced temporal coherence, but concede that there is room for improvement in the development of a light source with reduced spatial coherence.

To quantify the improvements to instrumental resolution, I make use of the Power Spectral Density (PSD) and Allan Variance [21]. In addition to quantifying the instrumental noise, the PSD can be used to quantify the motion of bead particles, from purely diffusive at high frequencies to sampling the potential well at lower frequencies, in a functional form that can be described by a Lorentzian. I will show that a similar expression can be derived for the Allan variance. The analytical expressions for bead particle motion can be fit to experimental data using maximum likelihood estimation.

The recent introduction of high-speed cameras to particle tracking [19, 22–24] has opened the door to a new field of video-based single-molecule manipulation

that can obtain high spatial and temporal resolution. In this thesis, I replace the conventional 60 Hz CCD with a hs-CMOS camera. I use the high-speed magnetic tweezer to demonstrate spatial resolution and bandwidth comparable to a high-resolution optical tweezer instrument.

Chapter 2

Physical limits to particle tracking resolution

In this chapter, I discuss the limits to particle tracking resolution, starting from general physical principles and developing into applied results specific to the magnetic tweezer.

2.1 Optical sensing principle

The magnetic tweezer is a digital inline holographic microscope [25] with added magnets. A collimated reference beam of light creates a planar reference wave on the image plane. Bead particles in this reference beam scatter light, and the resulting interference pattern between the reference and scattered waves is what gives rise to diffraction patterns. A typical image is shown in Figure 2.1.

The lateral (x,y) position of the bead can be determined with sub-pixel accuracy by cross-correlating the diffraction pattern [26]. The vertical position of the bead (z) is detected by interference between the scattered light and the unscattered reference light which creates an radial intensity pattern that is a function of defocus distance z.

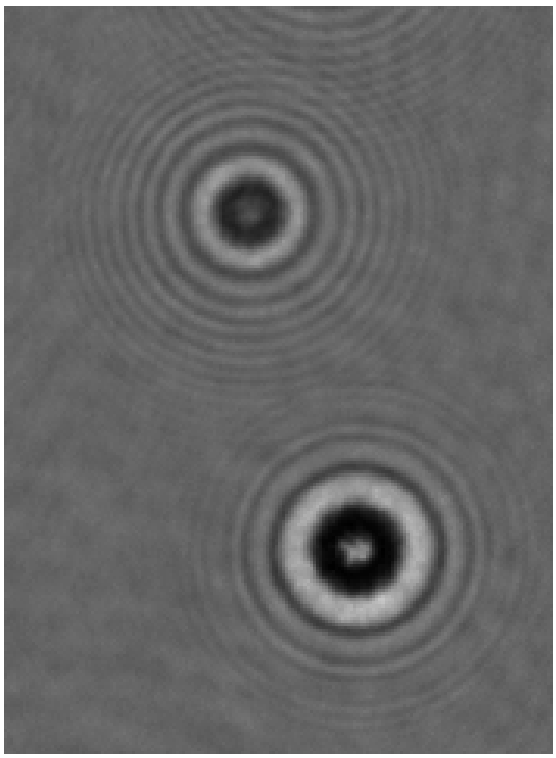

Figure 2.1: A typical bright-field normalized image of a bead. Imaged using superluminescent diode illumination, a 1.05 μm diameter Myone bead and partially molten "stuck" reference 2.8 μm diameter bead

The amplitude and phase of scattered light is a function of the relative sizes of the bead and the wavelength of light. In magnetic tweezers, the typical 1.05 μm

diameter beads are comparable to the 638 nm wavelength of light, and as a result, complete Lorenz-Mie theory must be used to accurately predict the amplitude and phase of scattered light as a function of scatter angle [25]. Lorenz-Mie simulations originally written in IDL programming language [27] were translated into C programming language [28]. The C program can generate simulated bead images given starting parameters such as bead refractive index, wavelength of light, magnification, and defocus distance.

2.2 Standard quantum limit

A single photon emitted at a point source and imaged by a microscope will create an Airy diffraction pattern on the detector, and criteria such as the Rayleigh criterion are often used to characterize the accuracy with which two points of unknown amplitude can be discerned. In a magnetic tweezer, isolated beads are imaged, and this is not a relevant method for quantifying the accuracy with which a particle position can be resolved.

In a typical magnetic tweezer experiment, a 150 μm diameter collimated beam of light with 2 mW of power is incident on the focal plane, where a 1 μm diameter bead (with an optical scattering cross section [29] of approximately 1.7 μm^2) will scatter approximately 10^{-7} W of light.

If we consider the scattered wave as interfering with a reference wave in a one-dimensional interferometer, then the accuracy of particle tracking resolution

can be quantified by the standard quantum (shot noise) limit:

$$\Delta\phi = \frac{1}{\sqrt{N}} \tag{2.1}$$

$$\Delta x = \frac{\lambda}{2\pi\sqrt{N}} \tag{2.2}$$

For light of wavelength $\lambda = 600$ nm, with a scattered power of 1×10^{-7} W (with $hc/\lambda = 3.3 \times 10^{-19}$ J/photon) we have $N = 3 \times 10^{11}$ photons/s. Plugging in for the quantum limited spatial resolution, we have:

$$\Delta x = \frac{\lambda}{2\pi\sqrt{N}} = 1.7 \times 10^{-13}\ \mathrm{m}/\sqrt{\mathrm{Hz}} \tag{2.3}$$

In terms of variance, this is: $(\Delta x)^2 \geq 3 \times 10^{-8}\ \mathrm{nm}^2/\mathrm{Hz}$, which is the noise floor in the standard quantum limit of a one-dimensional interferometer in the conditions described above. However, as we will show, not all photons are contributing optimally to the signal of particle position.

2.3 The Rayleigh limit of Lorenz-Mie Scatter

Although it is possible to use the intensity of scattered light alone to detect the height of the bead [30], by combining the scattered wave with a reference wave, we can obtain an improved measurement of the bead height by the optical interference between the scattered light and the reference wave. In the following, I will show how the use of an on-axis reference wave greatly improves the resolution of particle tracking on-axis through more efficient use of photons.

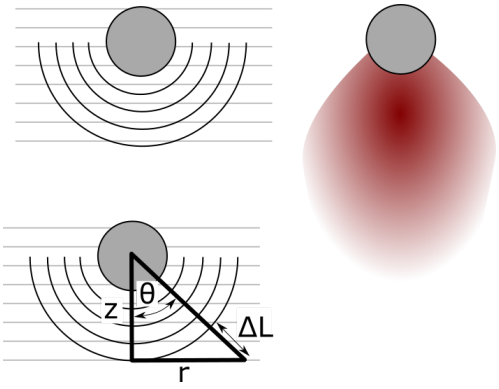

Figure 2.2: The phase and amplitude of beads due to Lorenz-Mie scatter, in the limit of beads much smaller than the wavelength

If we imagine that the sole function of a camera pixel is to determine the axial position of a bead by means of the scattered light interference pattern, then we can define an efficiency with which the pixel intensity conveys information of bead height as compared to a theoretically ideal interferometric measurement. The mechanism by which magnetic tweezers detect the vertical position of the bead can be conceptualized most easily in the limit of a bead with radius much smaller than the wavelength of light, where the amplitude from Lorenz-Mie theory reduces to Rayleigh theory, and goes as [31]:

$$I_s \propto (1 + cos^2(\theta)) = 1 + \frac{1}{1 + \frac{r^2}{z^2}} \tag{2.4}$$

The intensity of the electric field at a detector at axial distance z and radial distance r decays as the inverse squared distance:

$$I_s \propto \frac{1}{z^2 + r^2} \tag{2.5}$$

Combining the two scaling arguments gives:

$$I_s \propto \frac{1}{z^2 + r^2}\left(1 + \frac{1}{1 + \frac{r^2}{z^2}}\right) \tag{2.6}$$

The intensity of the detected signal is related to the electric fields of the reference and scattered signals. $I = |(E_R + E_S)|^2$. The reference beam will take the form of a planar wave, and the scattered wave will take the form dictated by Lorenz-Mie scatter, in this section approximated by Rayleigh scatter. Assuming that the phase of scattered light does not vary with scatter angle, and ignoring rotation of polarization, the intensity at the detector is:

$$I = |(E_0 + E_S)|^2 = \left| A_R e^{i(\omega t + kz)} + A_S e^{i(\omega t + k\sqrt{r^2+z^2})} \frac{\sqrt{2 + r^2/z^2}}{\sqrt{1 + r^2/z^2}} \frac{1}{\sqrt{r^2 + z^2}} \right|^2 \tag{2.7}$$

Figure 2.3 shows the intensity of light at a detection distance z at a radial coordinate r, with and without a planar reference wave which illustrates how the addition of a reference wave modulates the intensity pattern of scattered light. For simplicity, I chose a constant amplitude reference wave with $E_R = E_S = 1$.

Both the reference wave and the scattered wave will be time-varying electromagnetic fields with a phase factor of $e^{i\omega t}$, where ω is the angular frequency of the light. Since the angular frequency of light is much greater than the camera frequency, and ignoring the phase shift of scattered light, the magnetic tweezer takes the average interference pattern over many optical cycles and the intensity is:

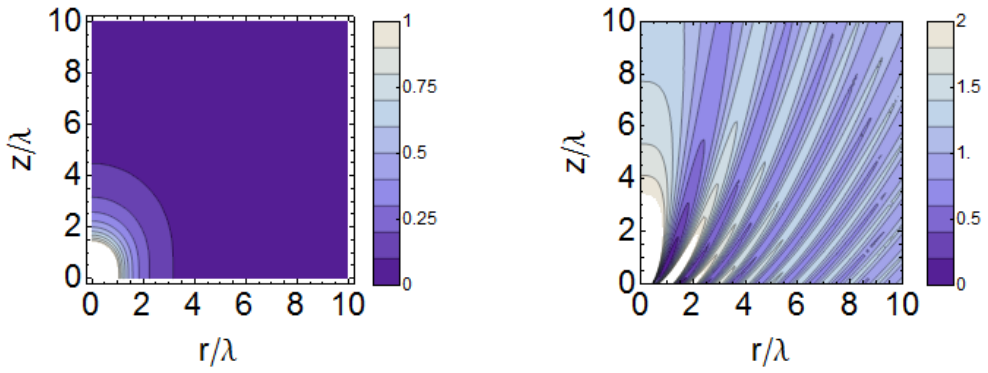

(a) without a reference wave (b) with a planar reference wave

Figure 2.3: The intensity I(r,z) as a function of defocus distance z and radial coordinate r for a particle with radius much smaller than the wavelength of light (Rayleigh scatter)

$$I = \left| A_R e^{ikz} + A_S e^{ik\sqrt{r^2+z^2}} \frac{\sqrt{2+r^2/z^2}}{\sqrt{1+r^2/z^2}} \frac{1}{\sqrt{r^2+z^2}} \right|^2 \tag{2.8}$$

There are two special cases that simplify this equation and are of relevance to the discussion of resolution in magnetic tweezers: no reference wave, and when the amplitude of the reference wave matches the amplitude of the scattered wave on the plane of the detector. We can compare these two cases with an ideal 1D Michelson-type interferometer with amplitude matched beams, where the change in intensity of light is most strongly dependent on distance at a 90 degree phase offset between object and reference wave, and intensity goes as $\frac{\partial I_{actual}}{\partial z} = \frac{2\pi I}{\lambda}$. The sensitivity of intensity change to bead distance can also be increased to $4\pi I/\lambda$ when back-scattered detection is employed and the relative path-length difference between reference and scattered light doubles per unit of bead motion. [17]

2.3.1 No reference wave

In the absence of a reference wave, we cannot measure the phase of the scattered light, and all we measure is the intensity of the scattered wave $I_{scat} = |E_S|^2$. In this case, we can define an efficiency of detection η by comparing change in intensity as compared to a 1-D interferometer of equal amplitude, where intensity vs distance would vary as $2\pi I/\lambda$:

$$\eta = \frac{\partial I_{scat}}{\partial z} / \frac{\partial I_{ideal}}{\partial z} = \frac{\partial I_{scat}}{\partial z} / \frac{2\pi I_{scat}}{\lambda} \tag{2.9}$$

With the scatter pattern given by Equation 2.7, we can solve for efficiency of height detection in the absence of a reference wave:

$$\eta_{no\_ref} = \frac{2\lambda}{\pi z}\left(\frac{1}{(r/z)^4 + 3(r/z)^2 + 2}\right) \tag{2.10}$$

This is the efficiency of a detector in estimating height of a bead much smaller than the wavelength of light, as compared to an ideal 1-D inteferometer with the same number of photons.

2.3.2 Amplitude matched reference wave

In the case where the reference wave amplitude is matched to the scatter wave amplitude on the focal plane:

$$I_{scat,ref} = \left| E_R e^{ikz} + E_S e^{ik\sqrt{r^2+z^2}} \frac{\sqrt{2 + r^2/z^2}}{\sqrt{1 + r^2/z^2}} \frac{1}{\sqrt{r^2 + z^2}} \right|^2 \tag{2.11}$$

$$I_{scat,ref} = E_S^2 \frac{(2 + r^2/z^2)}{(1 + r^2/z^2)(r^2 + z^2)} \left| e^{ikz} + e^{ik\sqrt{r^2+z^2}} \right|^2 \tag{2.12}$$

Solving for $\eta = |\frac{\partial I_{scat,ref}}{\partial z}| / \frac{2\pi(2I_{scat})}{\lambda}$, we can obtain the efficiency of photons, where the extra factor of 2 accounts for the fact that the reference beam has the same amplitude as the scattered beam. If we further assume that the reference wave amplitude is equal everywhere in amplitude to the scattered wave, we can obtain:

$$\eta_{explicit} = \frac{2}{k(r^2 + z^2)^{3/2}(r^2 + 2z^2)} (4z^3\sqrt{r^2 + z^2}\cos^2[k/2(z - \sqrt{r^2 + z^2})]$$

$$+k(r^4 + 3r^2z^2 + 2z^4)(-z + \sqrt{r^2 + z^2})\cos(k/2(z - \sqrt{r^2 + z^2}))\sin(k/2(z - \sqrt{r^2 + z^2})))$$

(2.13)

In reality, it is impossible to have a reference wave amplitude that matches the scattered wave amplitude everywhere, but this gives an upper bound of the efficiency of photon detection, and illustrates the efficiency of photons at higher angles.

Replacing $\cos^2(k/2(z - \sqrt{r^2 + z^2}))$ with an envelope of 1, and $\cos(k/2(z - \sqrt{r^2 + z^2}))\sin(1/2k(z - \sqrt{r^2 + z^2}))$ with 1/2 to obtain the general trend rather than the specific oscillations, we get:

$$\eta_{envelope} = 2 \left| \frac{(4z^3\sqrt{r^2 + z^2} + k/2(r^4 + 3r^2z^2 + 2z^4)(-z + \sqrt{r^2 + z^2})}{k(r^2 + z^2)^{3/2}(r^2 + 2z^2)} \right| \tag{2.14}$$

We can also use a more intuitive geometric argument to arrive at a similar result. Using simple trigonometry in Figure 2.2, the change in the relative phase

between scatter and reference light with respect to height is:

$$\frac{\partial \phi_{actual}}{\partial z} = 2\pi/\lambda \frac{\partial \Delta L}{\partial z} = \frac{2\pi}{\lambda}\left(\sqrt{1+\frac{r^2}{z^2}} - 1\right) \tag{2.15}$$

Defining $\eta = \frac{\partial \phi_{actual}}{\partial z} / \frac{\partial \phi ideal}{\partial z}$, the relative accuracy with which phase can be detected as a function of r when the amplitude of the reference beam matches the amplitude of the scattered light is equal to:

$$\eta_{phase} = 1 - 1/\sqrt{1+\left(\frac{r}{z}\right)^2} \tag{2.16}$$

The results of the analytically tractable bead scatter efficiency simulations are summarized in Figure 2.4, and demonstrate that using an amplitude-matched reference beam $\eta_{explicit}$ is a relatively efficient way to measure height of the bead, especially when compared with simple scatter detection η_{no_ref}. The efficiency parameters in equations 2.13, 2.14, and 2.16 assume that the reference wave amplitude is exactly matched to the scatter wave amplitude. In reality, this is impossible to achieve simultaneously for all scatter angles, since bead scatter amplitude will vary with angle. The beads used in typical experiments (radius comparable to wavelength of light), more light is scattered in the forward direction than is predicted by Rayleigh theory, and thus the majority of the scattered light is contained in the less-efficient small-angle pixels where intensity does not vary strongly with bead defocus distance.

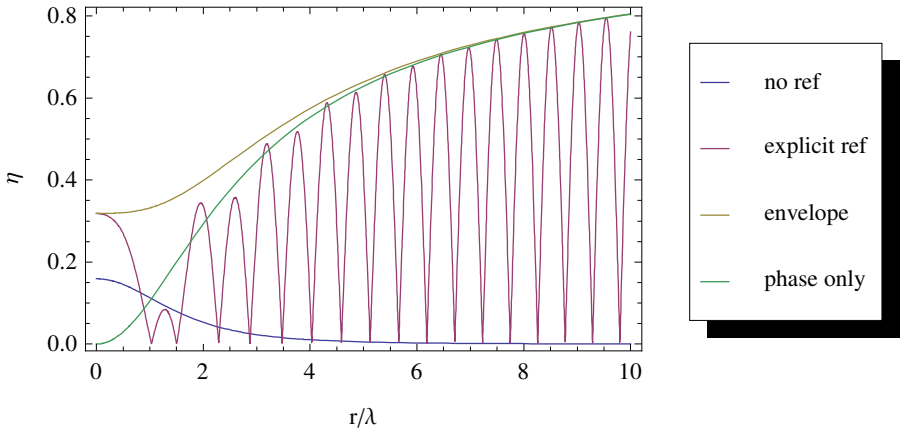

Figure 2.4: The efficiency of scattered photons in detecting height of the bead at $z = 2\lambda$

2.4 Photon radiation Pressure

The use of photons to detect the position of an object with a finite mass results in a recoil effect, where each photon imparts some momentum onto the probe particle. As more photons are used to determine the particle position, the particle momentum becomes more uncertain. In gravity wave detectors [32], this source of noise on the mirrors used is known as radiation pressure and has been shown to cause force fluctuations on the order of:

$$\frac{F^2}{\delta f} = \frac{4I_0 h}{\lambda c} \tag{2.17}$$

For a typical magnetic tweezer experiment with scattered light intensity $I_0 = 1^{-7}$ W, and wavelength $\lambda = 600$ nm,

$$\frac{F^2}{\delta f} = \frac{4I_0 h}{\lambda c} = \frac{4 \times 1 \times 10^{-7}\ \text{W} \times 6.6 \times 10^{-34}\ \text{Js}}{600\ \text{nm} \times 3 \times 10^{8}\ \text{m/s}} = 1.5 \times 10^{-42}\ \text{N}^2/\text{Hz} \tag{2.18}$$

We will show that this force noise caused by collisions with detection photons is approximately 13 orders of magnitude lower than the force noise due to collisions of typical magnetic beads with their surrounding water molecules. Clearly, the magnetic tweezer is not a radiation-pressure limited instrument, and from that perspective, there is plenty of room at the bottom! [33]

2.4.1 Image-based tracking accuracy

We can use a simple approximation to get the theoretical tracking accuracy, similar to a previously published result [34]. If we know the centroid from X,Y tracking, then each individual pixel of a bead image can be used to estimate the z-position of the bead using (Eqn 2.19), where z^* is a first-order estimate of bead position given a nearest neighboring slice z_i

$$z^* = z_i + \frac{\partial z}{\partial I}(I^* - I_i) \tag{2.19}$$

The error in this single-pixel estimate of z is:

$$\Delta z = \frac{\partial z}{\partial I}(\Delta I) \tag{2.20}$$

The variance in height measurement is then:

$$(\Delta z)^2 = \left(\frac{\partial z}{\partial I}\right)^2 (\Delta I)^2 \tag{2.21}$$

We can combine $N \times M$ pixels, each with an independent measurement of z, by weighting them inversely proportional to their variance, in order to yield a net

estimate for the variance in the z estimate:

$$(\Delta z)^2_{net} = \left(\sum_{i=1}^{N} \sum_{i=1}^{M} \left[\left(\frac{\partial z}{\partial I} \right)^2 (\Delta I)^2 \right]^{-1} \right)^{-1} \tag{2.22}$$

If we treat the pixels as a continuum (strictly only valid at large radius), then we can transforming from cartesian (N,M) pixels to polar (r,θ) pixels, we can express the error as:

$$(\Delta z)^2_{net} = \left(\sum_{i=1}^{r} 2\pi r \left[\left(\frac{\partial z}{\partial I} \right)^2 (\Delta I)^2 \right]^{-1} \right)^{-1} \tag{2.23}$$

If we assume that $(\Delta I)^2$ is constant across the field of view and independent of pixel intensity (a good approximation for weakly scattering particles), then we can simplify the theoretical tracking resolution from a calibration stack $I(r, z)$ to:

$$(\Delta z)^2_{net} = \left(\sum_{i=1}^{r} 2\pi r \left(\frac{\partial I}{\partial z} \right)^2 \right)^{-1} (\Delta I)^2 \tag{2.24}$$

2.4.2 Shot Noise

Shot noise is the statistical variation in counting a Poisson process. In the Phantom v7.3 camera that is used, electrons are converted into counts with a precision of 14 bits. When the camera is used in "8-bit" mode, the least significant digits of the 14-bit signals are discarded to yield a net 8-bit precision. The variance of a Poisson process is equal to the mean. For a 14 bit detector at half-max intensity, the shot noise will be $\sigma^2 = N = 2^{14}/2 = 8192$. When

this signal is downsampled from 14 to 8-bit resolution, the resulting variance is: $8192/(2^{14-8})^2 = 2 = \sigma^2_{shot}$.

2.5 Simulated bead tracking error

If we ignore photon shot noise, and assume that $(\Delta I)^2 \approx (0.5)^2$ from the digitization error inherent in an 8-bit image, and apply equation 2.22 to a simulated calibration stack (Figure 2.5), we can estimate the tracking resolution by performing a numerical derivative of adjacent slices. We can also simulate a broad spectral width light source by simply adding the intensity from each wavelength independently. In Figure 2.6 is the simulated per-frame tracking error for three different light sources, all with a central wavelength of 680 nm, but varying spectral widths (6 nm, 600 nm, 1 μm) as a function of out-of-focus depth, with 100nm steps per calibration slice. As one might expect, a narrow spectral width light source has a lower per-frame tracking error, however even a light source with a very large 1 μm spectral width is still trackable to within a reasonable accuracy of 4 nm per frame at a large 4 μm distance. The slices closest to focus have lower tracking error than out-of-focus slices.

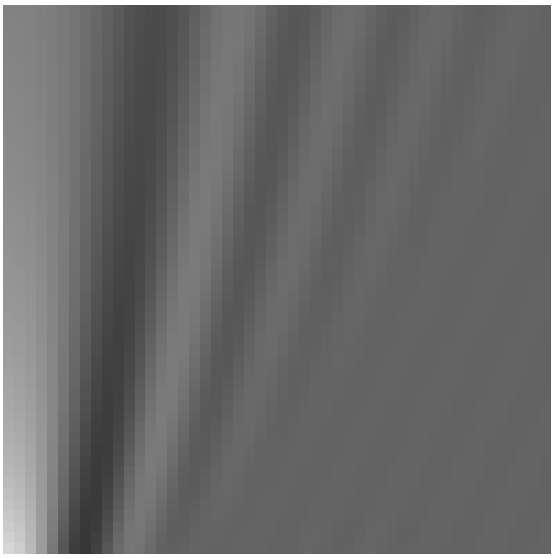

Figure 2.5: A simulated calibration image using a spectral width of 6nm

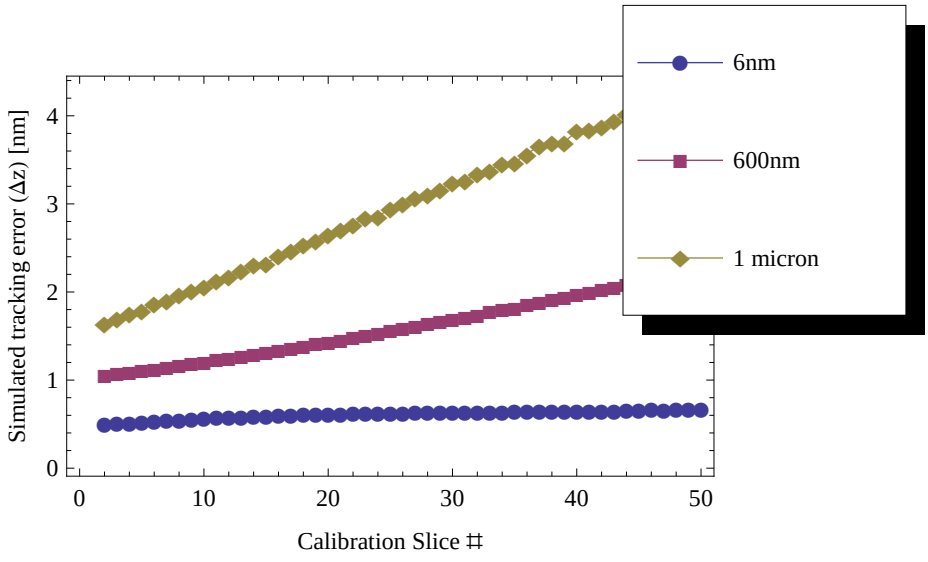

Figure 2.6: Theoretical tracking resolution as a function of calibration image

2.6 Summary

In this chapter, the general principle of on-axis particle tracking is outlined. A reference wave and a scattered wave interfere to cause a radial intensity on the detector that changes with bead height. Exact solutions are found in the limit of beads much smaller than the wavelength (Rayleigh scatter). I have shown that large radial distance pixels more efficiently convey height information of tracked beads, due to large phase difference between the scattered wave and the reference wave at larger radial distances. In subsequent chapters, I will apply these results towards improving the per-frame tracking error by tuning the relative intensity of the reference wave and scattered wave.

Chapter 3

Resolution limits through interactions with the fluid

In this chapter, based largely on a publication [35], I examine the resolution limits of the magnetic tweezer set by thermal noise. To accurately characterize the noise, I use the Power Spectral Density (PSD) and Allan variance (AV). I present analytical solutions for the PSD and AV of bead motion in a quadratic potential well, with particular analytical solutions found for video-tracking instruments with long shutter times.

3.1 A Hookean model for tether elasticity

A simple conceptual model for the bead and tether system in a magnetic tweezer is shown in Figure 3.1. Here, the system is modeled as ball on a spring

in a viscous medium. In this model, the drag due to the tether is neglected since it is relatively small.

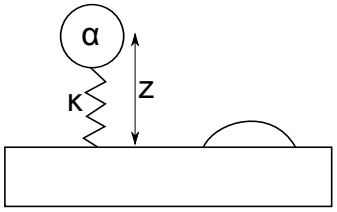

Figure 3.1: A conceptual model for the bead in a magnetic tweezer with surface-bead center distance z, bead drag coefficient α, and tether stiffness κ

3.2 Bead rotation

A purely paramagnetic bead will have a magnetic moment that increases with applied external field. By rotational symmetry, there is no preferred direction for a spherical paramagnet, and thus a superparamagnetic bead should not have any rotational preference in a magnetic tweezer. However, experimentally it is well established that superparamagnetic beads align in external fields in magnetic tweezers [36]. It was recently revealed that the origin of the preferred orientation of the magnetic beads used in magnetic tweezers is due to the non-uniform distribution of nanoparticles in the beads rather than the alignment axis of individual particles. [37]

The rotation of beads with rotation axis perpendicular to the magnetic field and perpendicular to the surface normal (see Figure 3.2a) has been shown to

change the apparent height of the bead [36]. The fluctuation magnitude is bead-dependent due to a varying uniformity of magnetic nanoparticle distributions within each bead, and due to variation in the angle of tether attachment with respect to the preferred bead magnetization moment.

Bead rotation parallel to the magnetic field (see Figure 3.2b) has been shown to influence force calibration [38]. In this axis of rotation, the preferred magnetic moment of the bead remains aligned with the field, but the bead performs work against the magnetic field gradient, and thus there is a restoring torque.

Bead rotation parallel to the surface normal (see Figure 3.2c) is energetically unfavorable and has no influence on apparent bead height. However, it is the only rotational angle of the bead that has been experimentally measured [39].

The rotational fluctuations that influence tether height are ignored in this thesis since they cannot be experimentally measured.

3.3 Langevin dynamics and the PSD of bead motion

Micron-sized probe beads trapped by optical or magnetic forces in water obey the Langevin equation [40], which relates the total force F to the mass m, the position coordinate x (can also be y or z), the velocity $\dot{x}$, the acceleration $\ddot{x}$,

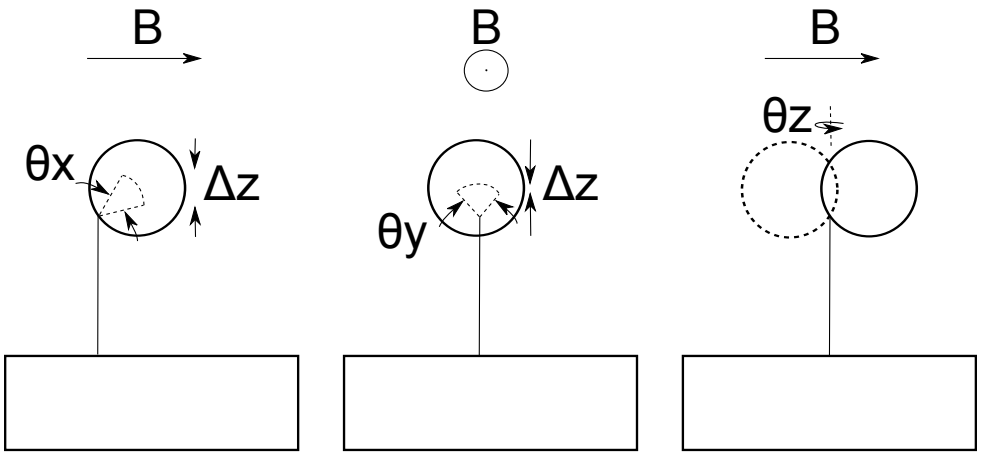

Figure 3.2: Rotational fluctuations of a magnetic bead in the three rotational degrees of freedom, and their influence the apparent height of the bead.

the spring constant of the trap κ, the drag coefficient α, and the the stochastic Langevin force F_L:

$$\sum F = m\ddot{x} = -\kappa x - \alpha\dot{x} + F_L \tag{3.1}$$

3.4 The Fourier Transform

A Fourier transform decomposes a time-domain signal consisting of N points into a sum of sin and cosine waves.

$$x(t) = \sum_{j=0}^{N-1} \left(a_j \cos(2\pi j/N) + b_j \sin(2\pi j/N)\right) \tag{3.2}$$

where a_j are the coefficients for cosine waves and b_j are the coefficients for sin waves.

The PSD at each frequency represents the amplitude of the wave, $\tilde{P} = a_j^2 + b_j^2$. In theory, a sine wave plus a cosine wave of equal frequencies can be represented as a single sine wave with a phase $\phi = \tan^{-1}(a_j/b_j)$. In magnetic tweezer experiments, the phase of particle position frequencies has no physical meaning since the oscillatory driving force of the bead-tether systems is caused by stochastic collisions with water molecules, which is why the PSD contains all the relevant information of the Fourier Transform despite the fact that the PSD discards phase information.

For a finite data set with N points collected at a sampling frequency of f_S, we can use the discrete Fourier transform (DFT) to calculate the PSD:

$$\tilde{P}_{w,N} = \frac{1}{f_s N} \left| \sum_{j=0}^{N-1} w_j x_j e^{-2\pi i j k/N} \right|^2 \tag{3.3}$$

The PSD allows us to compare the noise of particle tracking between instruments, different beads, and even different tether molecules. One disadvantage to using the PSD is that the units of $\mathrm{nm}^2/\mathrm{Hz}$ are somewhat unintuitive as compared to a metric such as the standard deviation, which has intuitive units of nm.

By taking the Fourier transform of Equation 3.1, and using the property that $\mathcal{F}(\dot{x}) = 2\pi i \hat{x}(f)$, we can arrive at:

$$\hat{x}(f) = \frac{\hat{F}_L}{\kappa + 2\pi i \alpha f - 4\pi^2 m f^2} \tag{3.4}$$

where $\hat{x}(f)$ is the Fourier transform of $x(t)$. Taking the absolute value squared of both sides gives:

$$P(f) = |\hat{x}(f)|^2 = \frac{\left|\hat{F_L}\right|^2}{|\kappa + 2\pi i\alpha f - 4\pi^2 m f^2|^2} \tag{3.5}$$

At high frequencies, $f \gg \frac{\kappa}{2\pi\alpha}$, the lowest order term in the denominator disappears and the motion reduces to diffusive motion with inertial effects:

$$P(f) = |\hat{x}(f)|^2 = \frac{\left|\hat{F_L}\right|^2}{|2\pi\alpha f(i - 2\pi^2 m f/\alpha)|^2} = \frac{\left|\hat{F_L}\right|^2}{4\pi^2\alpha^2 f^2(1 + (2\pi m f/\alpha)^2)} \tag{3.6}$$

At even higher frequencies, $f >> \alpha/(2\pi m)$, the highest order term in the denominator becomes significant. Physically, this can be intuited as the motion of the particle transitioning from diffusive motion to ballistic motion [41]. For 1 μm polystyrene particles in water, this corresponds to: $f_{ballistic} = 113$ MHz. At the maximum video tracking rates of a few hundred kHz used in this thesis, inertia can be ignored [42]. The relevant bead position $x(t)$ vs. time t can then be well-approximated by the overdamped Langevin equation of motion:

$$\kappa x + \alpha\dot{x} = F_L \tag{3.7}$$

where κ is the spring constant of the system, and $\alpha = 6\pi\eta r$ is the dissipation of the spherical bead of radius r in a solution of viscosity η. F_L is the Langevin force, a time-varying stochastic force that, in thermal equilibrium, obeys the fluctuation-dissipation relation $\langle F_L(t + t_0)F_L(t)\rangle = 2\alpha k_B T\delta(t_0)$ given thermal energy $k_B T$. The power spectral density of bead motion, $P(f)$, where f is the frequency in

hertz, can be calculated by taking the magnitude of the Fourier transform of Eq. 3.7 to obtain:

$$P(f) = \frac{k_B T}{2\pi^2 \alpha (f_c^2 + f^2)}, \tag{3.8}$$

where $f_c = \frac{\kappa}{2\pi\alpha}$. I use two-sided power spectra throughout, so that integrating $P(f)$ on the range $(-\infty, \infty)$ results in the equipartition result $\langle x^2 \rangle = k_B T/\kappa$.

In the frequency domain, I derive an expression for the measured probe PSD, $P_{A,B}(f)$, that accounts for both aliasing and the video-tracking instrument response. While approximations to this expression have been made before [43], this expression is exact. Finite-duration (spectral leakage) effects can be removed by calculating the windowed, blocked PSD, $\tilde{P}_{b,w}(f)$, using established DFT algorithms [44, 45]. Finally, following Nørrelykke and Flyvbjerg [46], I show that bias-free fitting of $P_{A,B}$ to $\tilde{P}_{b,w}(f)$ can be achieved using a maximum-likelihood estimate (MLE) algorithm.

3.4.1 An analytical expression for the PSD function, accounting for aliasing and the instrument function

The PSD of Eq. 3.8 corresponds to the true physical motion of the bead; any actual measurement $\tilde{P}(f)$ will deviate from $P(f)$ due to the distorting effects of aliasing and the instrumentation. In video-tracking experiments in which the bead position is measured by a camera with a shutter time τ_s, any motion of the bead that occurs on timescales faster than τ_s is diminished by the measure-

ment [47]; i.e. video-tracking introduces a low-pass filter. The low-pass filtering effect of the camera can be quantitatively accounted for: when the illumination is constant over τ_s, the measured position x_i from frame i at time t_i corresponds to the average over the interval $(t_i - \tau_s/2, t_i + \tau_s/2)$:

$$\begin{aligned} x_i &= \frac{1}{\tau_s} \int_{t_i - \tau_s/2}^{t_i + \tau_s/2} x(t) dt \\ &= [x * \Pi_{\tau_s}](t_i) \end{aligned} \tag{3.9}$$

which I have written in the second line as the convolution of $x(t)$ with the boxcar function $\Pi_{\tau_s}(t)$. I define $\Pi_{\tau_s}(t')$ to have value $1/\tau_s$ for$|t'| < \tau_s/2$, and to be zero otherwise. The frequency-space equivalent of convolution is simply multiplication of the Fourier transforms of the two convolved functions. Thus, since the Fourier transform of $\Pi_{\tau_s}(t)$ is $\sin(\pi f \tau_s)/(\pi f \tau_s)$, the PSD of bead motion including the boxcar response, $P_B(f)$, is

$$P_B(f) = P(f)H(f) \tag{3.10}$$

where the instrument response $H(f)$ is

$$H(f) = \frac{\sin^2(\pi f \tau_s)}{(\pi f \tau_s)^2} \tag{3.11}$$

In practice, accurately and precisely comparing $P(f)$ and $\tilde{P}(f)$ is difficult for three reasons:

1. *Instrument response* The instrument used to measure probe position invariably has a non-uniform frequency response, distorting $\tilde{P}(f)$ away from $P(f)$.

2. *Finite sampling distortions* $\tilde{P}(f)$ is distorted by the effect of aliasing, in which the estimated power at a given frequency f_k contains contributions from all frequencies $f_k + nf_s$, where $n = \ldots, -1, 0, 1, \ldots$, and f_s is the sampling frequency. Further, $\tilde{P}(f)$ is also distorted by the effects of the finite duration of the measured probe trajectory, which result in spectral leakage in the resulting estimate of the PSD.

3. *Biased fitting* The model/data comparison method itself can bias the estimated parameters, as the typical strategy of least-squares fitting is correct only when the error in the data is normally distributed, which is not the case for the estimated PSD [46].

$P_B(f)$ only accounts for the effect of instrumental low-pass filtering in distorting the measured PSD; it does not account for the further distortions created by aliasing. The aliasing effect causes the PSD at a particular positive frequency f', with $0 < f' < f_s/2$, to contain the summed power at all frequencies in the series $|f' + nf_s|$, where $n \in \{\ldots, -1, 0, 1, \ldots\}$ [43]. Thus, the measured PSD accounting for both aliasing and boxcar filtering is given by:

$$P_{A,B}(f) = \sum_{n=-\infty}^{\infty} P_B(|f + nf_s|) \tag{3.12}$$

with P_B given by Eqs. 3.10 and 3.11.

In the special case that the sampling frequency is the inverse of the shutter time, $f_s = 1/\tau_s$, the sum in Eq. 3.12 can be performed analytically:

$$P_{A,B}(f) = \frac{2k_BT\alpha}{\kappa^3}\left(\kappa + \frac{2\alpha f_s \sin^2\left(\frac{\pi f}{f_s}\right)\sinh\left(\frac{\kappa}{\alpha f_s}\right)}{\cos\left(\frac{2\pi f}{f_s}\right) - \cosh\left(\frac{\kappa}{\alpha f_s}\right)}\right) \tag{3.13}$$

Eq. 3.13 can be verified in multiple ways. First, I use $P_{A,B}$ and the Wiener-Khinchin relation are used to find the variance of the measured signal in the time domain; the result matches previously predicted results for boxcar-averaged probe positions [43]. Second, I compare $P_{A,B}$ with $P_A(f)$, the PSD expression that accounts only for aliasing (and not instrumental low-pass filtering) [48]:

$$P_A(f) = \frac{k_BT}{\kappa f_s}\left(\frac{\sinh\left(\frac{\kappa}{\alpha f_s}\right)}{\cosh\left(\frac{\kappa}{\alpha f_s}\right) - \cos\left(\frac{2\pi f}{f_s}\right)}\right) \tag{3.14}$$

P_A corresponds to the PSD measured by an instrument with sampling frequency f_s, but with an infinitely fast measurement interval (i.e. the boxcar measurement function, Π_τ, is replaced by a delta function). I compare $P_A(f)$ and $P_{A,B}(f)$ to experimental data in Fig. 3.3. The data are clearly best-described by $P_{A,B}$, lending confidence to the expression in Eq. 3.13.

I further verify the prediction of Eq. 3.13 through simulation of probe trajectories in the time domain, computation of the PSDs of the simulated trajectories, and comparison to $P_{A,B}$. I simulated discrete particle trajectories using an algorithm based on the solution to the Smoluchowski equation for a Brownian particle in a harmonic well [49]. To account for the averaging effect of the boxcar filter, we simulated discrete points with a short time step of $\delta < \tau$, then averaged to-

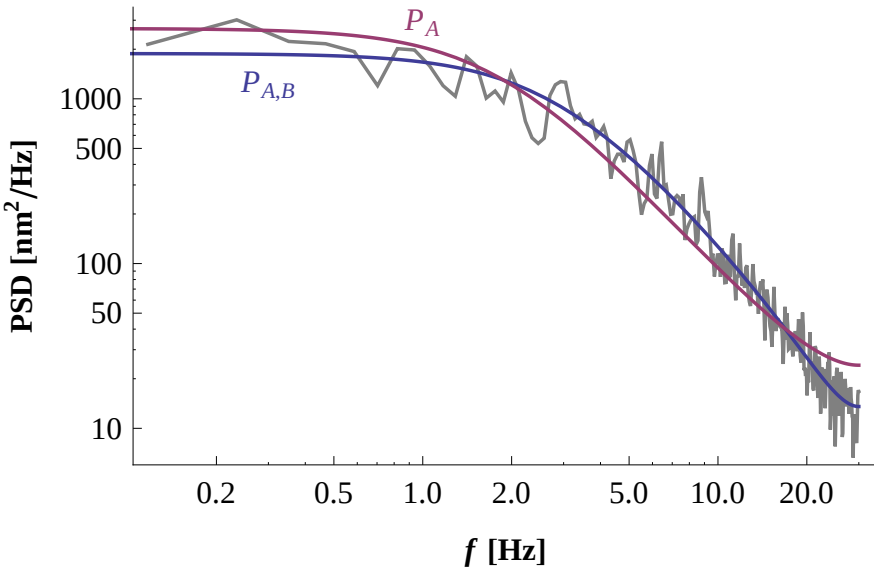

Figure 3.3: Experimental PSD (gray) compared to MLE fits to $P_{A,B}$ (Eq. 3.13, blue) and P_A (Eq. 3.14, purple). The data trajectory contained 4096 points, and was acquired by 60 Hz video-tracking of a 1 μm diameter bead tethered to a DNA molecule in a magnetic tweezer (see Ribeck [10] for experimental procedure). The trace was split into half-overlapping blocks of 512 points and Hann-windowed before PSD calculation. The best-fit parameters from the $P_{A,B}$ fit are $\kappa = 2.46 \times 10^{-4}$ pN/nm and $\alpha = 1.39 \times 10^{-5}$ pN s/nm.

gether consecutive clusters of τ/δ points, thus arriving arrive at a set of discrete positions x_i spaced by time τ. We did this for multiple time steps $\delta = \tau/m$, with $m = 1, 2, 4, 8, 16$. Fig. 3.4 shows comparisons of the simulation with both $P_{A,B}$ and P_A for both $f_c \ll f_s$ and $f_c \approx f_s$. For $m = 1$, there is no averaging of the time-domain signal, so the simulated PSDs match P_A, as expected. As m increases, the simulated PSDs converge on $P_{A,B}$. This directly indicates that Eq. 3.13 correctly accounts for the camera's averaging effect on the measured probe position.

3.4.2 Estimating the PSD from a time-series of data

Spectral leakage and windowing Given a set of N discrete measurements of probe position vs. time, an estimate, $\tilde{P}(f)$, of the PSD can be made from the discrete Fourier transform (DFT). Directly comparing $\tilde{P}(f)$ to $P_{A,B}(f)$ (Eq. 3.13) leads to difficulties due to the finite duration of the measurement: the frequency-domain analysis of the Langevin equation implicitly assumes that the trajectory is infinitely long, while any measurement will naturally be of finite duration. This truncation leads to the phenomenon of spectral leakage, in which some power present in the signal at one frequency shows up at other frequencies. For white noise, spectral leakage has no effect, as neighboring frequencies leak equal and opposite power to each other, resulting in zero net change. However, for limited

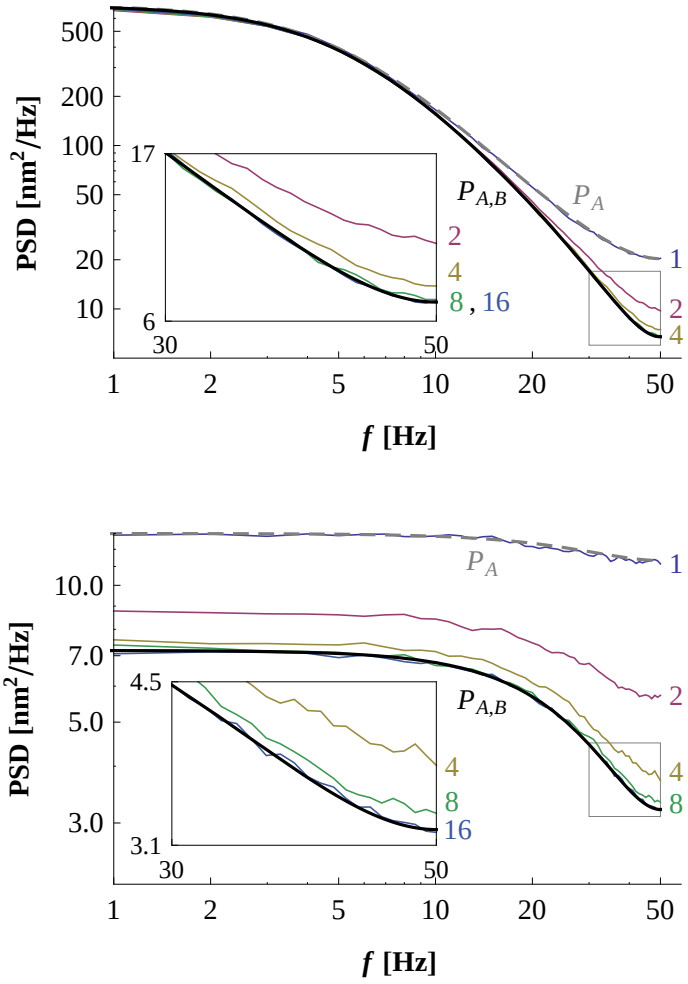

Figure 3.4: Plots of PSDs measured from time-domain simulations compared to the analytical PSDs, P_A (gray dashed line; Eq. 3.14) and $P_{A,B}$ (solid black line; Eq. 3.13). The measured PSDs (colored lines) correspond to averages of 10^4 simulations. Each simulation contained 1024 points with $\alpha = 10^{-5}$ pN s/nm and $f_s = 100$ Hz, with each point representing the average of $m = 1, 2, 4, 8, 16$ simulation time steps, as labeled. The spring constant was set to give (top) $f_c = 5$ Hz, or (bottom) $f_c = 50$ Hz. The insets highlight the convergence of the measured PSD to $P_{A,B}$ with increasing m. We note that the bottom figure has an apparent corner frequency which is due to the low-pass filtering effect of the camera (see Equation 3.11).

bandwidth signals (such as the Lorentzian, where the power is focused in the range $f < f_c$), spectral leakage leads to PSD distortions.

Spectral leakage can be minimized by 'windowing' the input data [44]. In particular, given N measurements of probe position, x_j, $j\epsilon\{0, 1, 2, \ldots, N-1\}$, at sampling rate f_s, the PSD can be estimated from:

$$\tilde{P}_{w,N} = \frac{1}{f_s N} \left| \sum_{j=0}^{N-1} w_j x_j e^{-2\pi i j k/N} \right|^2 \tag{3.15}$$

where w_j is the windowing function, which can be chosen from a range of standard functions, all of which taper to zero at the edges of the data trace [50]. Here, we use a Hann window, defined by

$$w_j = \sqrt{\frac{8}{3}} \sin^2\left(\frac{\pi j}{N}\right) \tag{3.16}$$

Application of the window reduces the total power in the PSD in a frequency-independent manner; this is corrected by the leading factor of $\sqrt{8/3}$.

Blocking In the absence of stochastic noise, the windowed PSD $\tilde{P}_{w,N}$ would converge on the analytical aliased filtered Lorentzian $P_{A,B}$. However, a feature of the discrete Fourier transform is that increasing N does not decrease the stochastic noise; instead it increases the number and density of estimates in frequency space. Moreover, while the noise in x_j is normally distributed, the stochastic noise in a single power spectrum is distributed exponentially, complicating least-squares fitting routines that assume normally-distributed noise.

The stochastic noise can be decreased, and the noise distribution made more normal, by compressing the data. Typically, this is done by blocking [46]: the data trace is separated into b blocks of length m, the PSD of each block, $\tilde{P}_m$, is calculated, and averaged with all others to give the blocked PSD $\tilde{P}_b = \sum \tilde{P}_m/b$. Blocking should be adjusted when also windowing, as application of the window minimizes the contribution of data near the termini of each block. All of the data can be efficiently utilized by following Welch's method [45]: instead of blocking into non-overlapping bins, $b = N/m$, the data trace is blocked into half-overlapping bins (Fig. 3.5), giving $b = 2N/m - 1$. The windowed PSD of each block, $\tilde{P}_{w,m}$, is calculated, and averaged with all others to give the final blocked, windowed PSD estimate $\tilde{P}_{w,b} = \sum \tilde{P}_{w,m}/b$. This insures efficient exploitation of all of the available data while keeping each bin statistically independent of its neighbors.

The noise distribution in a PSD Recently, Nørrelykke and Flyvbjerg [46] have pointed out that, even after blocking, the distribution of noise in the estimated PSD is typically still far from normally distributed, but that fitting can proceed in a precise manner by accounting for the actual distribution: averaging b spectra together causes the noise distribution to be the convolution of b exponential distributions, which is a Gamma distribution. In a Gamma distribution,

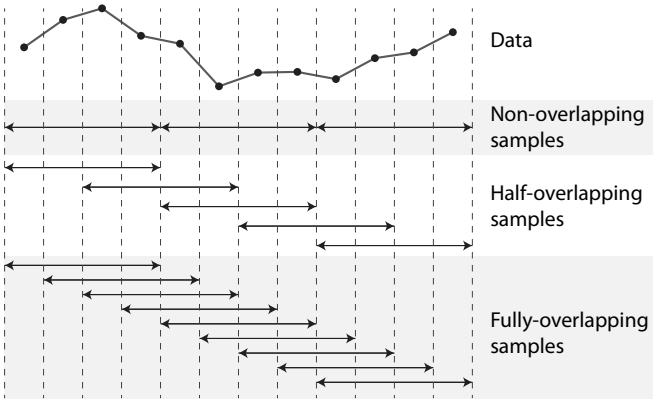

Figure 3.5: Illustration of different manners of binning ('blocking') data, shown here for an example trace containing $N = 12$ points split into bins of length $m = 4$. Non-overlapping sampling corresponds to no sharing of points between bins, and gives 3 bins in this example. This is used in calculation of the 'standard' AV, or in non-windowed estimates of the PSD; neither method is optimal, as described in the main text. Half-overlapping sampling use bins that are offset by half the binning interval from each neighbor, giving 5 bins offset by 2 points in this example. This insures maximal data usage when calculating windowed PSDs, and is known as Welch's method [45]. Fully-overlapping sampling uses bins offset by a single point from each neighbor, giving 9 bins here. This method is used to calculate the overlapping Allan variance (OAV).

the probability f of observing a certain value x depends on parameters η, θ as:

$$f(x;\eta,\theta) = x^{\eta-1}\frac{e^{-x/\theta}}{\theta^{\eta}\Gamma(\eta)} \tag{3.17}$$

where $\Gamma(\eta)$ is the gamma function. The two free parameters are the shape parameter η and the scale parameter θ. For a PSD calculated from b blocks, and whose true value is given by $P_{A,B}(f_k)$, the probability of observing $\tilde{P}_{b,w}$ is proportional to $f(\tilde{P}_{b,w}; b, P_{A,B}(f_k)/b)$; that is, the shape is $\eta = b$ and the scale is $\theta = P_{A,B}(f_k)/b$. Explicitly using the Gamma distribution allows for the application of bias-free maximum-likelihood estimation [46]. We discuss this below (Sec. 3.6), in conjunction with a similar discussion of fitting to the Allan Variance.

3.5 Allan Variance

The AV is a two-sample difference measurement [51] that is well-known in the frequency-stability literature [52, 53] and has recently been introduced to the SMM community [19, 21, 54, 55]. The low-error, bias-free α and κ estimation contrasts favorably with prior work that focused on only some of the sources of bias, and used only frequency domain methods [18, 44, 46, 56].

3.5.1 Definition of the Allan Variance

The Allan variance (AV), denoted by $\sigma^2(\tau)$, is a time-domain measure: it is half of the ensemble-averaged variance of the difference between two consecutive

samples of position [57, 58], where each sample is itself a local average of probe position (Eq. 3.18). The timescale τ denotes both the time between consecutive samples, and the time over which each sample is averaged. Thus, for a probe position $x(t)$, and integer j, the AV is defined by

$$\sigma^2(\tau) = \frac{1}{2}\left\langle (\bar{x}_{\tau,j+1} - \bar{x}_{\tau,j})^2 \right\rangle \tag{3.18}$$

where $\bar{x}_{\tau,j}$ is given by

$$\bar{x}_{\tau,j} = \frac{1}{\tau}\int_{\tau\left(j-\frac{1}{2}\right)}^{\tau\left(j+\frac{1}{2}\right)} x(t)dt \tag{3.19}$$

$$= [x * \Pi_\tau](j\tau). \tag{3.20}$$

The identical forms of Eqns. 3.9 and 3.20 emphasize that the camera measures an average probe position, exactly as called for by the AV. Thus, while the PSD requires special corrections for a box-car filtering instrument function, the AV does not, simplifying its use in this situation. In situations where data contains dead-time, for example when the frame-read time of a CCD approaches the frame acquisition time, the AV can compensated by bias correction when the noise sources have known power-laws [59, 60]. In our experiments using a JAI CV-A10CL camera, the ratio of frame-read time to frame-acquisition time is very small, 3.5 μs $\times$ 60 Hz $\ll 1$, so the instrument function is well-approximated by the boxcar function introduced in Eq. 3.9.

3.5.2 An analytical expression for the AV of a damped harmonic oscillator

In analogy to Section 3.4.1, we derive an analytical expression for the AV for a Brownian probe in a harmonic well. By expanding the product in Eq. 3.18, we find that the AV is related to the variance and autocorrelation of $\bar{x}_\tau$:

$$\sigma^2(\tau) = \left\langle \bar{x}_\tau^2 \right\rangle - \left\langle \bar{x}_{\tau,j+1} \bar{x}_{\tau,j} \right\rangle \tag{3.21}$$

where we have made use of the stationary nature of the process, so $\left\langle \bar{x}_{\tau,j+1}^2 \right\rangle = \left\langle \bar{x}_{\tau,j}^2 \right\rangle \equiv \langle \bar{x}_\tau^2 \rangle$. The Wiener-Khinchin theorem can be used to relate the variance and autocorrelation of $\bar{x}_\tau$ to its PSD; in turn, given the properties of convolution, the PSD of $\bar{x}_\tau$ depends on the PSD of $x(t)$ and of Π_τ. This allows the AV to be related to $P(f)$, giving [52]:

$$\sigma^2(\tau) = \int_{-\infty}^{\infty} \frac{4\sin^4(\pi f \tau) P(f)}{(\pi f \tau)^2} df \tag{3.22}$$

Using Eq. 3.8, this integral can be performed to obtain an analytical expression for the AV of an overdamped bead in a harmonic well:

$$\sigma^2_{SMM}(\tau) = \frac{2k_B T \alpha}{\kappa^2 \tau} \left(1 + \frac{2\alpha}{\kappa\tau} e^{\frac{-\kappa\tau}{\alpha}} - \frac{\alpha}{2\kappa\tau} e^{\frac{-2\kappa\tau}{\alpha}} - \frac{3\alpha}{2\kappa\tau} \right) \tag{3.23}$$

This expression has long been known in the frequency-stability literature [61] but we have rewritten it here in terms of α and κ with special application to SMM experiments. For long times, $\tau \gg \alpha/\kappa$, the AV reduces to $\sigma^2_{SMM}(\tau) \approx \frac{2k_B T \alpha}{\kappa^2 \tau}$, consistent with previously published approximations [19, 21, 54]. The large time

limit can be understood by noting that neighboring $\bar{x}_\tau$ values become uncorrelated for large τ, so the variance arises from the standard error in determining the mean of a normally distributed value, i.e. variance $\sim 1/(\#\text{ of points}) \sim 1/\tau$. In the opposite limit, $\tau \ll \alpha/\kappa$, we find $\sigma^2(\tau) \approx \frac{2k_BT\tau}{3\alpha}$; that the variance increases linearly with τ arises from the purely diffusive nature of the probe motion at short times. Thus, a feature of the AV of a damped, Brownian harmonic oscillator is that it increases at short times and decreases at long times (Fig. 3.6); the location of the intervening peak can be found numerically to be $\tau_{max} \approx 1.89\alpha/\kappa$, i.e. the peak scales with the system's correlation time, α/κ.

Since the AV is a time-domain analysis, neither aliasing nor spectral leakage occur. Further, the calculation of Allan variance intrinsically assumes a finite averaging time that exactly matches the video-tracking instrument function, so no additional correction for the instrument needs to be applied. Thus, AV is well-suited to the problem of determining α and κ, since no corrections must be made for the instrument response, aliasing or spectral leakage. However, using the AV is not completely free of subtleties: we show that obtaining low-error, bias-free parameter estimates requires that the AV is estimated from data using bins that fully-overlap, and that range in length by factors of two. Finally, we point out that biased fitting is also an issue with the AV due to the non-normally distributed noise in AV estimates, and that estimating the noise distribution is more involved for the AV than the PSD. To overcome this, we extend the Nørrelykke-Flybjerg

strategies [46] to the Allan variance, and show that unbiased parameter estimates can be found from an MLE approach that accounts for the actual distribution of Allan variance estimates.

Upon comparing the two strategies, we find that the AV and the PSD, when applied in an optimal manner, can both estimate α and κ with zero-bias and with nearly-identical error. However, use of the AV is conceptually simpler, since fewer corrections need to be applied, and more practical, since the AV compresses the data more efficiently than the PSD. Furthermore, AV does not require the choice of a data compression (blocking) parameter, thus the AV calculation has less indeterminacy.

3.5.3 Estimating the AV from a time series of data

Overlapping AV.

For a discrete set of measurements of probe positions x_j at times $t_j = j\tau_s$ for $j = 1, \ldots, N$, the 'standard' AV can be calculated for timescale $\tau = m\tau_s$ by computing the mean of successive bins of m points, then taking the mean-squared difference of the resulting $N/m - 1$ neighboring pairs of bins. So, in particular, the first pair of bins corresponds to the sets of points $(1, \ldots, m)$ and $(m+1, \ldots, 2m)$, the second pair are points $(m+1, \ldots, 2m)$ and $(2m+1, \ldots, 3m)$, and so on through the Nth point. However, the standard AV is known to not fully utilize the data [62]. A superior option is the 'overlapping' AV ('OAV'),

which uses every possible m-bin (Fig. 3.5). In particular, the first OAV pair of bins is $(1, \ldots, m)$ and $(m+1, \ldots, 2m)$, the second pair is $(2, \ldots, m+1)$ and $(m+2, \ldots, 2m+1)$, and so on through the Nth point. The standard and overlapping AVs are identical for $m = 1$ and $m = N/2$, but elsewhere the OAV more efficiently exploits the available data, and so provides a better estimate of the true AV. The experimentally derived OAV can be computed from [63]:

$$\tilde{\sigma}_m^2 = \frac{1}{2(N-2m)(m\tau_c)^2} \sum_{k=1}^{N-2m} (z_{k+2m} - 2z_{k+m} + z_k)^2 \tag{3.24}$$

with $z_1 = 0$ and for $j = 2, ..., (N+1)$:

$$z_j = \sum_{i=1}^{j-1} x_i \tag{3.25}$$

In our initial publication [35], I made a typo in this equation [64]. However, I use only the correct OAV in all calculations throughout this article.

Octave sampling.

The OAV can be determined for any integer value of the bin size, $m = 1, 2, \ldots, N/2$ (see Fig. 3.6). However, upon estimating and plotting the OAV, it is clear that neighboring values of m have a correlated noise, which stems from the nearly-identical sets of points used to calculate the OAV for similar values of m. While calculating all possible m values might be useful for visualizing the data, the noise correlations preclude most fitting algorithms, which assume independent error in the fitted points. Allan pointed out that this issue can be solved

by octave sampling [65], i.e. only using bin sizes in powers of 2: $m = 1, 2, 4, 8, \ldots$ up to $m \leq N/2$. Using bins of 2^n ensures a minimal correlation between successive estimates, and improves the results of fitting, as shown in Fig. 3.8.

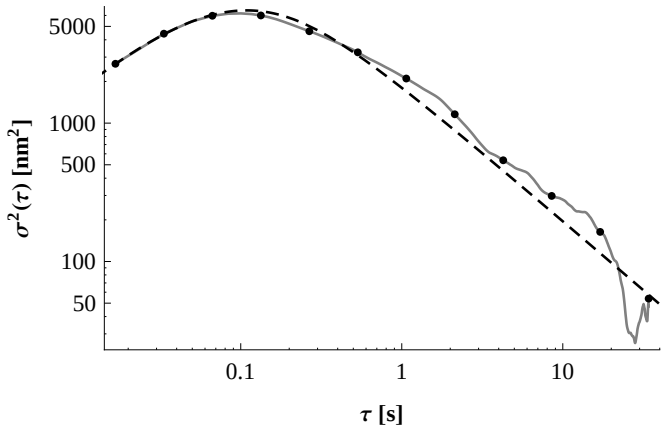

Figure 3.6: Experimentally-derived OAV calculating using bins of octaved lengths (points), or all possible lengths (gray line), compared to the best-MLE-fit to the theoretical prediction (Eq. 3.23, dashed line). The data were acquired as described in Fig. 3.3. The best-fit parameters are $\kappa = 2.40 \times 10^{-4}$ pN/nm and $\alpha = 1.38 \times 10^{-5}$ pN s/nm.

Error in the AV estimate. At the root of the AV is the difference $\bar{x}_{j+1} - \bar{x}_j$, which is normally distributed with mean zero. Thus, an estimate for the AV (which is a sum of squares of such differences) is Gamma distributed. The estimated blocked and windowed PSD, $\tilde{P}_{b,w}$ (Section 3.4.2), is also Gamma distributed, and $\tilde{P}_{b,w}$ has the same shape factor, $\eta = b$, for all frequencies f_k. However, the estimated AV does *not* have a constant shape factor because the number of available differences depends on the bin length m; this is the major complicating factor in working with the AV relative to the PSD.

Generally, the shape factor is given by the number of exponential distributions that are convolved to form the metric (this is why $\eta = b$ for the PSD). The standard AV for a given m is calculated from $N/m - 1$ differences; since each difference has a Chi-Square distribution, two of which must be convolved to get an exponential distribution, the shape factor is

$$\eta_{AV}(m) = \frac{1}{2}\left(\frac{N}{m} - 1\right) \tag{3.26}$$

As discussed, the OAV more efficiently exploits the available data, meaning that there are more available degrees of freedom per m. Thus, for the OAV, the shape factor of Eq. 3.26, while nearly correct, is an underestimate. The exact calculation of the available degrees of freedom for the OAV is quite involved, and beyond the scope of this paper; it has been the subject of much discussion in the literature [58, 66]. However, we have found that using η from the relatively simple Eq. 3.26 gives near-identical results to more exact, involved estimates, so we use Eq. 3.26 in all computations discussed below.

3.6 Maximum likelihood estimation

As discussed by Nørrelykke and Flyvbjerg [46], least-squares fitting to the PSD always leads to bias in the best-fit parameters. The bias occurs because of the least-squares assumption that the noise is normally-distributed, whereas the noise in the PSD is Gamma distributed (Sec. 3.4.2). Similarly, the noise in the

AV is Gamma distributed (Sec. 3.5.3), so least-squares fitting of AVs will also lead to biases. Although these biases can be analytically corrected [46], an unbiased and more accurate alternate to least-squares fitting is to perform a maximum likelihood estimate (MLE) that accounts for the correct noise distribution in the data [46]. The MLE approach stems from the assumption that the optimal parameters will maximize the joint probability $p_J = \prod_k p_k(\tilde{y}_k; y_k(\alpha, \kappa))$, where $p_k(\tilde{y}_k; y_k(\alpha, \kappa))$ is the probability of measuring a value $\tilde{y}_k$ given a true value y_k that depends on parameters (α, κ). By substituting the Gamma distribution, Eq. 3.17, for p_k, it can be shown that maximizing p_J is equivalent to minimizing the cost function [46]:

$$F' = \sum_k \eta_k \left(\frac{\tilde{y}_k}{y_k(\alpha, \kappa)} + \ln y_k(\alpha, \kappa) \right) \tag{3.27}$$

where η_k is the shape parameter for point k. Eq. 3.27 applies to both the PSD and AV. For the PSD, the shape factor is constant for all points, and equal to the number of blocks, $\eta_k = b$, while the true value is found from Eq. 3.13 as $P_{A,B}(f_k, \alpha, \kappa)$. For the AV, the shape factor is point-dependent, $\eta_k = \eta_{AV}$,where η_{AV} is defined in Eq. 3.26. The true value is found from Eq. 3.23 as $\sigma^2_{SMM}(\tau = k\tau_c, \alpha, \kappa)$. In either case, minimization of Eq. 3.27 with respect to (α, κ) can be carried out relatively efficiently using most numerical analysis software; we use the MLE approach to generate the results described below.

3.7 Experimental Results

To demonstrate the applicability of our AV fitting method to experimental data, a magnetic tweezer instrument is used to stretch double-stranded DNA molecules over a range of forces [10]. From each particle trajectory taken at a constant force, the octave-sampled, overlapping AV, with MLE fitting of Eq. 3.23 is used to estimate α_x, α_y, α_z, κ_x, κ_y, and κ_z. These results are compared to those independently estimated by theories of bead drag or polymer elasticity.

In Figure 3.9 is the drag coefficient$\alpha_x, \alpha_y, \alpha_z$ as a function of the average bead height. As the magnetic force is decreased, the bead height decreases and the drag coefficient of the bead increases due to surface effects, which can be theoretically predicted using the Faxén correction [67]. Both α_x and α_z closely match the theory (solid lines in Figure 3.9). Due to the rotational constraints imposed on the magnetic beads by the applied magnetic field, $\alpha_y > \alpha_x$. At the highest forces tested, the fitting routine was unable to accurately determine α_z, since the corner frequency of the system approached and exceeded the Nyquist frequency of our camera.

In Figure 3.9 is the experimentally derived κ_x, κ_y, κ_z values as a function of extension. At each measured tether extension L is a predictions for κ_x, κ_y, κ_z obtained by using the worm-like-chain model for double-stranded DNA [68] to convert L into an estimate of force, F and then use the inverted-pendulum model for magnetic tweezers [47] to convert F and L into expected stiffness through the

relations: $\kappa_z = \frac{\partial F}{\partial z}$, $\kappa_x = F/L$, and $\kappa_y = F/(L+R)$. For all predictions, we use a persistence length of 53 nm, consistent with previous measurements [68], and a contour length of 1720 nm. Although we do not correct for bead mistethering [36, 37], there is still good agreement between theory and experiment over a wide range of forces in all six measured parameters.

3.8 Recipe for obtaining α and κ

I have presented two strategies for calibrating the spring constant κ and measuring the drag α in a Single-molecule manipulation (SMM) instrument that uses full-frame video-tracking to measure probe position. These strategies are based on the Allan variance (AV) and Power spectral density (PSD). In particular, given N discrete measurements of position $x_j(t)$, with $j\epsilon\{0, 1, 2, ..., N-1\}$, we suggest the following fitting procedure for the PSD:

1. Divide the trace into half-overlapping bins of length $m \leq N/8$, resulting in $b = 2N/m - 1$ bins.

2. For each bin, multiply x_j by a Hann window and calculate a windowed PSD $\tilde{P}_{w,m}$ for each bin (Eq. 3.15)

3. Average the Power spectra over all bins to obtain a single blocked and windowed $\tilde{P}_{b,w}$

4. Minimize the cost function in Eq. 3.27 using $y_k = P_{A,B}(\alpha, \kappa, f_k)$, $\tilde{y_k} = \tilde{P}_{b,w}(f_k)$ to obtain α and κ

The corresponding recipe for calculating α and κ using an AV fit to the same data is:

1. Calculate the octave-sampled OAV $\tilde{\sigma}^2_m(\tau)$ using Eq. 3.24
2. Calculate the shape factor $\eta_{AV}(m)$ from Eq. 3.26
3. Minimize the cost function in Eq. 3.27 using $\eta_{AV}(m)$, $y_k = \sigma^2_{SMM}(\tau, \alpha, \kappa)$ and $\tilde{y}_k = \tilde{\sigma}^2_m(\tau)$ to obtain α and κ

PSD vs Allan Variance

Both the AV and PSD algorithms are capable of unbiased, low-error parameter estimates of equal quality (Figs.3.7 and 3.8). However, the AV algorithm is conceptually easier to understand and use. While both the AV and PSD require fitting with a Maximum Likelihood Estimation (MLE) algorithm rather than least-squares, the PSD approach requires applying multiple corrections, particularly for instrument response, discrete sampling (aliasing), and finite-duration of the data (spectral leakage). The AV is not subject to any of these three issues, as the instrument response intrinsic to video tracking exactly matches the assumptions made in calculating the AV, and the PSD finite-sampling effects that manifest in the DFT sum are simply not present in the time-domain AV calcu-

lation. Further algorithmic simplicity is achieved by the AV in that no choice of blocking number, b, needs to be made.

Numerical minimization of the cost function (Eq. 3.27) is also more straightforward with the AV because it achieves superior data compression without sacrificing accuracy or precision. The octave-sampled OAV for a data trace of N points contains $\log_2 N$ points, while the estimated PSD (using the maximum bin length that still reduces stochastic error) contains $N/8$ points. Therefore, the total number of points that must be fit grows linearly with N for the PSD, but only logarithmically with N for the AV. For example, for the $N = 4096$ traces simulated here, the AV contains 12 points, while the PSD contains 513 points. This means that the MLE cost function (Eq. 3.27) contains only 12 terms when working with the AV, but contains 513 terms for the PSD. Because of the advantages in simplicity, speed, and robustness of fitting with the AV as compared to the PSD, we suggest that the Allan variance is the ideal calibration method for many SMM instruments.

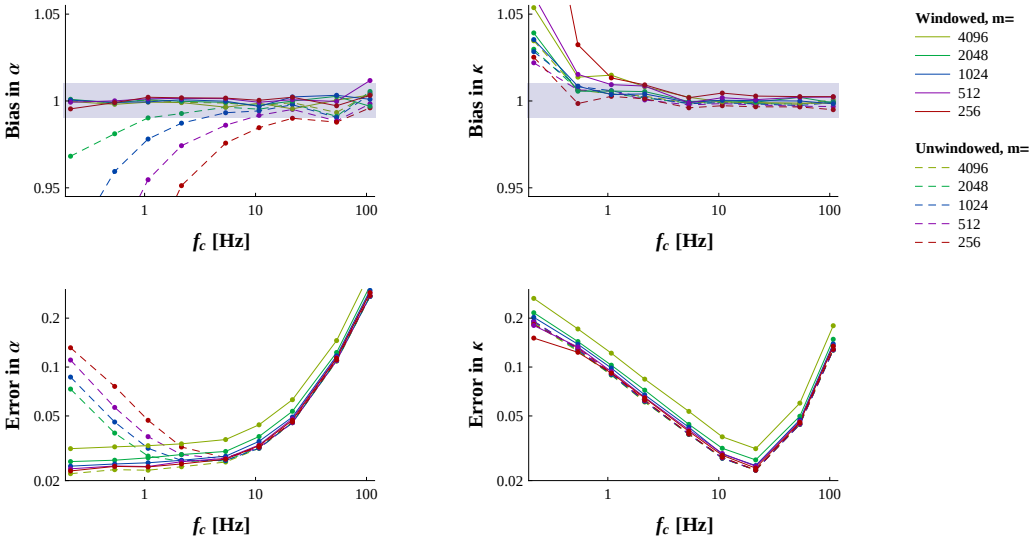

Figure 3.7: Bias and error in the best-fit parameters α and κ found from MLE fitting of Eq. 3.13 to simulated PSDs. 1000 simulations of a video-tracking experiment were performed; each simulation contained 4096 points and used $\alpha = 10^{-5}$ pN s/nm and $f_s = 100$ Hz. The spring constant κ was set to give a range of f_c between 0.2 and 100 Hz. Each trajectory was blocked into sub-sequences of length m, as indicated, and the PSD was calculated either using a Hann window (solid lines) or not (dashed lines). We used half-overlapping blocks (Fig. 3.5) for the windowed calculation, and non-overlapping blocks for the unwindowed calculation. The bias (top row) is reported as the median best-fit value across all simulations relative to the true value, while the error (bottom row) is reported as the standard deviation in best fit results relative to the median value. In the bias plots, the gray bar indicates values within $\pm 1\%$ of being unbiased.

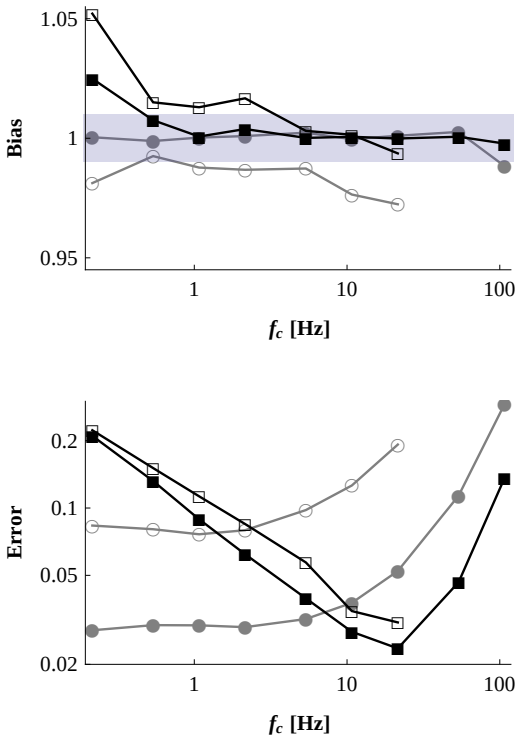

Figure 3.8: Bias and error in the best-fit parameters α and κ found from MLE fitting of Eq. 3.23 to simulated AVs. Trajectories were simulated with parameters as described in Fig. 3.7. From each trajectory, we calculated and fit to both the octave-sampled, overlapping AV ($\alpha : \bullet$ and $\kappa : \blacksquare$), and the all-τ, overlapping AV, ($\alpha : \circ$ and $\kappa : \square$). The bias (top) is reported as the median best-fit value across all simulations relative to the true value, while the error (bottom) is reported as the standard deviation in best fit results relative to the median value. In the bias plots, the gray bar indicates values within $\pm 1\%$ of being unbiased.

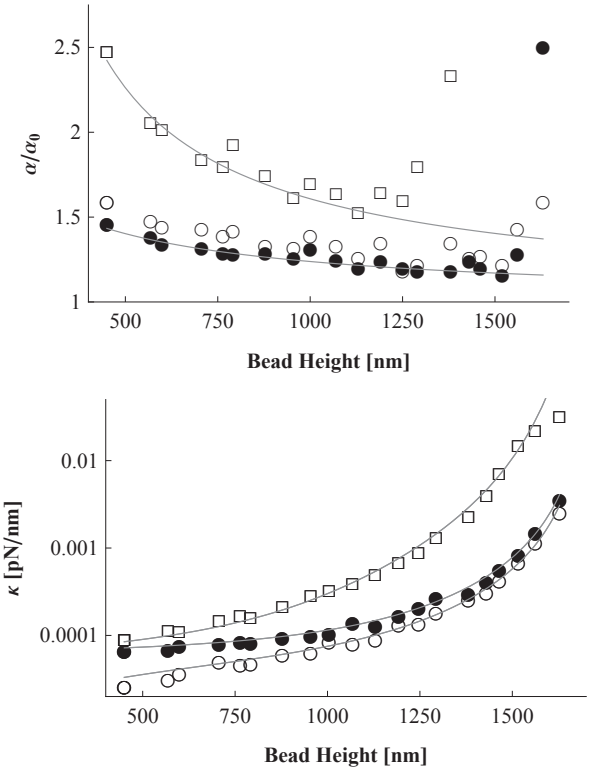

Figure 3.9: Experimental results showing the relationship between the measured drag coefficients $(\frac{\alpha_x}{\alpha_0} : \bullet)$,$(\frac{\alpha_y}{\alpha_0} : \circ)$,$(\frac{\alpha_z}{\alpha_0} : \square)$ and the bead height above the surface in comparison to the theoretical Faxén' correction [67]. For all theoretical curves, we use radius $R = 530$ nm, viscosity $\eta = 0.00115$ Ns/m^2, and $\alpha_0 = 6\pi\eta R$. The bottom panel demonstrates the relationship between the extension of dsDNA and the measured stiffness coefficients $(\kappa_x : \bullet)$, $(\kappa_y : \circ)$, $(\kappa_z : \square)$ in comparison to the predictions of a model that combines dsDNA's worm-like-chain elasticity [68] with the inverted-pendulum model of a magnetic tweezer [47]. For all analytical worm-like-chain curves, we use persistence length $l_p = 53$nm, contour length $L_0 = 1720$ nm, and $R = 530$ nm.

Chapter 4

A high speed magnetic tweezer beyond 10,000 fps

This chapter is largely drawn from a recent publication [69].

4.1 Introduction

The accurate measurement of tether extension in the presence of thermal noise requires a bandwidth above the corner frequency $f_c = \frac{\kappa}{2\pi\alpha}$ in order to avoid aliasing of high frequency diffusive motion into lower frequencies where they will interfere with extension measurements. The corner frequency for bead motion in the vertical direction in typical magnetic tweezer experiments can range from a few hertz to several kilohertz. Since the thermal noise for an instrument with a given bandwidth scales with α/κ^2, small beads and stiff tethers are desired in

high resolution experiments to minimize noise [14], which increases the corner frequency to the maximum possible values. For these reasons, a high bandwidth detector is desired that records bead positions at high frequencies. To maximize the bandwidth, I attach a high-speed CMOS camera to the magnetic tweezer with a frame rate of up to 100,000 frames per second (fps).

Tracking beads at high frame-rates with conventional LED illumination is unsatisfactory due to insufficient illumination intensity. To overcome this limitation, I introduce superluminescent diode illumination, which enables high-speed tracking. I further introduce GPU-accelerated particle tracking for high-speed analysis of video files. This high-speed magnetic tweezer is shown to resolve particle position to within 1 Å at 100 Hz, and to measure the extension of a 1566 bp DNA with 1 nm noise at 100 Hz in the presence of thermal noise.

4.1.1 Superluminescent Diode Illumination

The 2 mW Superluminscent Diode (SLD) (QPhotonics) has a spectral width of 7.9 nm at a central wavelength of 680 nm. To capture all the light of the superluminescent diode and obtain a relatively collimated beam (wavefronts parallel on sample plane), the light is fiber-coupled through a 0.12 Numerical Aperture (NA) single-mode fiber, and then projected onto the focal plane by a 7.5 mm focal length fiber collimator (Thorlabs). Light from the single-mode fiber exits through an angled physical contact (FC/APC) fiber to reduce back-reflections

from damaging the SLD and is focused by the 7.5 mm collimating lens at a distance of $z = 250$ mm. The minimum distance z is limited by the finite size of the magnets and the size of the slit between the pole pieces. From Gaussian beam optics [70], we can calculate the width of the waist w_0 given the width of the beam

$$w(z) = f\tan(\sin^{-1}(\mathrm{NA})) = 7.73\text{ mm}\tan(\sin^{-1}(0.12)) = 0.93\text{ mm} \tag{4.1}$$

at the collimating lens with knowledge of the Rayleigh range $z_R = \pi w_0^2/\lambda$.

$$w(z) = w_0\sqrt{1+\left(\frac{z}{z_R}\right)^2} = w_0\sqrt{1+\left(\frac{z\lambda}{\pi w_0^2}\right)^2} \tag{4.2}$$

Solving the quadratic equation for w_0 and keeping the physically relevant solution yields:

$$w_0 = \frac{w(z)}{\sqrt{2}}\sqrt{1-\sqrt{1-\frac{4z^2\lambda^2}{\pi^2 w^4(z)}}} = \frac{0.93\text{mm}}{\sqrt{2}}\sqrt{1-\sqrt{1-\frac{4(250\text{mm})^2(680\text{nm})^2}{\pi^2(0.93\text{mm})^4}}} = 58\ \mu\text{m} \tag{4.3}$$

Thus, the beam diameter at the waist will be $2w_o = 2 \times 58\ \mu\text{m} = 118\ \mu\text{m}$, which adequately covers the 139nm/pixel $\times$ 800 pixels = 111.2 μm field of view.

Light from the SLD passes through custom-designed magnets [71], is scattered by beads in our flowcell, and collected by a 100X 1.4 NA Nikon objective, where it is routed to the high-speed camera (see Figure 4.2 for schematic). The SLD has a similar temporal coherence as an LED, but since the SLD is single-mode,

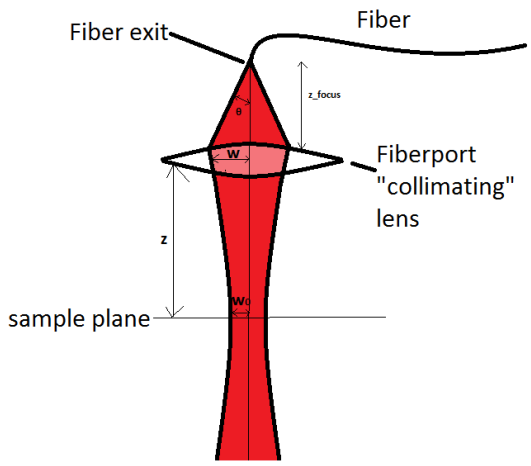

Figure 4.1: A schematic of the superluminescent diode fiber launch system.

we observed bead diffraction patterns to be sharper. Furthermore, we observed that the single-mode SLD permitted improved collimation, resulting in a narrow-waisted beam that minimized clipping of light on the magnets and permitted the magnets to be translated over a larger range.

4.1.2 High-speed video capture

To increase the temporal resolution of the magnetic tweezer, we have used a high-speed camera (Vision Research Phantom v7.3-16GB) in place of the previously used CCD (Jai CV-A10). The high-speed camera can capture up to 180,000 fps at a reduced field-of-view. With a typical 256x256 pixel field-of-view, the camera can capture 35,087 fps and store 6.9 seconds of video on the 16 GB of onboard memory. The subsequent transfer of video frames from onboard camera

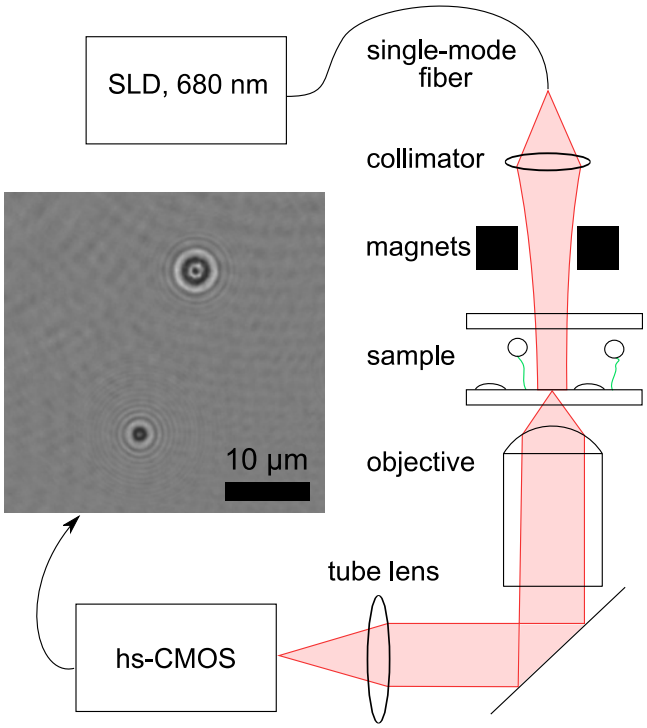

Figure 4.2: A schematic of the high-speed magnetic tweezer with a fiber-coupled Superluminscent Diode (SLD) for illumination and a high-speed CMOS (hs-CMOS) camera for detection. The inset shows a 256x256 8-bit brightfield-normalized still-frame, taken from a video acquired at 35087 fps. The still frame shows a partially molten 2.5 μm diameter reference bead and a 1.05 μm diameter streptavadin-coated magnetic bead, which is tethered to the surface via a DNA hairpin.

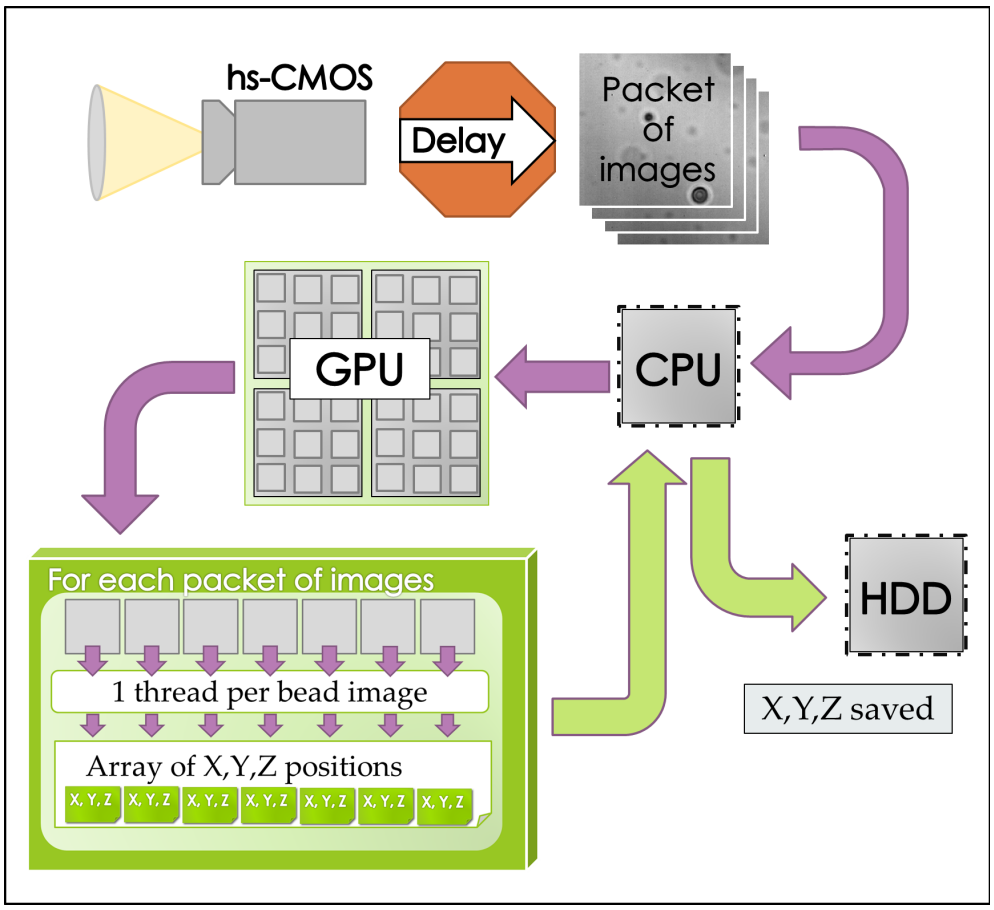

Figure 4.3: Schematic illustration of data flow in our high-speed magnetic tweezer. Images from the hs-CMOS camera are transferred (with delay) via ethernet cable to the CPU. The CPU transfers the data to the GPU, where XYZ coordinates are generated.

memory to the CPU happens via a Gigabit ethernet connection at approximately 25 MB/s, which corresponds to a transfer speed of 380 fps. A schematic of the data-flow in our high-speed magnetic tweezer is shown in Figure 4.3.

To reduce the effect of non-uniform background illumination, we transformed the raw image I_{raw} using bright-field normalization. [25] The bright-field image I_{BF} was taken by manually scanning the sample laterally, and taking the median

image intensity at each pixel of approximately fifty frames. The dark field I_{DF} was taken by blocking the light source. The bright-field normalized pixel intensity for an 8-bit image is then:

$$I_{normalized}(x,y) = 100\left(\frac{I_{raw}(x,y) - I_{DF}(x,y)}{I_{BF}(x,y)}\right) \tag{4.4}$$

A representative bright-field normalized image is shown in Figure 4.2.

4.1.3 GPU-accelerated particle tracking

The goal of a particle tracking algorithm is to output the three-dimensional position of a particle center as a function of time, given a sequence of video frames as input. Existing algorithms can find the position of spherical particles to sub-pixel in-plane accuracy and similar out-of-plane accuracy. [10, 26, 39] Despite their accuracy, existing tracking routines throttle data throughput due to their serial nature. To increase throughput, we implemented a graphics processing unit (GPU) algorithm using CUDA architecture [72] to massively parallelize the task of obtaining three-dimensional particle positions.

We measured bead positions from images using a centroid-finding algorithm frequently used in magnetic-tweezer instruments. [10, 56] The in-plane (X-Y) position of the bead is found by measuring the linear intensity profile along the horizontal and vertical axis of the bead near the center. A cross-correlation of the linear intensity profile with its mirror image is used to find a first guess for the

in-plane particle center. The cross-correlation is fit to a second-degree polynomial near the central point to find the in-plane particle center to sub-pixel accuracy.

Once we have calculated the X-Y position, we can find the out-of-plane (Z) position. First, a radial intensity profile about the X-Y center is compared to a previously generated radial-intensity vs height look-up table. The look-up table is generated using the same in-plane tracking algorithm, but with bead height varied in 100 nm steps by a piezoelectric stage. Second, the look-up-table is interpolated using least squares with polynomial fitting to find the height of the particle.

To capture a high-speed event, we first preview data at approximately 50 frames per second while the camera continuously updates the latest 16GB of video on an internal circular buffer of memory. When we observe an event of interest in the preview data, we trigger the camera to dump the buffer, and the data processing begins. The camera sends packets, each containing multiple camera frames, each containing multiple bead images, from the hs-CMOS to the CPU (see Figure 4.3). The CPU relays the packets via the PCI-express bus to the GPU, where particle positions are determined for all of the beads in the packet. With our tracking algorithm, we have tracked thousands of beads simultaneously and have obtained particle position data at the limit of the ethernet cable image transfer rate. Our GPU-accelerated particle-tracking algorithm is freely available for download at `http://www.engr.ucsb.edu/~saleh`, and can be used by anyone

with an NVidia CUDA 2.0 capable GPU. Our code can be extended to include rotational tracking, bright field normalization, and even alternate methods of particle tracking.

4.1.4 Flowcell Preparation

We prepared glass coverslips by rinsing with acetone, isopropyl alcohol (IPA), de-ionized water, then drying with nitrogen gas, then plasma treating for 10 minutes. A solution of 2.5 μm diameter polystyrene beads suspended in IPA was evaporated onto the bottom coverslip surface to leave randomly dispersed beads that subsequently became the "stuck bead" fiducial markers to track coverslip drift (Figure 4.4). Once the IPA evaporated, coverslips were left on a hotplate for 3 minutes at 145 °C. Sigmacote solution was pipetted onto the coverslip and allowed to air-dry in a fume hood. Residual Sigmacote clumps were removed with an ethanol rinse. The flowcell was assembled by sandwiching a piece of parafilm, cut using a 40 W CO_2 laser (Full Spectrum), between the bottom and top coverslips. The flowcell was placed on a hotplate at 80 °C for 10 minutes to seal the parafilm to the glass.

The double-stranded DNA (dsDNA) used for thermal noise analysis was taken from pGluc-basic 2 vector (NEB). The vector was digested by AvaI to yield fragments of 3392-bp and 1566-bp length (data in Figure 4.5). Our dsDNA molecules have two handles for tethering: a biotin-label and an anti-DIG la-

bel. The dsDNA was left in a fridge for 40 minutes to allow the anti-DIG to non-specifically bind to the Sigmacote surface, leaving sparse surface-anchored dsDNA. Biotin-streptavadin bonds were formed by flowing streptavadin-coated 1.05 μm diameter magnetic beads in TE buffer into the flowcell, and allowing the beads to diffuse around the coverslip surface and find dsDNA molecules for 10 minutes.

DNA hairpin measurements in Figure 4.6 were performed on a DNA hairpin structure described previously, [12] consisting of a 20-bp stem sequence with 55% GC content and a thymidine tetraloop. dsDNA handles were attached via non-palindromic ligation sequences at either end of PAGE-purified DNA oligomer (Integrated DNA Technologies). Abasic sites were also included to provide space between the hairpin stem and handles. For the 5' handle, we generated 1050-bp DNA with a terminal digoxiginin and 15-nt overhang sequence by autosticky PCR. [73] We prepared the 3' handle by annealing a 20-nt oligo with a terminal biotin.

4.2 Experimental Measurements

4.2.1 Stuck beads

To determine the instrumental noise of our system, we measured the position vs time of polystyrene particles stuck to a glass coverslip surface. In Figure

4.4(a) we plot the position versus time of a single particle (raw) and that same particle with the position of a second stuck reference bead subtracted (corrected) in order to compensate for common-mode noise. In Figure 4.4(b) we plot the Allan deviation, the square root of the Allan variance, which characterizes the noise at various timescales. [21,35] In principle, the Allan deviation contains the same information as the PSD graph shown in Figure 4.4(c), but we find that the Allan deviation more clearly illustrates the relevant noise regimes. At very short time scales, below 10^{-4} s, the noise is dominated by the limited accuracy of our particle tracking algorithm. At intermediate times, we see the introduction of common-mode acoustic noise in the raw traces. We note that the common-mode noise is reduced by three orders of magnitude in the lateral direction after reference correction. At times above 0.1 seconds, we see the influence of thermal drift in both the lateral and axial traces. With reference bead correction, the axial noise reaches 0.6 Å at down-sampling times beyond 1/60 s, which compares favorably to previous measurements that attained 5 Å in similar conditions. [10]

4.2.2 DNA tether

The tethered probe particles in magnetic tweezers are micron-sized superparamagnetic beads that fluctuate due to thermal collisions with surrounding water molecules. To a good approximation, the particles can be modeled as massless Brownian particles with drag coefficient α trapped within the constraints of a

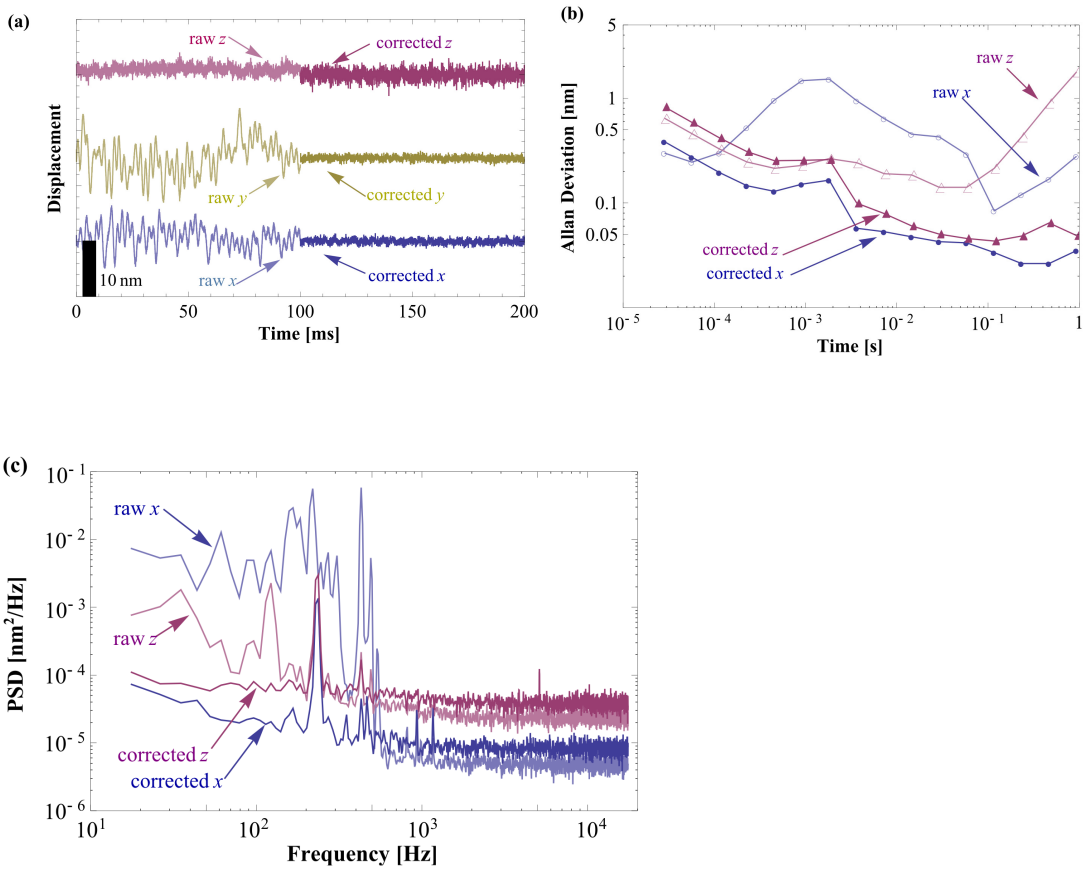

Figure 4.4: Three ways to examine the instrumental tracking error of a magnetic tweezer. Figure 4.4(a) shows the position of a partially molten polystyrene reference bead as a function of time with (corrected) and without (raw) reference bead subtraction. Figure 4.4(b) shows the Allan deviation of bead position as a function of the measurement time, for lateral X and axial Z fluctuations. Figure 4.4(c) shows the PSD of bead motion, with and without reference bead subtraction. For clarity, lateral Y-fluctuation data is not shown in Figure 4.4(b) and Figure 4.4c, but it qualitatively matches the X-fluctuation data.

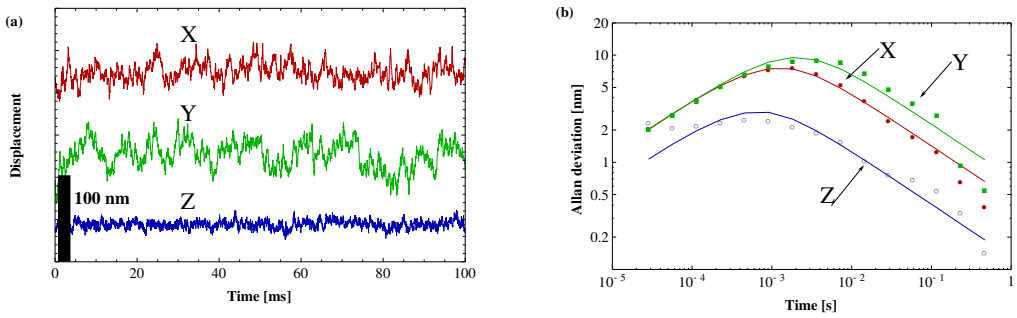

Figure 4.5: The time-domain X,Y,Z positions of a magnetic bead tethered to a 1566 bp dsDNA molecule (Figure 4.5(a)) can be analyzed using Allan deviation (Figure 4.5(b)). Best-fit curves to Allan deviation data give measurements of the trap stiffness κ and probe drag α.

harmonic potential of stiffness κ. In Figure 4.5(b), we fit the analytical equation for the Allan deviation for a tethered Brownian particle [35, 47] to experimental data using a 1566-bp dsDNA molecule in the X and Y directions, resulting in $\alpha_x = 1.78 \times 10^{-8}$ N s/m, $\alpha_y = 1.86 \times 10^{-8}$ N s/m, $\kappa_x = 2.87 \times 10^{-5}$ N/m, and $\kappa_y = 1.61 \times 10^{-5}$ N/m.

We are therefore able to resolve a corner frequency of $f_{c,x} = \frac{\kappa_x}{2\pi\alpha_x} = 256$ Hz, beyond the Nyquist frequency of conventional magnetic tweezers. The Allan variance in the axial Z-direction has added instrumental noise at timescales below 1 ms that makes a direct fit to analytical theory impossible. However, we can measure the length with 1 nm of noise at 100 Hz.

4.2.3 DNA hairpin dynamics

To demonstrate the ability of the high-speed magnetic tweezer to accurately measure a fast biomolecular transition, we measured a DNA hairpin as it fluctuated between a folded and an unfolded state (see Figure 4.6). The upper inset shows a transient closed hairpin state that was only stable for 8 frames at 701.74 fps, or 0.011 s, faster than a single frame of the traditional 60 Hz CCD camera. The right inset is a histogram of particle positions, with a best-fit curve that is a sum of two Gaussian peaks with a separation of 17.6 nm, in reasonable agreement with previous results of 18.1±0.3 nm. [12]

4.3 Conclusion

We have developed a high-speed magnetic tweezer that utilizes a SLD for illumination and a hs-CMOS camera for detection. To handle the increased data throughput of the high-speed camera, we have re-written a particle-tracking algorithm to utilize a GPU for faster data throughput. Our particle tracking results on a dsDNA tether have demonstrated our ability to resolve corner frequencies above 250 Hz. We have accurately resolved DNA hairpin dynamics that were unresolvable with previous generations of magnetic tweezers. We have shown how the high-speed magnetic tweezer has noise below 0.6 Å in three dimensions at a bandwidth of 100 Hz.

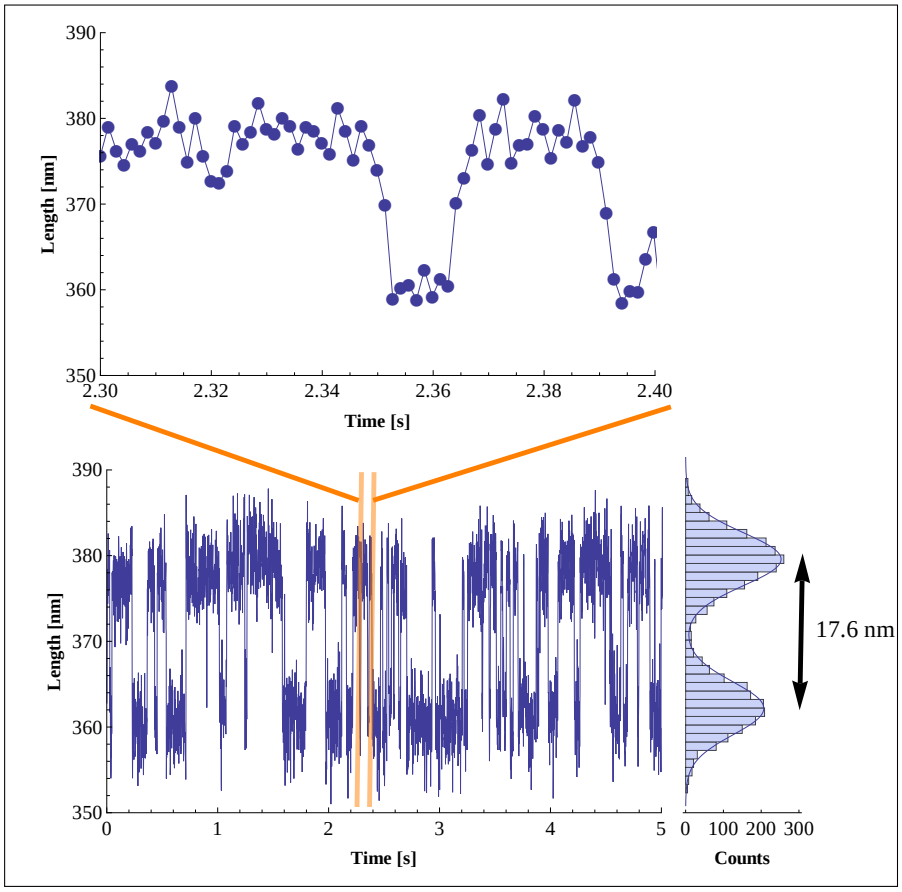

Figure 4.6: Extension trajectory of a DNA hairpin undergoing stochastic folding/unfolding transitions. Data was acquired at 35087 fps, then low-pass filtered to 701.74 fps. Inset shows a 0.011 s residence in the folded state. The histogram of particle positions is well-described by a sum of two Gaussians, separated by 17.6 nm.

Chapter 5

Reduced mechanical vibration and optimization for small beads

In this chapter, I present numerous instrumental advances to further improve the high speed magnetic tweezer. I replace noisy cooling fans with a liquid cooling system, replace the expensive piezoelectric microscope objective focusing system with a stable stage and tube-lens focus system, add a spatial filter to improve per-frame tracking resolution, design and build high-force magnets, and discuss the ideal light source from theoretical principles.

5.1 Mechanically stable stage

The region of the magnetic tweezer that is most sensitive to vibration is the high magnification region (objective, sample). To solidify the mechanical path

between the objective and the sample, it would be ideal to mount them together. However for experimental convenience, it is useful to retain the ability to translate laterally to find beads of interest. For this reason, a sample stage was designed that retained X-Y lateral translation, but eliminated the piezo-electric objective and instead rigidly mounted the objective to the sample stage with a minimized mechanical path. The design and realization are shown in Figure 5.1.

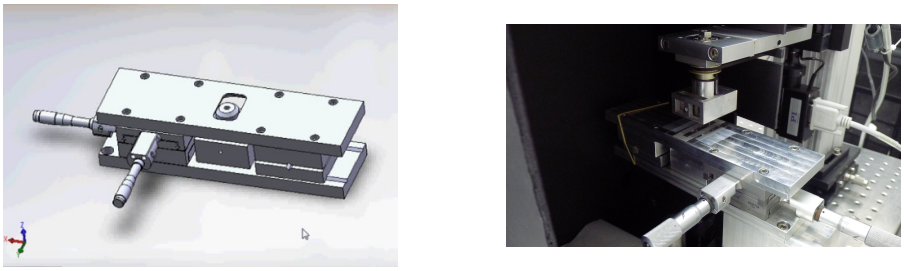

Figure 5.1: A lateral translation stage design and realization.

To quantify the improvement in mechanical noise in the high-speed magnetic tweezer, I tracked "stuck beads," 2 μm diameter polystyrene particles that were affixed to a glass coverslip. In Figure 5.2 I plot the AV for stuck beads before and after the addition of the stable stage.

5.2 Liquid cooling

A stuck bead particle was tracked with the Phantom v7.3 high-speed camera. Without overheating the camera, the cooling fans could be temporarily unplugged for 20 seconds to measure the influence of the fans on tracking error. In Figure 5.3,

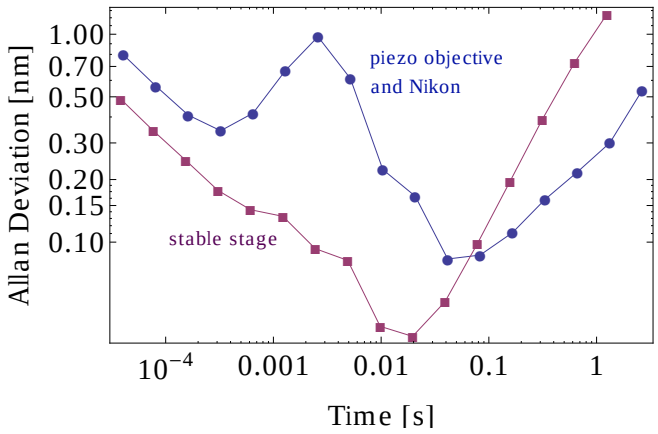

Figure 5.2: AV for a stuck bead in the axial (Z) direction, for the piezo-objective and old Nikon stage, and the new stable stage

the same bead particle tracked with the camera fans plugged in and disconnected. There are clear prominent acoustic noise features in the resulting PSD.

To solve the problem of acoustic noise generated by the fans, a custom liquid cooling setup was designed. The cooling blocks were designed in two parts, with channels to force cooling water through. The two parts were sealed together with a butyl o-ring "gasket" that was coated in vacuum grease to prevent tearing. Figure 5.4a shows a Solidworks model of the copper cooling block, as well as an experimental realization given in Figure 5.4. Full design drawings are included in 6.2.5. In Figure 5.4c is a photograph of the high-speed camera with two such cooling blocks mounted, with external cooling provided by an external radiator with all-copper plumbing to prevent corrosion (Koolance EXT-440CU).

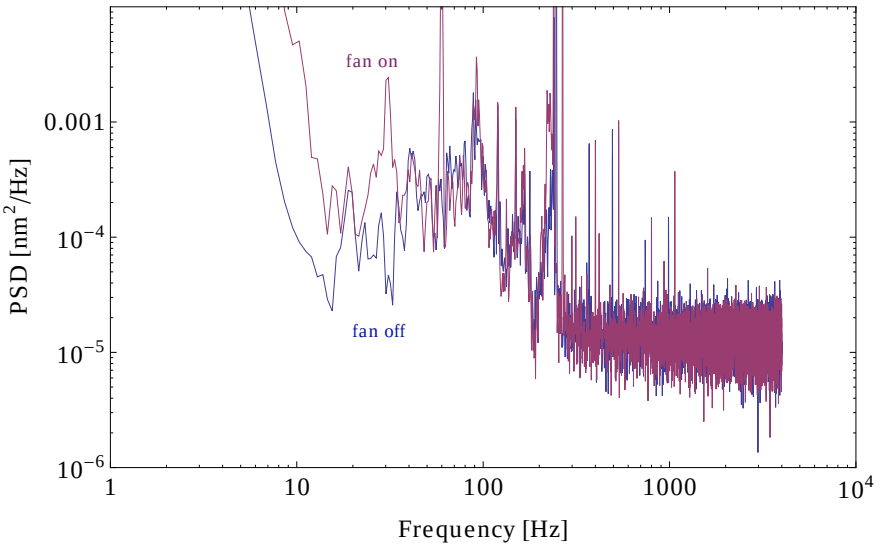

Figure 5.3: The PSD of stuck bead tracking in the x direction, with and without the fans activated.

(a) (b) (c)

Figure 5.4: A Solidworks rendering (a), experimental realization (b), and mounted on a hs-CMOS camera (c)

5.3 Tube-lens focus

In typical magnetic tweezers, a calibration image is created by translating a piezo-electric objective and capturing images at different focal planes for the subsequent z-tracking lookup table (see Section 2). By rigidly mounting the microscope objective to the sample stage, I reduce the mechanical vibration associated with the piezoelectric objective. However, by doing so, the distance between sample and the objective is fixed, and translation of the objective can no longer be used to generate a calibration stack for particle tracking. To solve this problem, I add a retroreflector on a translation stage between the tube lens and the camera, in a similar approach to a previous work which moved the tube lens. [74] The mechanical drive was constructed from the screw drive mechanism from an old syringe pump repurposed to become a linear translation stage. An Arduino with a stepper motor shield was used to drive a stepper motor which controlled the retroreflector position. An experimental realization is shown in Figure 5.5

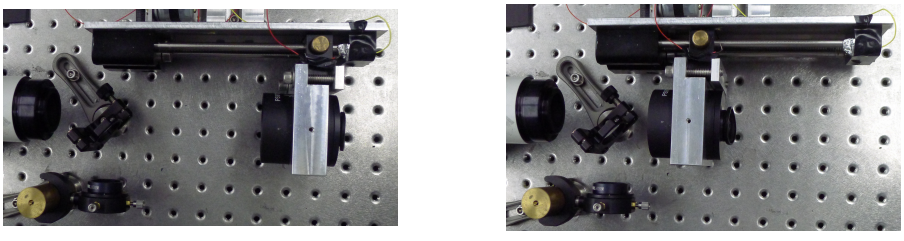

Figure 5.5: A retroreflector on a translation stage (right) is used to adjust the optical path length between the tube lens (bottom) and the camera (left)

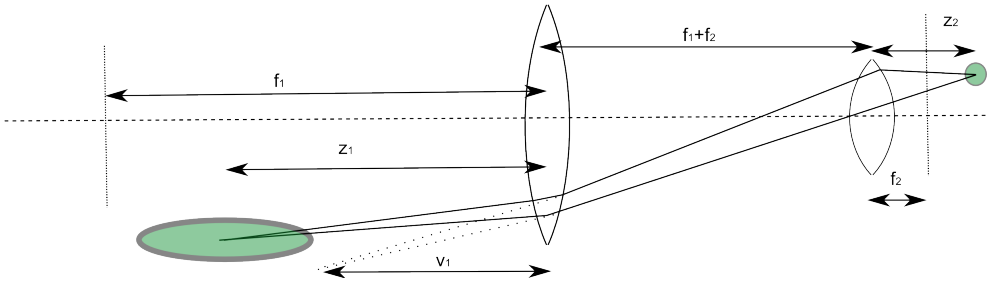

Figure 5.6: A thin lens representation of a translation-stage tube lens. Starting from an in-focus particle at the camera image plane (leftmost green dot) at a distance z_1 from a tube lens with focal length f_1, we create a virtual image at v_1. A microscope objective with focal length f_2 will mean that the particle at a distance of z_2 from the objective.

We can use the thin lens equation ($1/f = 1/s_1 + 1/s_2$) to derive the theoretical magnification of bead images given a translation of the retroreflector. In Figure 5.6 is a schematic showing a bead particle at a distance z_2 from the objective with focal length f_2. A tube lens is placed at a distance of $f_1 + f_2$ from the objective, which ensures that collimated light entering the objective (focused to a point at the back focal plane) is collimated on the other side of the tube lens. To calculate the "axial magnification" $M_{axial} = \frac{\partial z_2}{\partial z_1}$, we can solve the thin lens equations for the objective with f_2 and the tube lens with f_1, for a virtual image with distance v_1 from the tube lens.

$$\frac{1}{f_1} = \frac{1}{z_1} + \frac{1}{v_1} \tag{5.1}$$

$$\frac{1}{f_2} = \frac{1}{v_1 + f_1 + f_2} + \frac{1}{z_2} \tag{5.2}$$

$$z_2 = \left(f_2^{-1} - (v_1 + f_1 + f_2)^{-1}\right)^{-1} \tag{5.3}$$

$$z_2 = \left(f_2^{-1} - ((f_1^{-1} - z_1^{-1})^{-1} + f_1 + f_2)^{-1}\right)^{-1} \tag{5.4}$$

+

$$M_{axial} = \frac{\partial z_2}{\partial z_1} = \frac{f_2^2}{(f_1 - 2z_1)^2} \approx \frac{f_2^2}{f_1^2} = M_{lateral}^2 \tag{5.5}$$

And so, with $f_1 \gg z_1$ the axial magnification M_{axial} scales with the lateral magnification squared, $M_{lateral}^2$. For a typical experiment, with a "100X" microscope objective with $f = 2$mm and a tube lens of $f = 200$mm, we get $M_{axial} = 10,000$. In other words, the retroreflector must move by 100mm to equate to 10μm of equivalent distance in the focal plane.

5.4 Spatial Filtering

Smaller beads reduce thermal noise (see Section 3.5.2). However, smaller beads also scatter less light. Smaller particles scatter less light relative to the unscattered reference beam and result in a relatively low contrast diffraction pattern, and as a result, the per-frame tracking error is limited by the shot-noise limit (see Section 2.4.1). To improve the contrast of images, we can use a spatial filter [75](see Figure 5.7). The spatial filter consists of a piece of glass with a

200 μm diameter metallic spot of 50 Å of Titanium (adhesion layer) and 300 Å of Platinum, in order to attenuate the zero-order beam (reference beam), and thereby enhance the contrast of higher-order fringes with respect to the background. Higher order fringes are the more sensitive to height changes of the bead than small-angle rays (see Section 2.16), and so by attenuating the reference beam we increase the relative contribution of high-angle scattering to bead images, which increases their height informational content. The ideal attenuation of the reference beam is when the amplitude of the scattered light matches the amplitude of the reference light, and interference is maximized (see Section 2.3). The actual fabricated spot was slightly elliptical due to a 26° misalignment of the stage in the e-beam deposition machine.

Although the spatial filter did in fact improve the contrast for small beads, as expected, the SLD could only reach 5000 fps with the attenuated light due to the 2 mW maximum power of the SLD, and thus there was not a significant improvement in tracking accuracy since both setups were effectively scatter-photon-limited. However, since the per-frame accuracy was improved, spatial filtering is a means to improve the informational content of images and so may be an effective solution when processing power or transfer bandwidth is limited, or when the maximum frame-rate of a camera has already been reached.

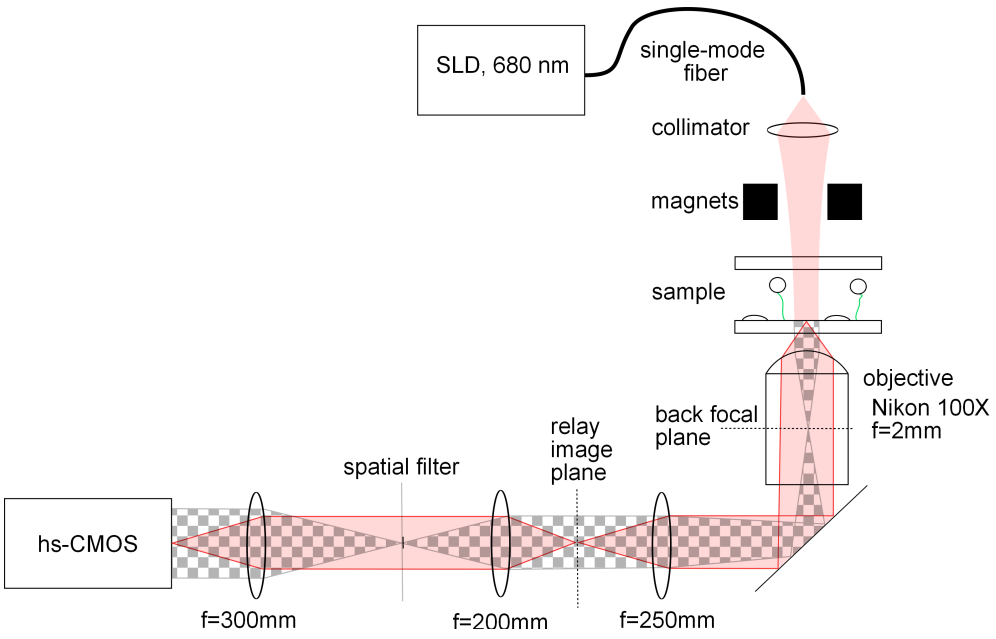

Figure 5.7: Unscattered reference beam light (checkerboard pattern) can be attenuated by a spatial filter, resulting in a spatial high-pass filter. The relative magnitude of scattered light is increased as a result.

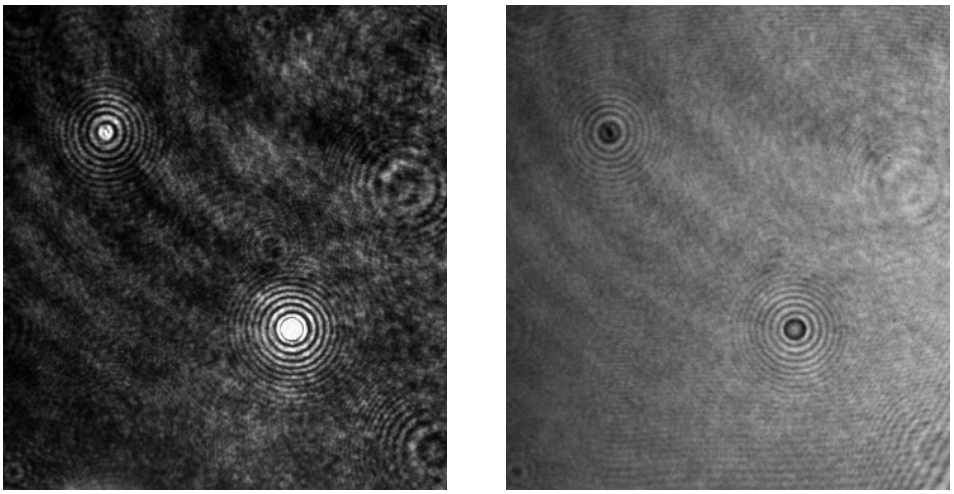

(a) with spatial filter (b) without spatial filter

Figure 5.8: The same stuck beads imaged in a dry flowcell with (a) and without (b) a spatial filter.

5.5 Magnets

5.5.1 Magnetic fields and forces

From the perspective of thermal noise, stiffer tethers and smaller beads result in a lower noise. [14] The high-speed tweezer [69] allows for the measurement of 1.05 μm diameter Myone beads at up to 28 pN of force, using magnets designed by Andrew Dittmore and Jun Lin. [71] For the study of DNA hairpin dynamics, it would advantageous to be able to measure smaller beads at forces sufficient to open DNA hairpins ($>$ 15 pN), since thermal noise would be reduced by a factor of approximately $\sqrt{\frac{1050\ \text{nm}}{536\text{nm}}} \approx \sqrt{2}$ for 536nm diameter beads as compared to the conventional 1.05 μm beads.

5.6 Magnetic Field and gradient

The force on a magnetic particle [76–79] is:

$$\vec{F} = \vec{\bigtriangledown}(\vec{m} \cdot \vec{B}) \tag{5.6}$$

For a magnetic field with field with relatively small gradients in x and y (relevant for a well-aligned setup), the equation simplifies to:

$$F_z = m(B)\frac{\partial B}{\partial z} \tag{5.7}$$

The bead magnetization becomes saturated above approximately 24 mT for Myone beads [76], and thus as long as the field magnitude is well above 24 mT, the net force will be linearly proportional to the gradient, with the saturation magnetization (25.5 pemu for Myones) as the constant of proportionality. It is worth noting that some papers have incorrectly included a pre-factor of 1/2 [47,80] in their calculation of force.

We can estimate the saturation magnetization of 536 nm diameter beads (Microparticles GmbH) by multiplying the saturation magnetization of a Myone by the relative volume and the volume fractions of magnetic content of the smaller bead to obtain: $25.5 \text{ pemu} \left(\frac{536}{1050}\right)^3 \times \frac{0.3}{0.28} = 3.63 \text{ pemu}$. To achieve a goal of 20 pN of force, a field gradient of: $\frac{20 \text{ pN}}{3.63 \ pemu} \times \frac{1 \ T}{1 \ kg/(s^2 A)} \times \frac{10^{12} \ pemu}{10^{-3} \ Am^2} = 5.5 \ T/mm$ is required, which is a factor of 8 higher gradient than a patented design that reaches 0.69 T/m at a distance of 300 μm from the surface. [81] As compared to the high gradient design used in the Saleh Lab [71] $\frac{30 \text{ pN}}{25.5 \text{ pemu}} = 1.1$ T/mm, the gradient of high-force magnets must be made approximately 5 times higher to achieve the goal of sufficiently high force on smaller beads.

5.7 High gradient magnet design

To arrive at a high force magnet design, there are two areas of optimization, both relating to maximizing the field gradient. First, the magnitude of the field gradient can be maximized by maximizing the field in the focusing tips by se-

lecting a material with a high saturation magnetization. Second, the mechanical design of the focusing tips must be optimized for high gradient. Rather than embark on an exhaustive search through the phase space of dimension optimization [82], I examine the fundamental limits from basic principles and then design around those.

5.7.1 Material Selection

The magnets used in the magnet tweezer use permanent magnets with pole pieces to focus the field. [71] However, the maximum field inside the pole pieces is limited by the saturation flux density. The highest saturation flux density of commercially available materials is Iron-Cobalt alloy with $M_0 = 2.5$T. However, for ease of machining I use soft iron, with a saturation flux density of approximately 2.1 T. Superconductors are beyond the scope of this work due to added experimental complications associated with cryogenic cooling.

The other material property of interest for magnetic tweezers optimization is magnetic permeability. The magnetic permeability is the constant of proportionality between magnetic field flux density and magnetic field strength. The relative permeability is the ratio of this constant as compared to vacuum. The relevance of permeability to a magnetic tweezer pole piece is that a higher permeability material will have less leakage of field from inside the pole pieces to the surrounding air. Higher permeability is desirable, but the relative permeability of

soft iron is greater than 150 [83] and so leakage is a minor consideration. The use of high permeability materials with low saturation flux density are a good choice for an oscillatory electromagnet [84] where hysteresis should be minimized, but they are an unimportant choice for the pole piece in a magnetic tweezer where permeability is much larger than 1 and maximum field is the key design parameter.

5.7.2 Theoretical model of magnets

For the purposes of obtaining an analytical solution to achievable magnetic fields in the magnetic tweezer, I assume that we have pole pieces of infinite permeability that are fully saturated to the saturation flux density. Furthermore, I will assume that these pole pieces are uniformly magnetized, so that contributions to the magnetic potential from inside the pole pieces can be ignored, and a simple surface integral can be performed.

5.8 Geometry

A horizontally magnetized pole piece is examined. Following a previously published semi-analytical method [80], we can calculate the theoretical magnetic field given the geometric parameters of the magnets.

If we assume that the surface of the pole pieces are magnetized with M_0, then we can follow a previously published [80] semi-analytical method and write the

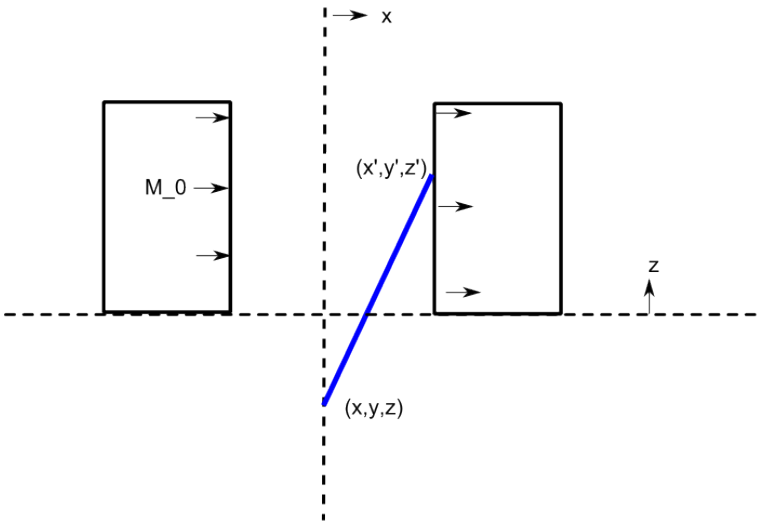

Figure 5.9: A schematic illustration of horizontally magnetized pole pieces

magnetic scalar potential in free space as:

$$\Phi = \frac{1}{4\pi} \oint_S \frac{M_0(x', y', z') \cdot \hat{n}}{\sqrt{(x - x')^2 + (y - y')^2 + (z - z')^2}} \tag{5.8}$$

where S is the surface of the magnet, and $\hat{n}$ is the surface normal vector. We are interested in the magnetic field $B = -\nabla\Phi$.

The integral can be performed by substituting in Cartesian coordinates:

$$\Phi = \frac{1}{4\pi} \int \int \frac{M_0(x', y', z') \cdot \hat{n}}{\sqrt{(x - x')^2 + (y - y')^2 + (z - z')^2}} dy'dz' \tag{5.9}$$

By symmetry, we can say that the field lines will be perfectly horizontal about the line $(x, y) = (0, 0)$, and that the surfaces of the pole pieces are all fully saturated with $M_0(x', y', z') = M_0$, and therefore the gradient reduces to:

$$B = -\nabla\Phi = -\frac{\partial}{\partial x} \left(\frac{2}{4\pi} \int \int \frac{M_0 \cdot \hat{n}}{\sqrt{(x - x')^2 + (y - y')^2 + (z - z')^2}} dy'dz' \right) \tag{5.10}$$

The factor of two comes from the fact that there are two pole tips, with magnetic field M_0 and surface normals $\hat{n}$ exactly opposed, making the resulting integrals for each equal. By approximating the finite sized magnets as infinitely large magnets and integrating from $z' = 0$ to ∞ and $y' = -\infty$ to ∞, we get:

$$B = -\frac{\partial}{\partial x}\left(\frac{M_0}{2\pi}\int\int \frac{1}{\sqrt{(x-x')^2+(y-y')^2+(z-z')^2}}dy'dz'\right) \tag{5.11}$$

Since $x - x'$ is constant in this geometry, the equation simplifies to:

$$B = -\frac{M_0}{2\pi}\int\int \frac{x'-x}{((x-x')^2+(y-y')^2+(z-z')^2)^{3/2}}dy'dz' \tag{5.12}$$

Replacing $x - x'$ with a constant $W/2$, and setting $y = 0$, we get:

$$B = -\frac{M_0}{2\pi}\int_0^\infty\int_{-L}^{L} \frac{W/2}{(W^2/4+(y')^2+(z-z')^2)^{3/2}}dy'dz' \tag{5.13}$$

$$B = -\frac{M_0}{2\pi}\int_{-L}^{L}\int_0^\infty \frac{W/2}{(W^2/4+(y')^2+(z-z')^2)^{3/2}}dz'dy' \tag{5.14}$$

$$B = -\frac{M_0 W}{4\pi}\int_{-L}^{L} \frac{1}{(W^2/4+(y')^2)}\left(1+\frac{z}{\sqrt{W^2/4+(y')^2+z^2}}\right)dy' \tag{5.15}$$

$$B = -\frac{M_0}{2\pi}\left[tan^{-1}\left(\frac{y'z}{W/2\sqrt{W^2/4+y'^2+z^2}}\right)+tan^{-1}\left(\frac{2y'}{W}\right)\right]_{y'=-L}^{y'=L} \tag{5.16}$$

because $tan^{-1}(-L) = -tan^{-1}(L)$, this simplifies to:

$$B = -\frac{M_0}{\pi}\left[tan^{-1}\left(\frac{Lz}{W/2\sqrt{W^2/4+L^2+z^2}}\right)+tan^{-1}\left(\frac{2L}{W}\right)\right] \tag{5.17}$$

In the limit of infinite pole pieces, $L \to \infty$ this reduces to:

$$B = -\frac{M_0}{\pi}\left(tan^{-1}\left(\frac{2z}{W}\right) + \frac{\pi}{2}\right) \tag{5.18}$$

We can easily verify that the superparamagnetic particles will be saturated within a few mm of the pole tips, since they are saturated at 25mT = $M_0/100$. However, since what we actually care about is the gradient in the magnetic field, which gives rise to a force on the paramagnetic particles, we can calculate:

$$\frac{\partial B}{\partial z} = \frac{M_0}{\pi}\left(\frac{2W}{W^2 + 4z^2}\right) \tag{5.19}$$

By minimizing, we can find that for a given distance between the magnets and the bead (limited by the flowcell) of z_{min}, the maximum gradient can be achieved by setting the magnet tip gap equal to twice the bead-tip distance

$$W = 2z_{min} \tag{5.20}$$

In the conventional flowcell design, a layer of Parafilm and a # 0 coverslip define the minimum distance z_{min} of the magnet tips to the surface-tethered magnetic particles as 128 μm + 130 μm = 258 μm. To achieve a significantly smaller gap size, a new ultra-thin flowcell was created using a rectangular capillary (Wale Apparatus) glued to a coverslip using glass-glass-glue (Loctite) and with fluidic access ports created using a ring of hydrophobic vacuum grease (Dow Corning). Figure 5.10 shows a schematic of the assembly. The distance z_{min} is defined by the depth of the flowcell cavity and the thickness of the glass top surface:

$z_{min} = 30\ \mu\text{m} + 30\ \mu\text{m} = 60\ \mu\text{m}$. To maximize the gradient (see Equation 5.20) the tip-tip spacing of the magnets is set to 120 μm.

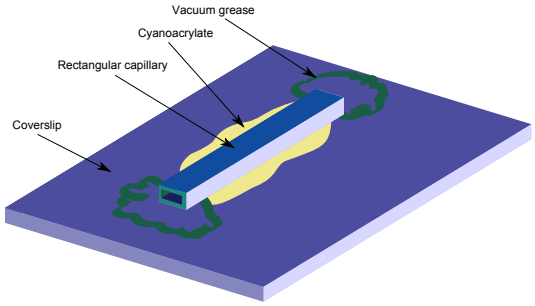

Figure 5.10: A schematic of ultra-thin flowcells

With $W = 120\mu$m and $z > 60\ \mu$m, the theoretical gradient using Equation 5.19 is:

$$\frac{\partial B}{\partial z} \leq \frac{M_0}{\pi}\left(\frac{2W}{W^2 + 4z^2}\right) \tag{5.21}$$

Setting $M_0 = 2.1$ T, a reasonable value for the saturation flux density of soft iron [85], we get: 5.57 T/mm, slightly above the target value of 5.5 T/mm.

5.9 Finite Element Simulations

Together with Zachary Hockenbery, Finite Element Simulations were performed in COSMOS software. Variable distances between the magnet tips were entered: 50, 100, 150, 200, 300, 400 μm.

Upon comparison of the theory developed in Equation 5.19 with the COMSOL results in Figure 5.12, it is clear that the magnetic field is underestimated in the

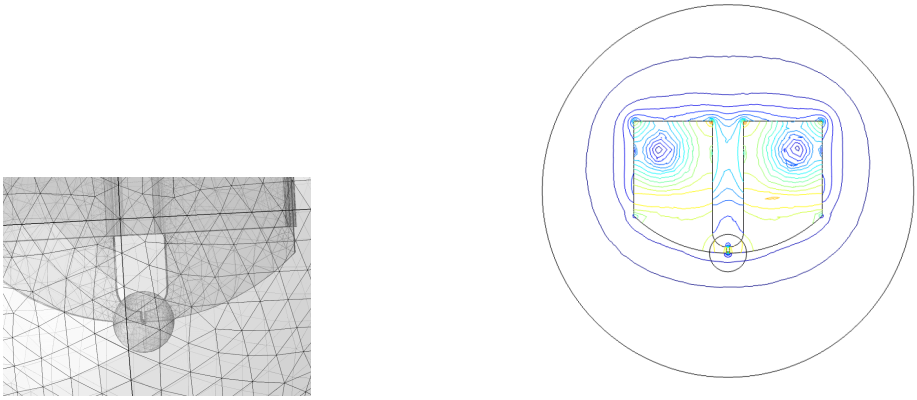

(a) (b)

Figure 5.11: Screenshots from COMSOL magnetic simulation software of 3D magnet tips including the mesh used for simulation (a) and a cross-section of a result (b).

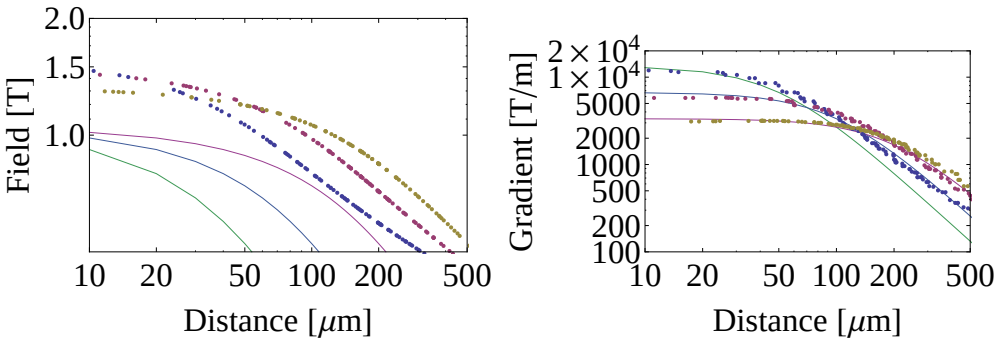

Figure 5.12: The simulated magnetic field (a), and gradient (b), using the analytical expression in Equation 5.19 (solid lines) and using COMSOL (points).

analytical theory. However, the gradient at small distances, which depends most strongly on the field lines that extend from the nearest points on the surface of the pole pieces, shows a remarkable similarity to theory. Discrepancies in both the magnitude of the field at all distance, and the gradient of the field at large distance can be attributed to the finite permeability of the magnets in COMSOL as compared to the infinite permeability used in the theory, which will result in "leaking" field lines from the edges of the pole pieces. The optimal tip-spacing predicted in Equation 5.20 is very nearly matched by the COMSOL predictions, although the crossover occurs at slightly larger distances in the finite element simulation than it does in the analytical theory. This suggests that $W < 2z$ may give even higher gradients than the analytical theory.

5.10 Experimental Realization

The old soft iron tips from a previous magnetic tweezer [71] were used in combination with a custom machined aluminum housing built in the UCSB COE Machine Shop. The gap between the tips was set to approximately 120μm by wedging a metal shim of known thickness between the two pole pieces and then tighetning the rest of the assembly.

The small-gap magnets were tested using a thin flowcell (see Figure 5.10). The gradient prediction from COMSOL simulation can be converted to Force with $\vec{F} = m(B)\frac{\partial B}{\partial z} = 3.63 \text{ pemu}\frac{\partial B}{\partial z}$. A force vs magnet position curve was generated for

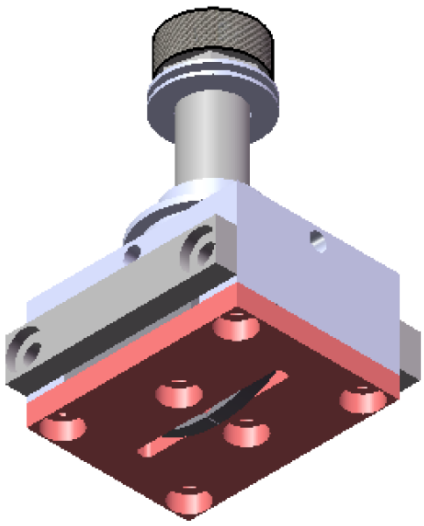

Figure 5.13: A Solidworks rendering of a magnetic tweezer with focusing tips separated by 120 μm. Detailed mechanical drawings can be found in the Appendix.

experimentally measured DNA hairpins. Forces were obtained using the inverted pendulum model for DNA [47], which gives $F = \kappa_x * L$ and $F_y = \kappa_y * (L + R)$, yielding two independent measurements for force from a given trajectory. The predicted behavior of the magnet tips was compared with experiment in Figure 5.14.

The new high-gradient magnets and ultra-thin flowcell were successfully able to open a DNA hairpin using a small 536nm bead, which reduces thermal noise by a factor of $\sqrt{2}$ as compared to the conventional 1.05 μm beads used in magnetic tweezers.

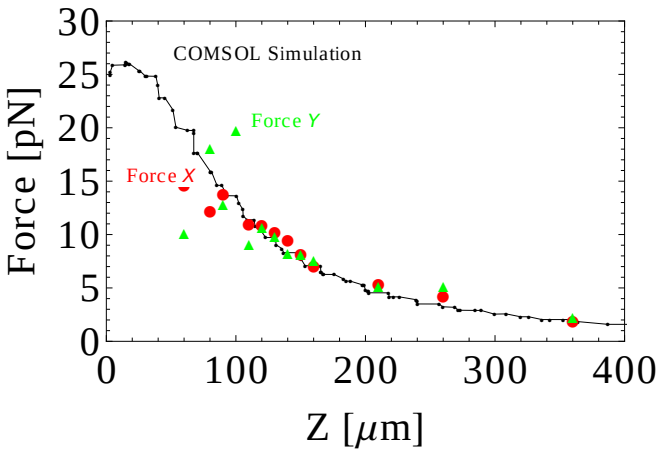

Figure 5.14: The force applied to 536nm beads from experiment as compared to COMSOL simulation

5.11 Illumination source

The magnetic tweezer tracks particle position by imaging the the interference pattern of a reference wave (typically a collimated LED) and scattered light from a probe particle. The ideal light source creates high quality interference patterns, has a high power, and does not suffer from parasitic noise.

The ideal illumination source for magnetic tweezers is:

- focused onto a spot on the focal plane (approximately 100 μm diameter)
- temporally incoherent to reduce speckle (spectral width at least 10 nm)
- collimated to allow the light to pass through magnet tips (angular divergence of less than 10 degrees)
- a maximum number of spatial modes to reduce speckle

- bright enough to allow tracking at 80,000 frames per second ($> 2{\times}10^5$ W/m^2)

Speckle

Stray reflections, dust particles in the optical path, and contamination in the immersion oil or flowcell, all create undesired scattered light, which interferes with the reference beam and creates a 'speckle' pattern. Speckle noise is difficult to distinguish from Lorenz-Mie particle scatter signal, and the speckle therefore contributes to the resulting tracking resolution. The speckle contrast can be empirically described [86, 87] by the speckle contrast $C = \sigma_I / \langle I \rangle$. The speckle can be reduced by increasing the number of spatial modes M, and the resulting speckle contrast scales [86] as: $C \propto 1/\sqrt{M}$.

Speckle noise is indeed the limiting factor on particle tracking resolution at low frequencies. This can be proven by capturing a particle-free background at 2000 fps that includes speckle and electronic noise, and then superimposing a simulated particle image onto this background and tracking its position vs time (nominally constant position). The result is a particle trajectory that displays low-frequency noise (see Figure 5.15). The simulated bead noise matches the results from a stuck bead. Thus, the remaining noise is due to the optical speckle noise and not the mechanical vibration of the stage.

Thus, it is desirable to reduce speckle by choosing an ideal light source. However, both the temporal and spatial coherence will deteriorate the per-frame par-

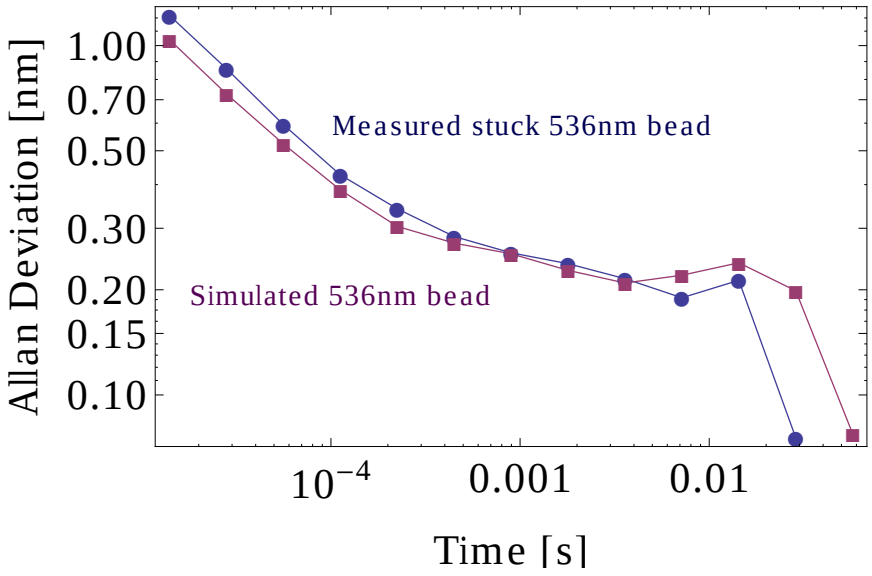

Figure 5.15: The AV of bead motion in the axial (z) direction for a simulated constant intensity bead image superimposed on a fluctuating speckle background

ticle tracking error (as calculated in Section 2.3) due to a blurring of high-order diffraction rings. This effect is schematically shown in Figure 5.16

Temporal Coherence

The temporal coherence can be quantified by the coherence length l_c, which is the characteristic distance over which wavefronts are in-phase (see Figure 5.16). Assuming a Gaussian intensity vs wavelength, a light source with a central wavelength of λ_0 and a spectral width of $\Delta\lambda$ has a coherence length of:

$$l_c \approx \frac{\lambda_0^2}{\Delta\lambda} \tag{5.22}$$

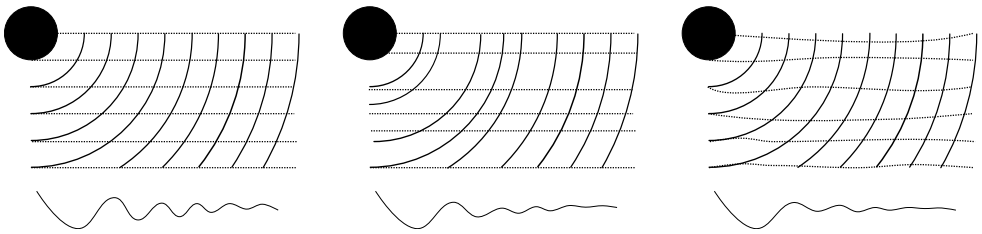

(a) Perfectly coherent illumination (b) Temporally incoherent illumination (c) Spatially incoherent illumination

Figure 5.16: A schematic influence of how both temporal and spatial coherence deteriorates the diffraction patterns and thus the per-frame tracking

which for a superluminescent diode with a central wavelength of $\lambda_0 = 681$ nm and a spectral width of $\Delta\lambda = 7$ nm results in a coherence length of $l_c \approx 66$ μm. The non-Gaussian nature of the superluminescent diode light source (some peaked features) result in slightly longer coherence length. Nonetheless, 66 μm is higher than the typical range of bead motion, and longer than the typical length over which diffraction fringes must remain coherent (approximately 15 interference fringes corresponds to 10 μm), but is not so high that stray reflections from the microscope objective (working distance $\approx$ 200 μm)and other surfaces are detrimental (see Section 2.5). Thus, a spectral width of approximately 10 nm is ideal.

Spatial Coherence

A spatially coherent light source (e.g. one coupled through a single-mode fiber, focused to a diffraction limited spot) has all wave-fronts parallel, and thus

maximizes the number of coherent interference fringes that contribute to particle tracking. A spatially coherent source has problems experimentally because out-of-focus particles will create interference patterns on the image plane, whereas a spatially incoherent source will average out the out-of-focus images. However, a spatially coherent source has the advantage of allowing a collimated beam to pass through the magnet tips.

The number of spatial modes in a light source can be approximated [88] as:

$$N = \left(\frac{\pi \ \mathrm{NA} a}{\lambda} \right)^2 \tag{5.23}$$

For an LED with an emission width of 100 μm, at a wavelength of 0.6 μm, "collimated" at NA 0.1, this corresponds to 2700 modes. Each mode has an independent speckle pattern, so it is no wonder that speckle is not a problem with LED illumination! An angular divergence of approximately 10 degrees, corresponding to NA=0.1, or approximately 3000 spatial modes, is ideal, as this maximizes the number of spatial modes while still allowing the light to pass through the magnet tips, and not have a significant detrimental influence on tracking.

Brightness

The brightness of a light source must allow for high-speed tracking. Empirically, I found that SLD was bright enough to track at beyond 80,000 fps, which makes it a good starting point for the required brightness for high-speed tracking.

The SLD used has 2 mW of power concentrated onto the sample plane into a Gaussian spot of approximately 1×10^{-4} m diameter (see Section 4.1.1), for an irradiance of: 25W/cm^2 within the required NA<0.1. In comparison, a Quartz Tungsten Halogen bulb or Xenon Arc will both have less than 2 W/cm^2, which explains why they have failed to achieve the highest tracking rates [89].

5.11.1 Ideal Light Source

The ideal light source for a magnetic tweezer would have the spectral width of 10nm, at least 1000 independent spatial modes, and a brightness of at least 25W/cm^2, focused onto a an approximately 100μm diameter spot, with an angular divergence of less than 10 degrees. The recent alternative light sources in high-speed magnetic tweezers [69, 89, 90] have failed to meet at least one of the three specifications (spectral width, spatial modes, brightness).

In Figure 5.17 is a diagram that illustrates the combination of spectral width, spatial modes, and brightness that would make an ideal light source for magnetic tweezers.

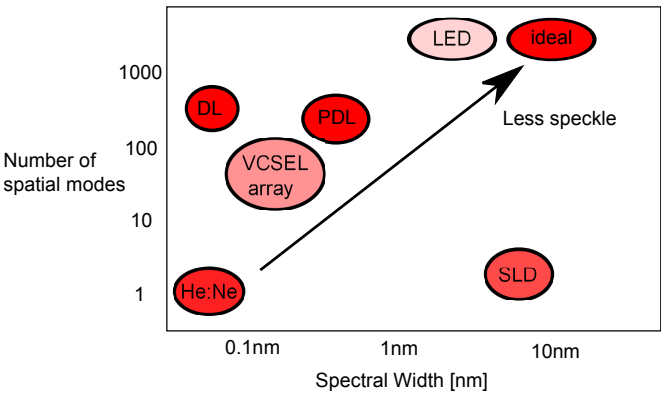

Figure 5.17: A schematic diagram of various light sources and their respective coherence lengths (x-axis), number of spatial modes (y-axis), and brightness (shaded ovals). To reduce speckle, a large spectral width (low coherence length) is desired, as well as a large number of spatial modes, and a high brightness.

Chapter 6

Future outlook

In this chapter, I provide an overview of the potential applications of the instrument I have developed, and further improvements that could improve resolution further.

6.1 Scientific applications

A high-resolution magnetic tweezers such as the one developed in this thesis is most useful where a stable external force is required and where dynamics in the $10 - 100$ Hz range are of interest.

6.1.1 Hairpin dynamics

SMM studies of biopolymer folding are a new method for understanding microscopic dynamics, yet could have an issue in resolving underlying molecular

dynamics by the influence of the bead and tether. For example, the rate at which a DNA hairpin (see Section 4.2.3) opens and closes is not simply a function of the diffusion coefficient of DNA as it explores its potential energy landscape. The rate of hopping with tethered beads is also a function of the bead and handle that connect to it [91]. To test the theoretical predictions of bead size and tether properties on the dynamics of single molecule experiments, it may be possible to measure a DNA hairpin in a magnetic tweezer with varying bead sizes and solution viscosity, to measure the influence of bead drag on hairpin dynamics. Such a study would have implications for other measurements of single-molecule dynamics.

6.1.2 Helicase dynamics

The motor proteins DnaB helicase unzips dsDNA ahead of the replication machinery of the cell. However, it is currently unknown how big the steps are that this molecule takes. Crystal structures and single-molecule measurements have hinted at various step sizes. A recent crystal structure of DnaB helicase suggested a lock-washer configuration of the hexameric helicase, with a 2bp step size, [92] whereas previous X-ray crystal structures of the viral E1 helicase suggested 1 bp steps. [93] Single-molecule studies with insufficient resolution to directly measure steps have given estimates of step size based on the match between force-velocity curves and theoretical models with varying step size. A measurement of gp41

suggested a 1 bp step size, [94] whereas similar measurements of T7 gp4 helicase suggested a 2bp step, [95] A bulk quenched-flow measurement suggested a 1 bp step for DnaB. [96]

A recent review article [97] summarized the current state of the art:

> Thus far, there has not been a real-time measurement of DNA unwinding by hexameric helicases with sufficient spatiotemporal resolution to detect the elementary steps of unwinding despite many interesting single-molecule analyses performed on hexameric helicases. In the only published report of resolving individual steps by a ringshaped motor on DNA (Moffitt et al.,2009), the DNA packaging motor from ϕ29 was shown to package dsDNA in a hierarchy of noninteger, 2.5 bp steps, pausing after packaging 10 bp.

My preliminary experiments with measuring step size were unsuccessful, due in part to extra low-frequency noise above the expected Lorentzian of bead motion.

6.1.3 Optimum tether length for helicase experiments on a hairpin magnetic tweezer assay

In a typical hairpin experiment in a magnetic tweezer [11], a tether consists of: a single-stranded DNA (ssDNA) loading region to allow helicase to bind and load, a hairpin to convert an unzipped dsDNA base-pair into a change in bead height, and a dsDNA handle, to keep the bead away from the surface. If the handle is too short, the surface-induced viscous drag on the probe particle will

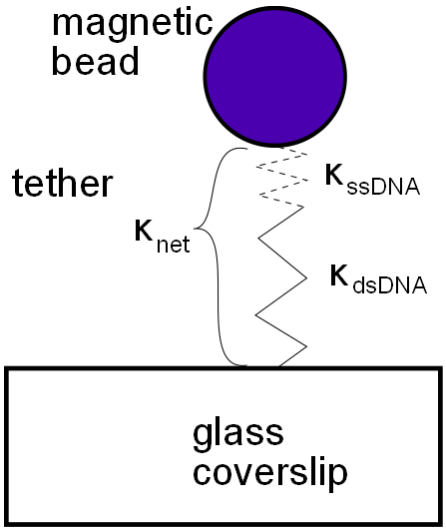

Figure 6.1: A schematic of combined ssDNA and dsDNA

increase the thermal noise, and if the handle is too long, the tether stiffness will decrease, and the thermal noise will increase.

To calculate the optimal tether length for a given assay, we can use the Faxén correction [67] for probe drag perpendicular to a flat surface:

$$\alpha\perp = \frac{6\pi\eta R}{1 - \frac{9R}{8h} + \frac{R^3}{2h} - \frac{57R^4}{100h^4} + \frac{R^5}{5h^5} + \frac{7R^{11}}{200h^{11}} - \frac{R^{12}}{25h^{12}}} \tag{6.1}$$

To model a tether that is composed of ssDNA and dsDNA, we assume that the system behaves as two springs in series, with $\kappa_{net} = \left(\kappa_{ssDNA}^{-1} + \kappa_{dsDNA}^{-1}\right)^{-1}$. For this analysis, angular fluctuations [36] are ignored, since they are dependent on the degree to which the tether is bound to the bead with respect to the preferred magnetization axis of the bead (mistether). If we find a lucky tether with a small mistether, then rotation can be ignored.

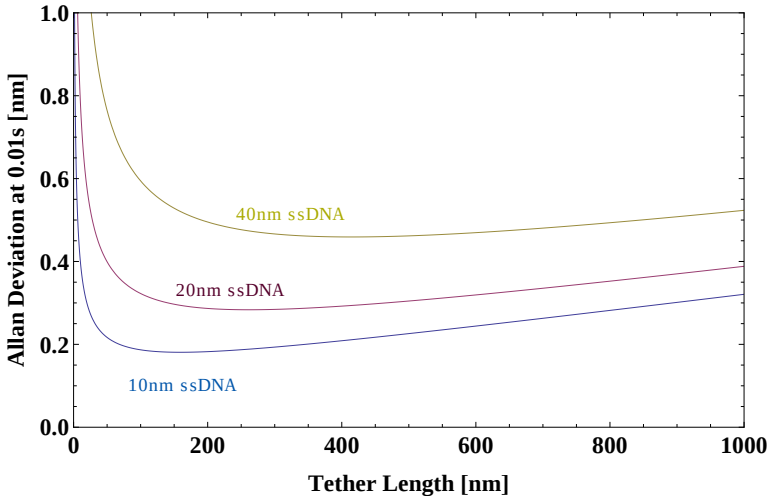

Figure 6.2: The theoretical Allan deviation at $\tau = 0.01s$, as a function of dsDNA handle length at a simulated force of 10 pN. The three curves correspond to different ssDNA length: 10 nm (blue), 20 nm (red) and 40 nm (yellow).

To calculate the stiffness of the dsDNA section, we use a numerical approximation to the extensible worm-like chain model, ignoring finite-size effects, [68] given by:

$$F = \frac{k_B T}{L_p}\left[\frac{1}{4\left(1 - z/L_0\right)^2} - \frac{1}{4} + \frac{z}{L_0} + \sum_{i=2}^{i\leq 7} \alpha_i \left(\frac{z}{L_0}\right)^i\right] \tag{6.2}$$

The stiffness $\kappa = \frac{\partial F}{\partial z}$ of dsDNA at high force is found numerically.

The single-stranded region cannot be described by the worm-like-chain, [98] but an empirical relation [99] for the force-extension behavior at forces greater than 1 pN is:

$$z = L_0\left[\gamma \ln\left(\frac{F}{F_C}\right) + 1\right] \tag{6.3}$$

solving for $\kappa = \frac{\partial F}{\partial z}$ we get:

$$\kappa_{ssDNA} = \frac{F}{L_0 \gamma} \tag{6.4}$$

Solving for the Allan deviation (Equation 3.23) for a given ssDNA length and dsDNA length, with a 1 μm diameter bead, we get the theoretical results shown in Figure 6.2. For ssDNA of 40 nm (10 nm of loading zone and 30 nm for stepping), the theoretical optimum tether length is approximately 400 nm. This theoretical result should help guide future experimentalists.

6.2 Further instrument improvements

The magnetic tweezer still has a long way to go before the instrumental limitations of particle tracking catch up to the theoretical limitations of quantum limited particle tracking. The liquid water phase in which most biomolecules operate presents a challenge to low-noise tether measurement, since the fluid imparts momentum on the bead which obscures tether length measurements. To track smaller and smaller particles, more advanced optical schemes will be required, such as the one I presented which attenuates the reference beam. Use of smaller particles in a magnetic tweezer will require increasingly high gradient magnetic fields in order to apply relevant forces. Stiffer tethers can also increase the corner frequency of measurements [100].

6.2.1 Heterodyne detection

It may be possible to perform heterodyne detection to accurately measure the phase of scattered light [101, 102]. The position of the bead would in this

case be determined by the phase of the interference between scattered light and a frequency-shifted reference. This would involve significant experimental effort to implement, requiring acousto-optic modulators, and frequency-stable oscillators. However, a potential benefit could be that low-frequency position measurements would no longer be limited by speckle, but instead by the phase stability of the two oscillators, which often approaches 1 part in 10^{12}.

6.2.2 Tethers in air

To reduce the Langevin noise would require reducing the viscosity and thereby the drag coefficient on the bead particle. If the tether could bridge between a liquid and vapor phase, with biomolecule activity of interest in liquid phase and probe particle suspended in vapor phase, then the particle motion would no longer be limited by Langevin fluctuations of a bead in water, but by a bead in air, which would significantly increase the corner frequency which scales as $f_c \propto 1/\eta$. DNA nanopores could potentially act as the conduit between liquid and vapor phase, so that the bead would be in vapor phase, the tether extending between liquid and vapor. This could perhaps be achieved using DNA nanopores. However, it would be a monumental experimental achievement to actually achieve this in practice.

A more feasible improvement would be to add a stiff handle [100] which would increase κ and therefore reduce the thermal noise. This could for example be accomplished by making handles using DNA bundles. [103]

6.2.3 Further reductions in noise

There are still numerous instrumental issues which can be improved, most notably the speckle noise at low frequencies, higher speed tracking with brighter light sources, and use of smaller beads. A brighter light in combination with a spatial filter would improve the spatial resolution. The same effect could be accomplished by decreasing the focal spot size of the reference illumination light source, to shrink from illuminating the entire field of view to just illuminating one or two beads. However, the current generation illumination was optimized for the magnet translation stage, and so a more focused beam would require a redesign of the optics performed in Section 4.1.1.

As outlined in Secion 3.2, it would be interesting to track the out-of-plane rotation angle of magnetic beads. Perfectly spherical beads with a uniform refractive index will have a scatter pattern that does not vary with rotation angle. However, perhaps the imperfect distribution of nanoparticles or the asphericity can be exploited to gain information about the out-of-plane rotation of the bead.

Higher-speed cameras with brighter light sources will only be needed once the thermal limit has been reached for smaller beads. For now, the excess low-

frequency noise that is present with the single spatial-mode illumination of a superluminescent diode is a problem that needs the be addressed, for example by switching to a bright multi-mode light source with a broad spectral width.

6.2.4 New light sources

To reduce speckle noise, experiments with multiple spatial-mode light sources could be performed. These types of light sources are being actively developed [86,104,105] and perhaps one of them could find application in the magnetic tweezer. It is technically difficult to start with a bright, multiple spatial mode light source with a relatively narrow spectral width such a Pulsed Laser Diode (PLD) and try broaden the spectral width. What might be technically possible is to start with bright and spectrally broad source such as a Superluminscent Diode (SLD) and increase the number of spatial modes by destroying the spatial coherence by means of a rotating ground glass, vibrating multimode fiber [106], or other creative means. The key will be to destroy the spatial coherence within a small scatter angle to allow light to pass through the magnets, and also retain the brightness. Scattering in the Fourier conjugate plane will likely result in huge losses in intensity, and therefore: placing a moving diffuser in a relay image plane of the 100 μm focal spot (before sample plane) may yield a spatially incoherent reference wave with a broad spectral width of desired brightness.

6.2.5 General conclusion

The magnetic tweezer has a bright future. Experimentalists will continue to drive advances, which will further expand our understanding of the world. I look forward to seeing how things progress.

Appendix

A mechanically stable stage

Attached are Solidworks drawings of the stable microscope stage, which houses an objective centrally, and allows lateral translation of the sample with minimal axial vibration. These were manufactured by the author in the UCSB COE machine shop.

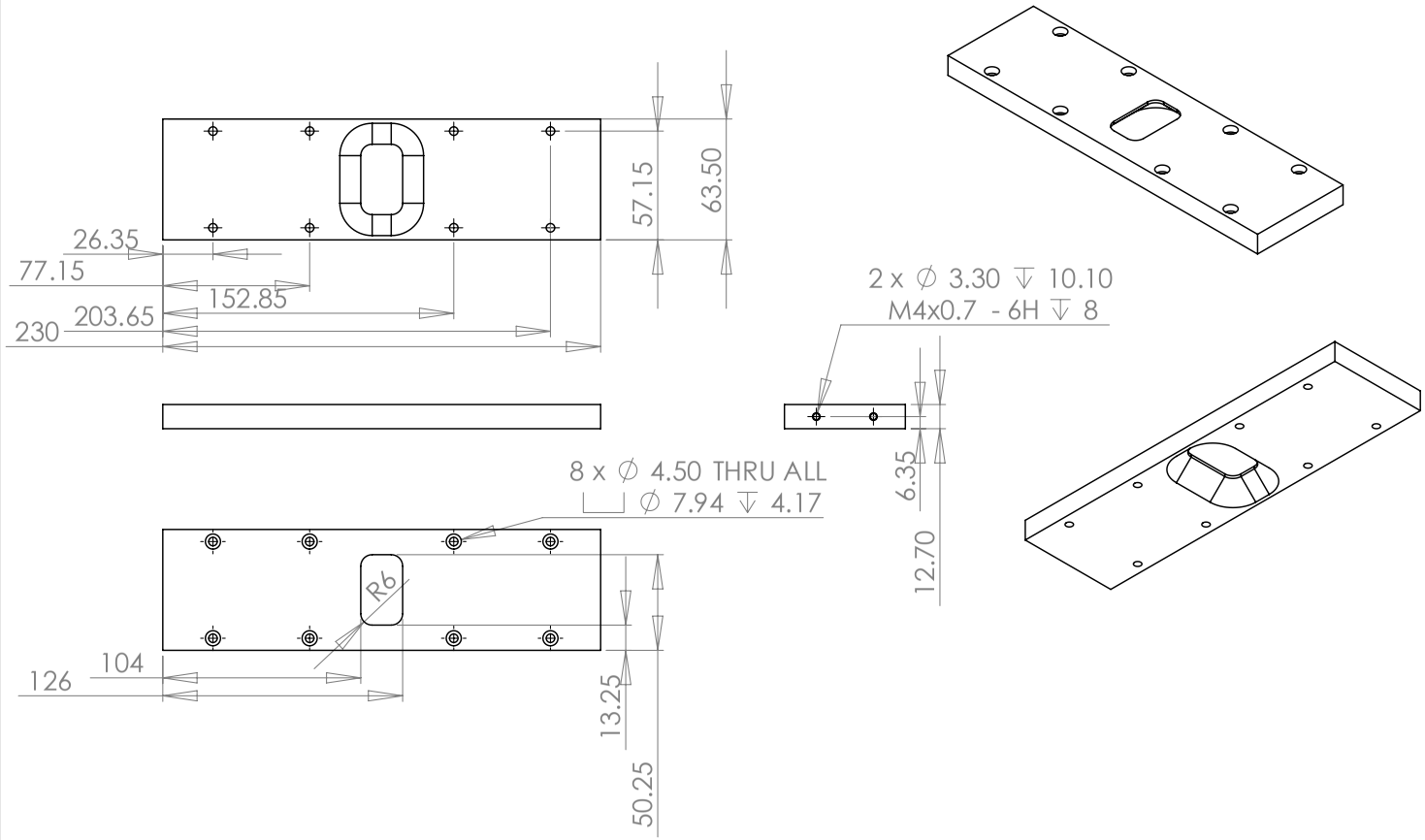

	NAME	DATE
DRAWN	Bob Lansdorp	
CHECKED		
COMMENTS:		

UNLESS OTHERWISE SPECIFIED:
DIMENSIONS ARE IN MM

MATERIAL

FINISH

TITLE:

stablestage

SCALE: 1:3 | SHEET 1 OF 7

The Saleh Lab at UCSB

5 4 3 2 1

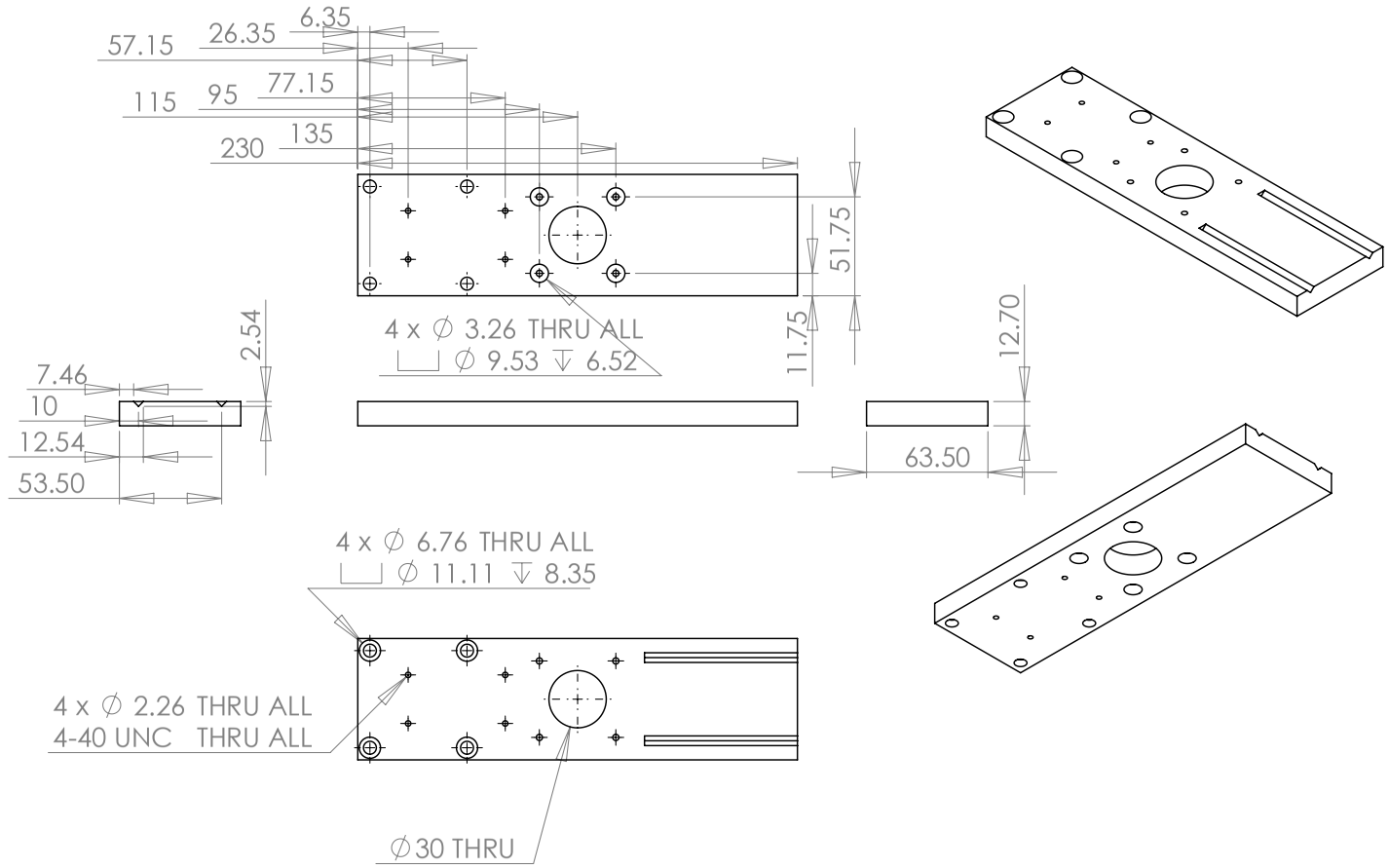

	NAME	DATE
DRAWN	Bob Lansdorp	
CHECKED		

COMMENTS:

UNLESS OTHERWISE SPECIFIED:
DIMENSIONS ARE IN MM

MATERIAL

FINISH

TITLE:

stablestage

SCALE: 1:3 | SHEET 2 OF 7

The Saleh Lab at UCSB

5 4 3 2 1

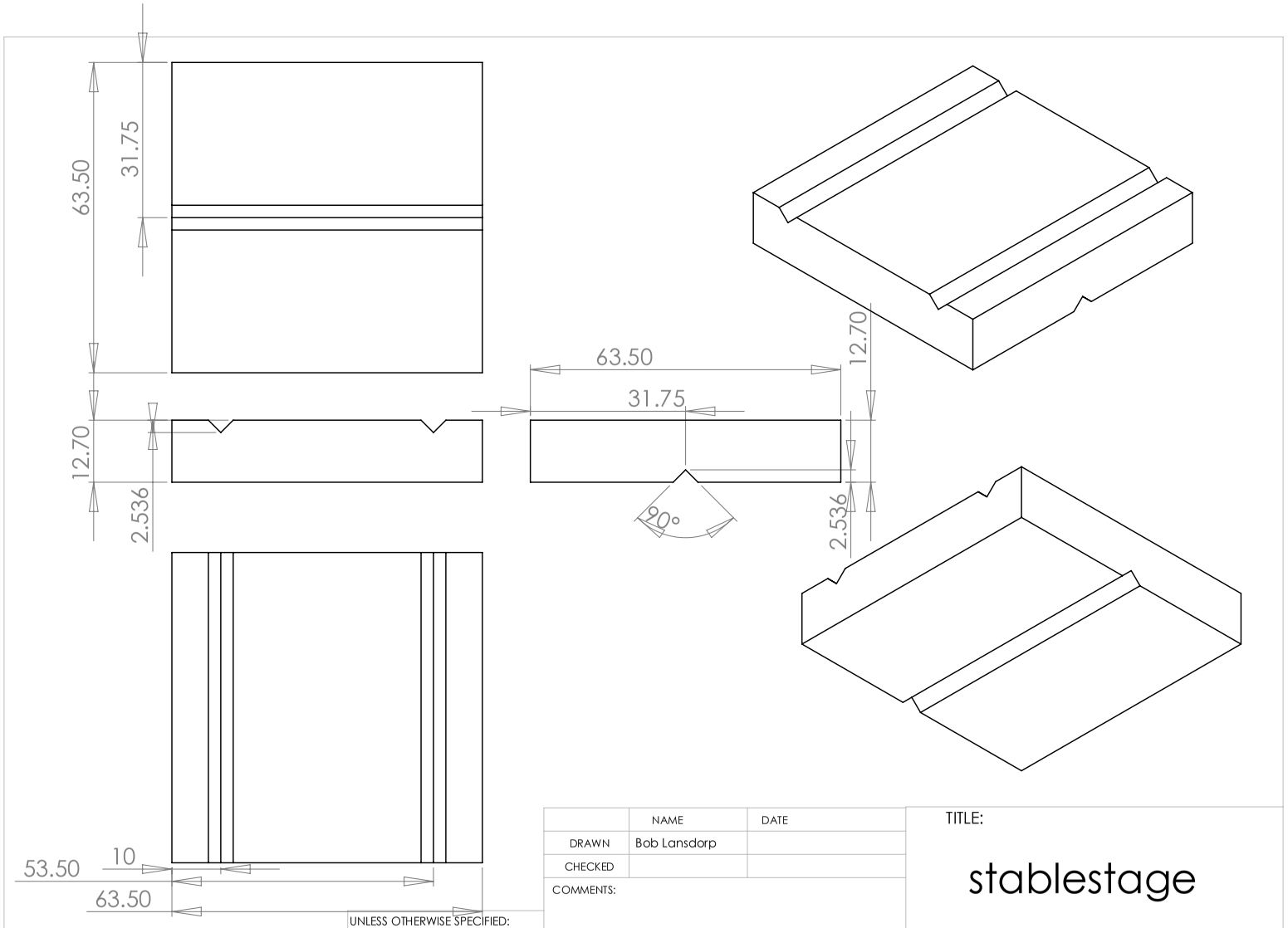

	NAME	DATE
DRAWN	Bob Lansdorp	
CHECKED		

COMMENTS:

UNLESS OTHERWISE SPECIFIED:
DIMENSIONS ARE IN MM

MATERIAL

FINISH

TITLE:

stablestage

SCALE: 1:1 | SHEET 3 OF 7

The Saleh Lab at UCSB

5 4 3 2 1

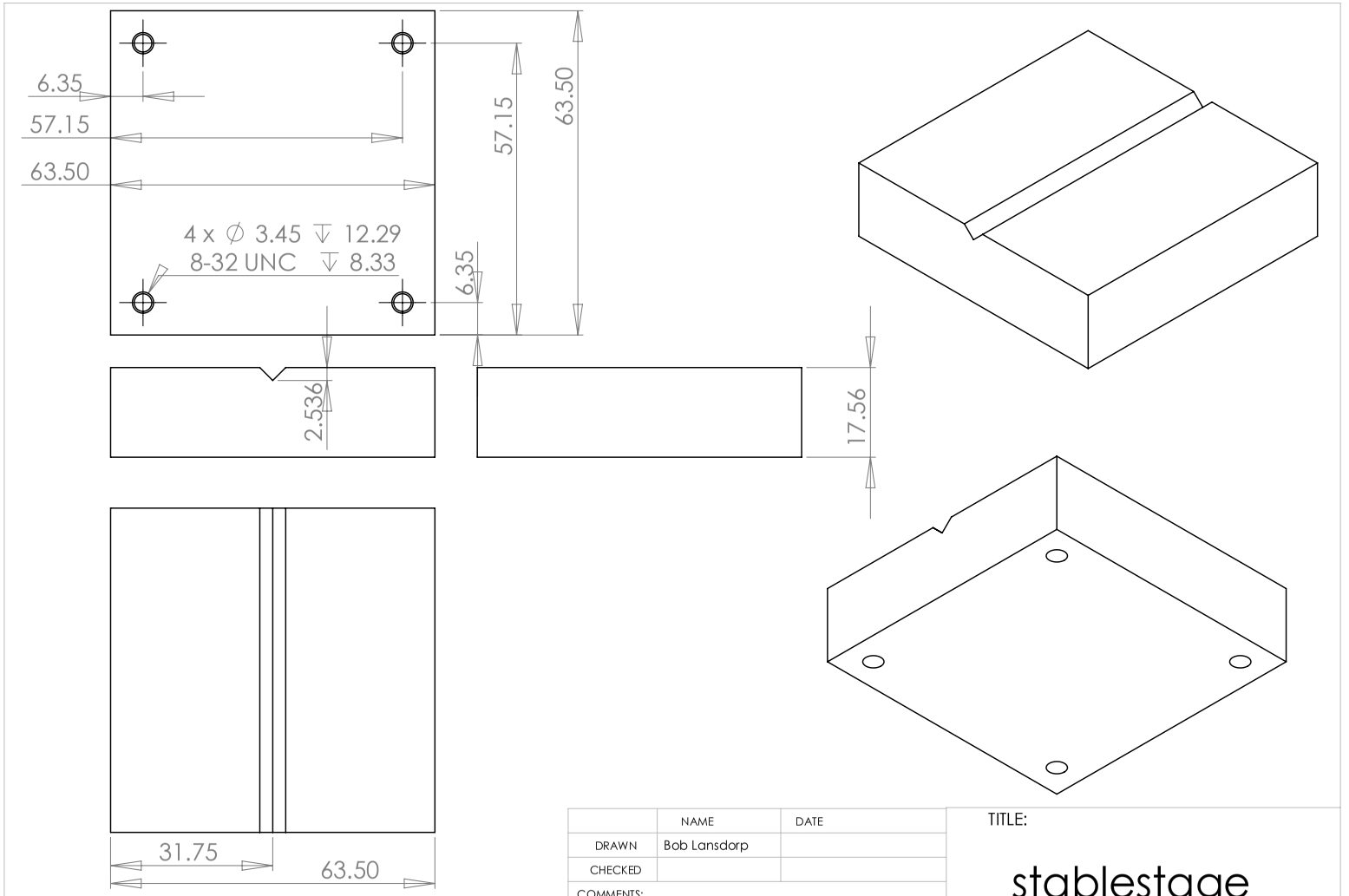

	NAME	DATE
DRAWN	Bob Lansdorp	
CHECKED		
COMMENTS:		

TITLE:

stablestage

UNLESS OTHERWISE SPECIFIED:
DIMENSIONS ARE IN MM

MATERIAL

FINISH

SCALE: 1:1 | SHEET 4 OF 7

The Saleh Lab at UCSB

5 4 3 2 1

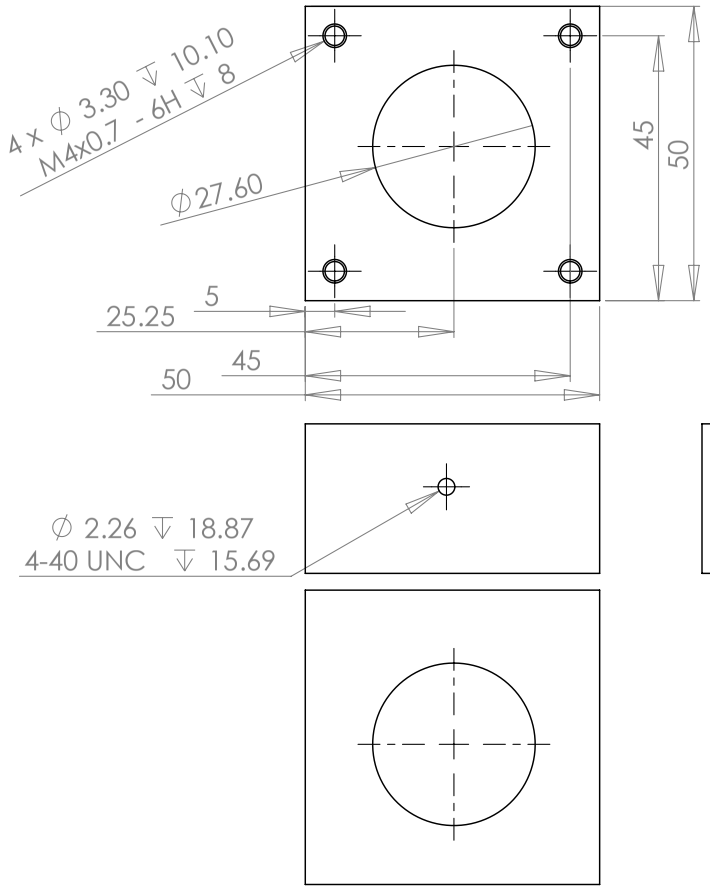

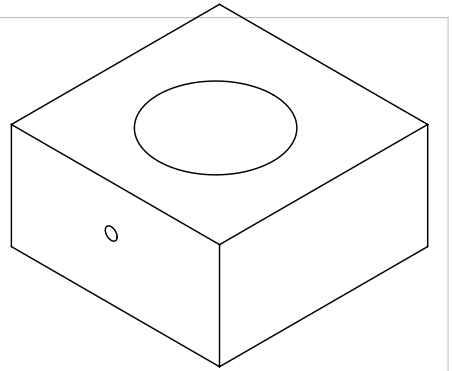

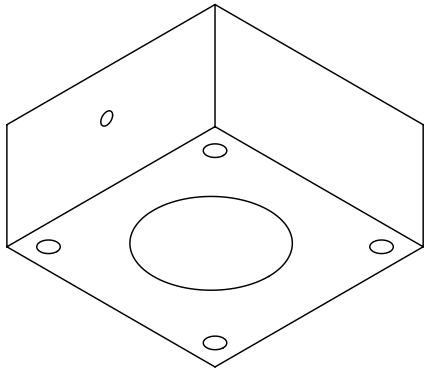

	NAME	DATE
DRAWN	Bob Lansdorp	
CHECKED		
COMMENTS:		

UNLESS OTHERWISE SPECIFIED:
DIMENSIONS ARE IN MM

MATERIAL

FINISH

TITLE:

stablestage

SCALE: 1:1 | SHEET 5 OF 7

The Saleh Lab at UCSB

5 4 3 2 1

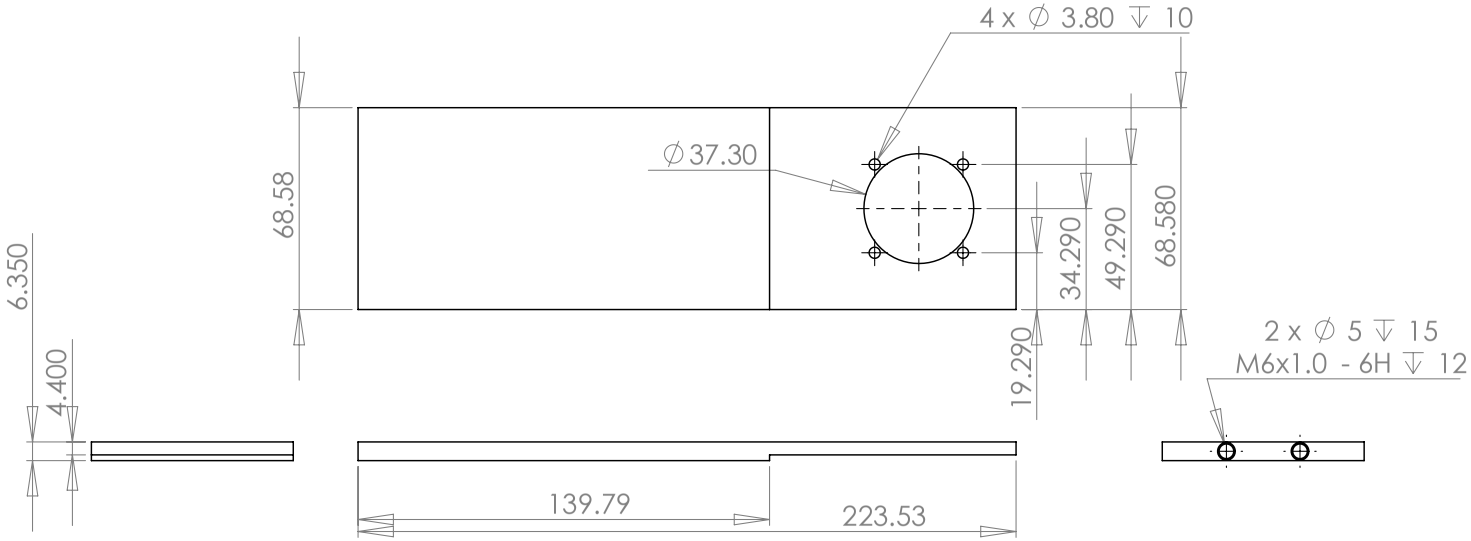

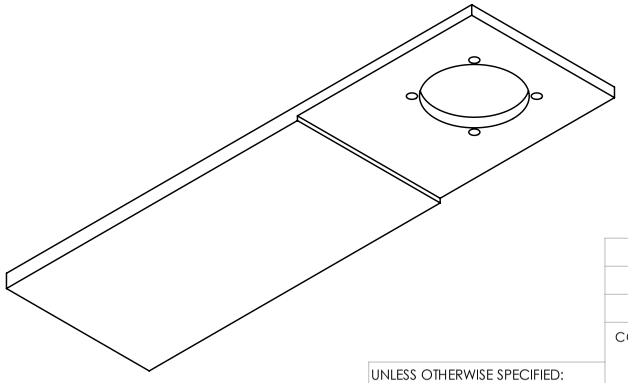

	NAME	DATE
DRAWN	Bob Lansdorp	
CHECKED		
COMMENTS:		

UNLESS OTHERWISE SPECIFIED:
DIMENSIONS ARE IN MM

MATERIAL

FINISH

TITLE:

stablestage

SCALE: 1:2 | SHEET 6 OF 7

The Saleh Lab at UCSB

5 4 3 2 1

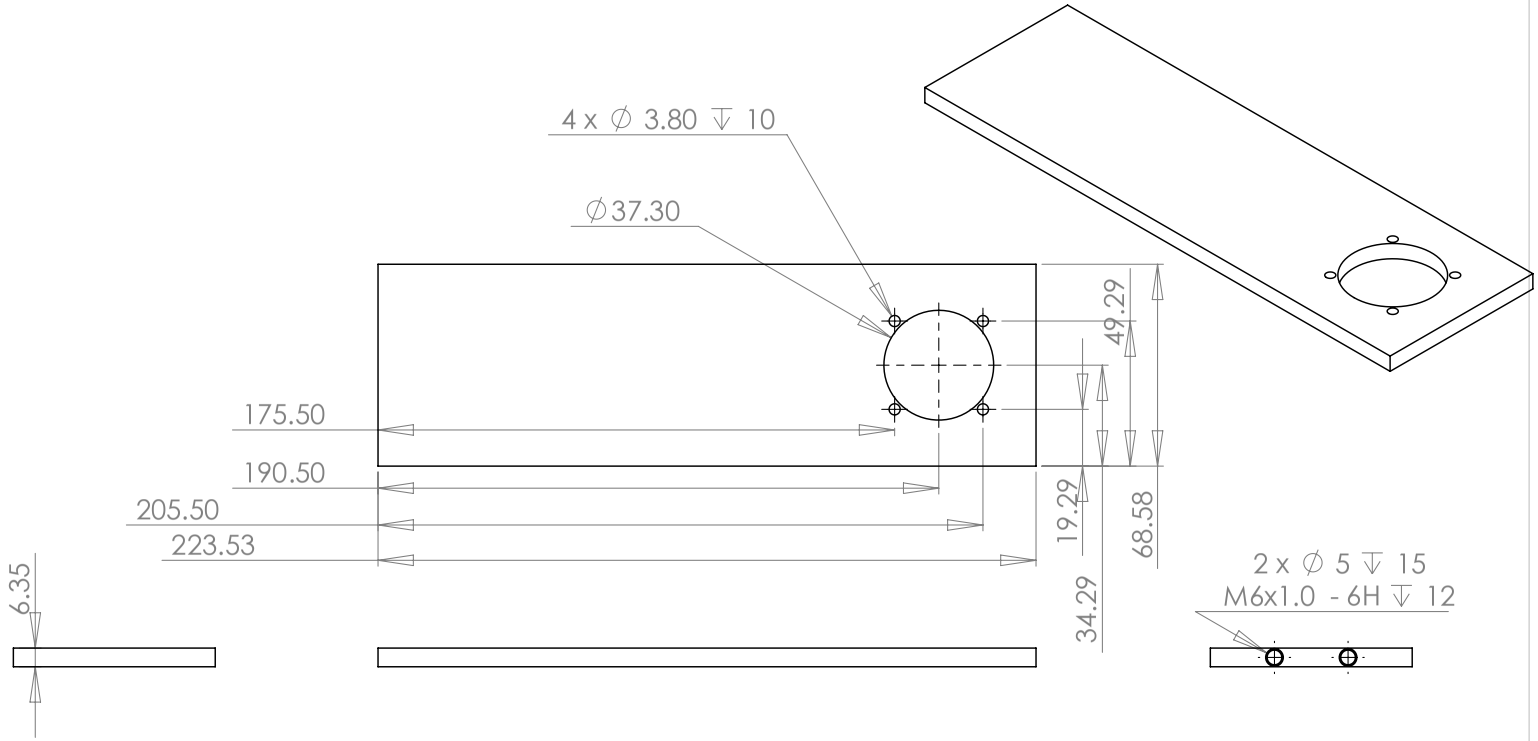

	NAME	DATE
DRAWN	Bob Lansdorp	
CHECKED		
COMMENTS:		

UNLESS OTHERWISE SPECIFIED:
DIMENSIONS ARE IN MM

MATERIAL

FINISH

TITLE:

stablestage

SCALE: 1:2 | SHEET 7 OF 7

The Saleh Lab at UCSB

5 4 3 2 1

A custom liquid cooling system

Attached are Solidworks renderings of a liquid cooling system for the Phantom v7.3 high-speed camera used in this thesis. The parts were machined at the UCSB Physics Machine Shop.

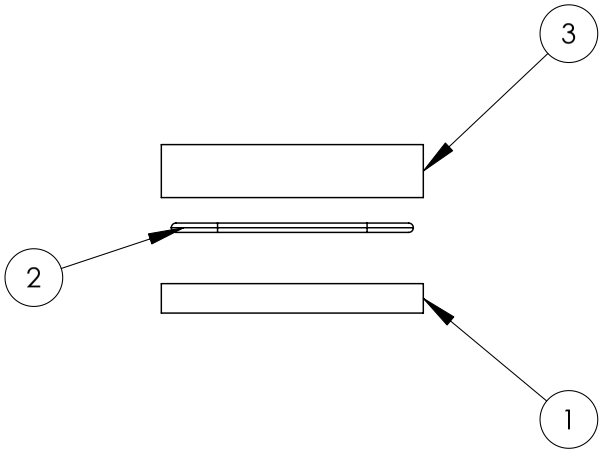

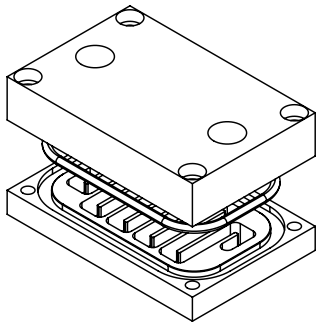

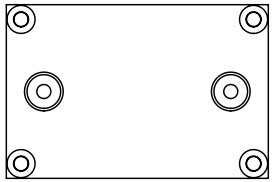

ITEM NO.	PART NUMBER	QTY.
1	cooling block	2
2	gasket	2
3	top plate	2

	NAME	DATE
DRAWN	Bob Lansdorp	March 28, 2014
CHECKED		
COMMENTS:		

UNLESS OTHERWISE SPECIFIED:
DIMENSIONS ARE IN MM

MATERIAL

FINISH

TITLE:

liquid cooling system

SCALE: 1:2 | SHEET 1 OF 3

The Saleh Lab at UCSB

5 4 3 2 1

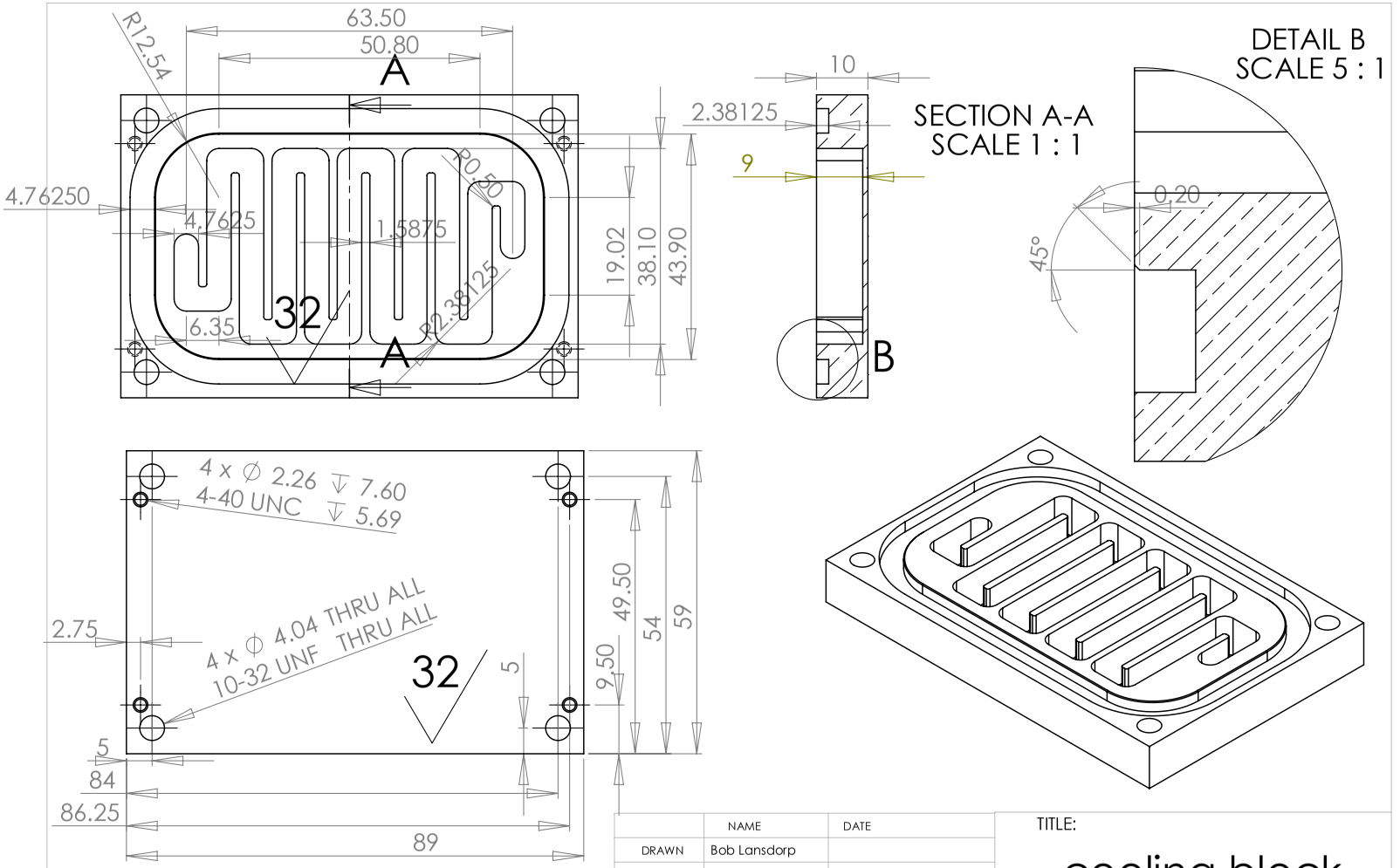

	NAME	DATE
DRAWN	Bob Lansdorp	
CHECKED		

TITLE:

cooling block

UNLESS OTHERWISE SPECIFIED:
DIMENSIONS ARE IN MM

MATERIAL	Copper
FINISH	heat-sink side: Mirror

COMMENTS:
-O-ring track to compress 1/8" O-ring to 75% of initial height (2.381mm depth)
-surface roughness less than 32 microinches to ensure good o-ring seal
-Added chamfer to o-ring gland to prevent o-ring damage during installation
-Heat-sink side also polished to 32 microinches roughness to improve contact

SCALE: 1:2 | SHEET 2 OF 3

The Saleh Lab at UCSB

5 4 3 2 1

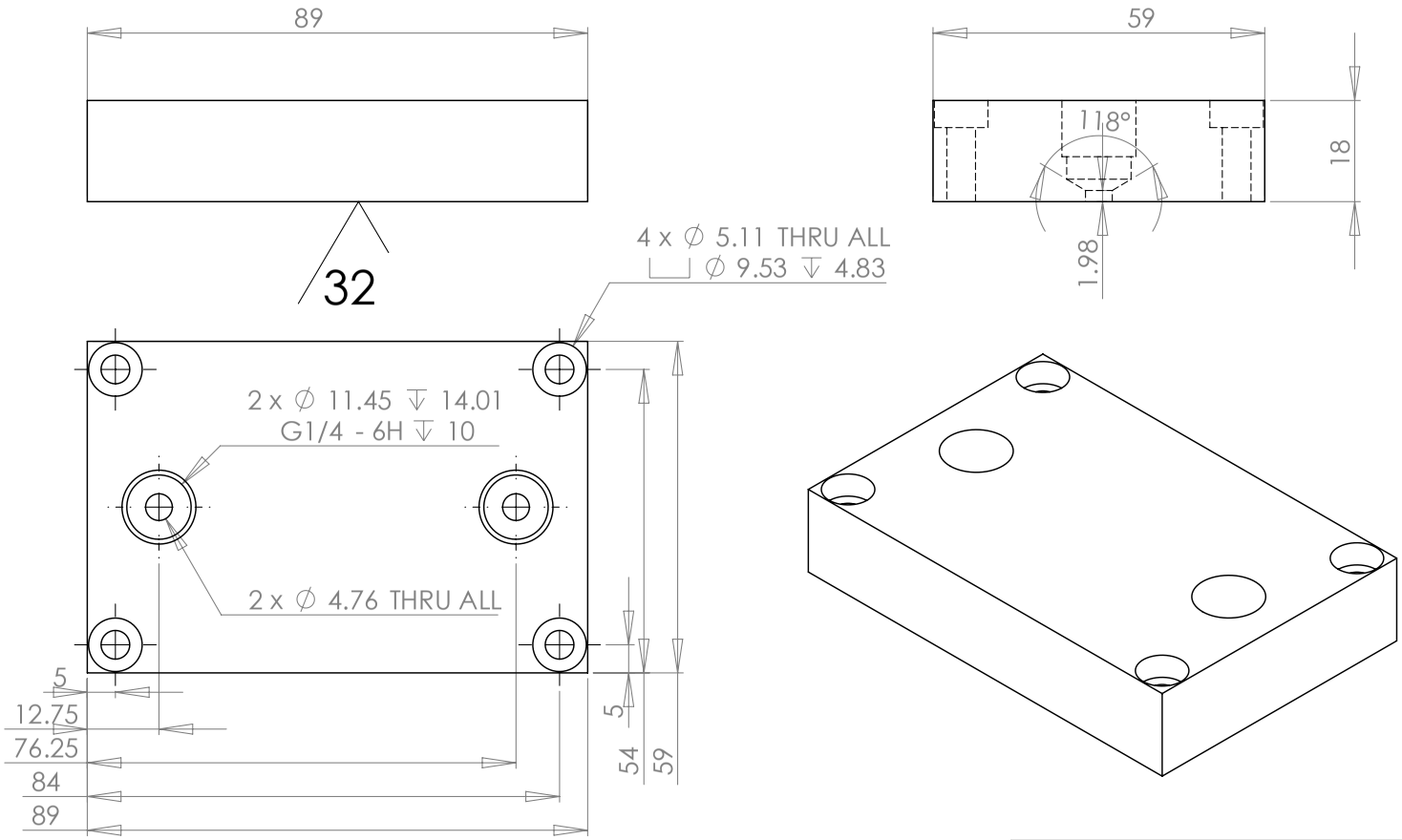

	NAME	DATE
DRAWN	Bob Lansdorp	
CHECKED		

COMMENTS:

from google search: G1/4 thread has 19TPI
this connects to liquid cooling adapter

32 microinches roughness for o-ring seal

UNLESS OTHERWISE SPECIFIED:
DIMENSIONS ARE IN MM

MATERIAL Copper

FINISH

TITLE:

top plate

SCALE: 1:2 | SHEET 3 OF 3

The Saleh Lab at UCSB

5 4 3 2 1

High gradient magnets

Attached are Solidworks drawings of high-gradient magnets.

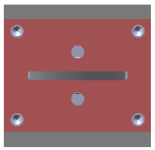

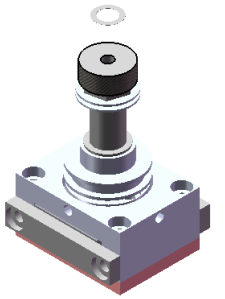

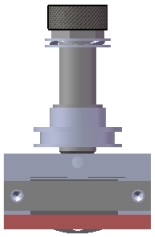

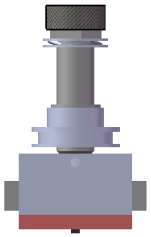

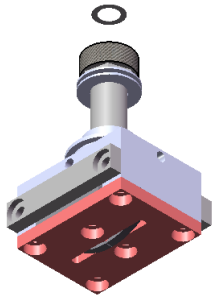

To DO: Consider length of knurl rod... with extra washer?

	NAME	DATE
DRAWN	Bob Lansdorp	June 16, 2014
CHECKED		
COMMENTS:		

UNLESS OTHERWISE SPECIFIED:
DIMENSIONS ARE IN MM

MATERIAL

FINISH

TITLE:

magnet holder

SCALE: 1:5 | SHEET 1 OF 9

The Saleh Lab at UCSB

5 4 3 2 1

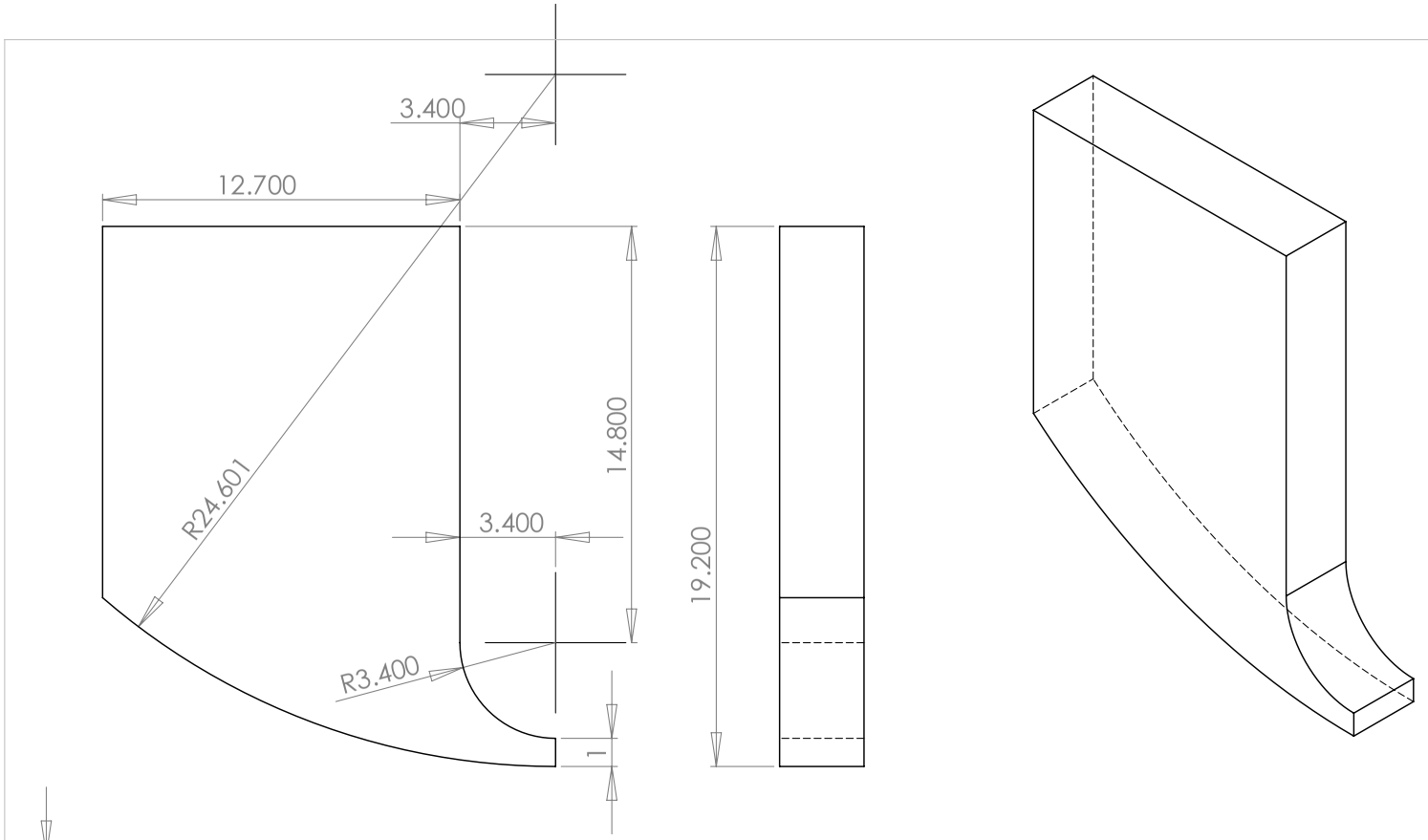

	NAME	DATE
DRAWN	Bob Lansdorp	June 16, 2014
CHECKED		
COMMENTS:		

TITLE:

magnet holder

UNLESS OTHERWISE SPECIFIED: DIMENSIONS ARE IN MM	
MATERIAL	high saturation magnetization iron
FINISH	zinc-plated (anti-corrosion)

SCALE: 5:1 | SHEET 2 OF 9

The Saleh Lab at UCSB

5 4 3 2 1

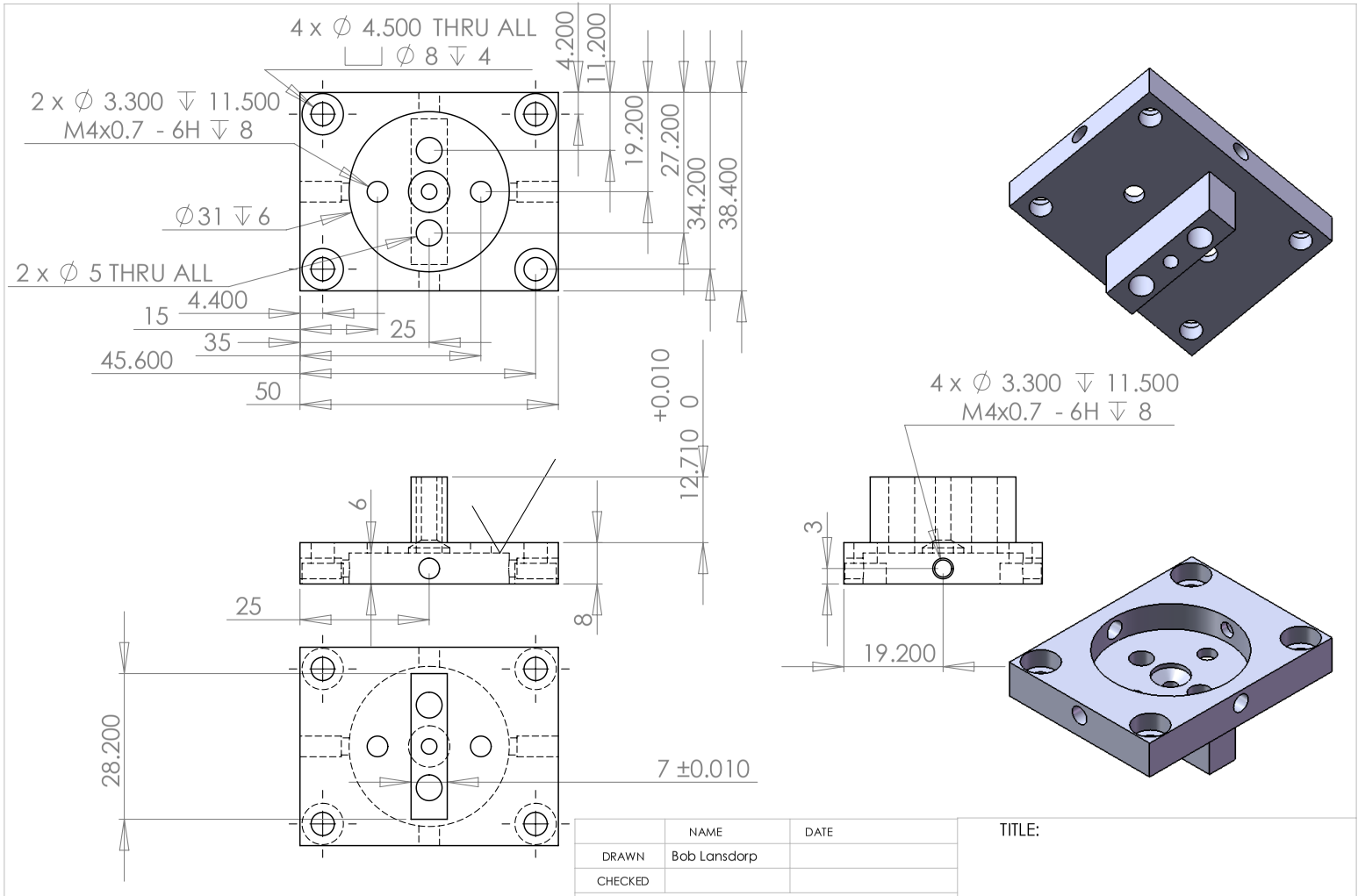

	NAME	DATE
DRAWN	Bob Lansdorp	
CHECKED		
COMMENTS:		

UNLESS OTHERWISE SPECIFIED:
DIMENSIONS ARE IN MM

MATERIAL Aluminum

FINISH

TITLE:

magnet holder

SCALE: 1:1 | SHEET 3 OF 9

The Saleh Lab at UCSB

5 4 3 2 1

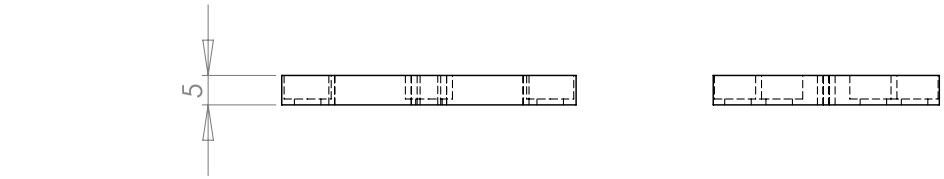

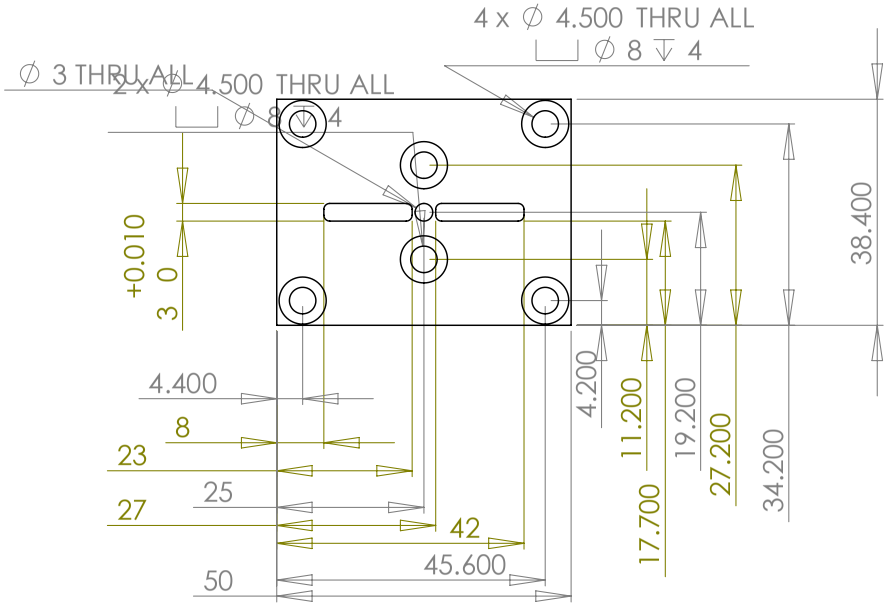

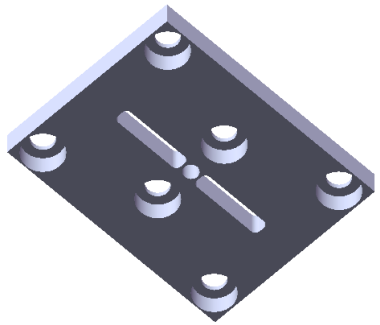

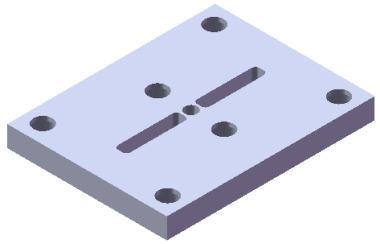

	NAME	DATE
DRAWN	Bob Lansdorp	
CHECKED		
COMMENTS:		

TITLE:

magnet holder

UNLESS OTHERWISE SPECIFIED:
DIMENSIONS ARE IN MM

MATERIAL Aluminum

FINISH

SCALE: 1:1 | SHEET 4 OF 9

The Saleh Lab at UCSB

5 4 3 2 1

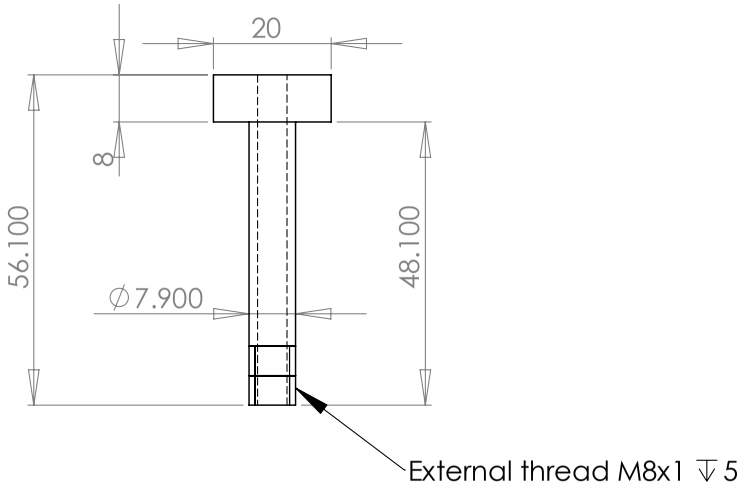

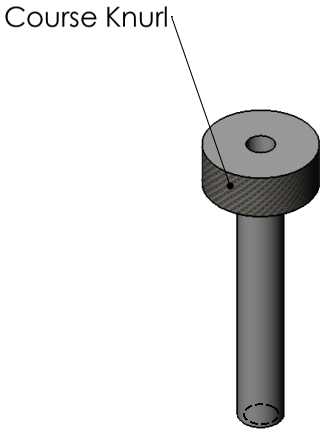

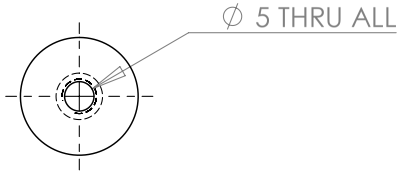

	NAME	DATE
DRAWN	Bob Lansdorp	
CHECKED		
COMMENTS:		

UNLESS OTHERWISE SPECIFIED:
DIMENSIONS ARE IN MM

MATERIAL Aluminum

FINISH

TITLE:

magnet holder

SCALE: 1:1 | SHEET 5 OF 9

The Saleh Lab at UCSB

5 4 3 2 1

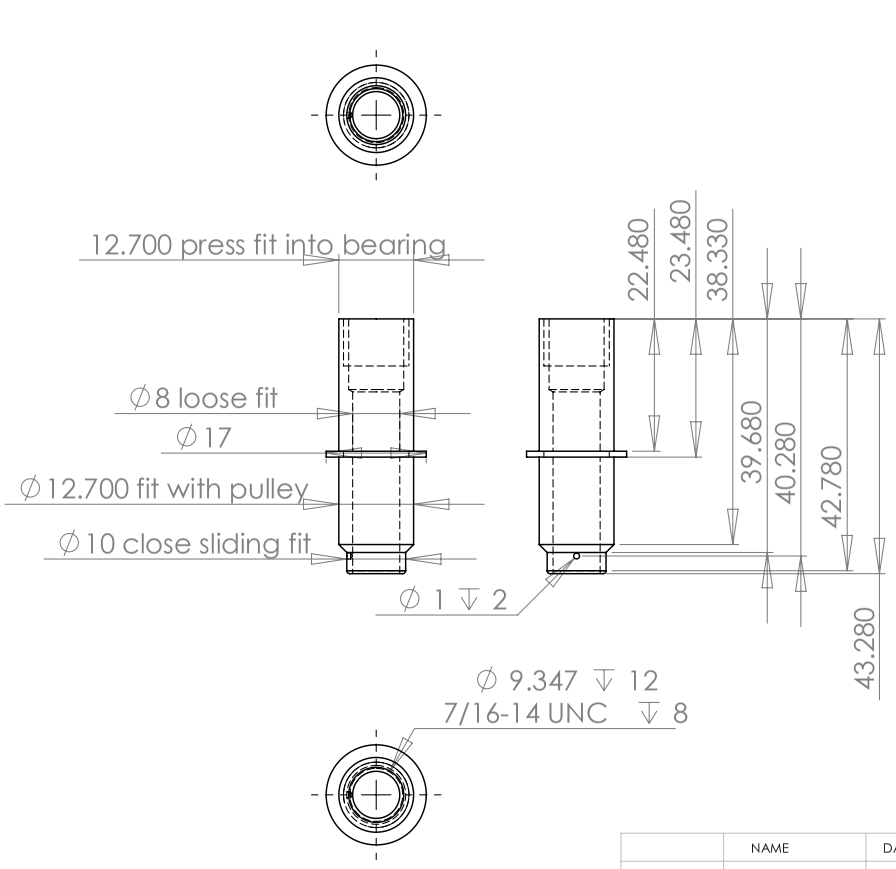

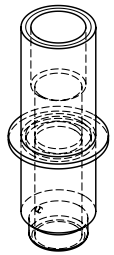

	NAME	DATE
DRAWN	Bob Lansdorp	
CHECKED		
COMMENTS:		

UNLESS OTHERWISE SPECIFIED:
DIMENSIONS ARE IN MM

MATERIAL Aluminum

FINISH

TITLE:

magnet holder

SCALE: 1:1 | SHEET 6 OF 9

The Saleh Lab at UCSB

5 4 3 2 1

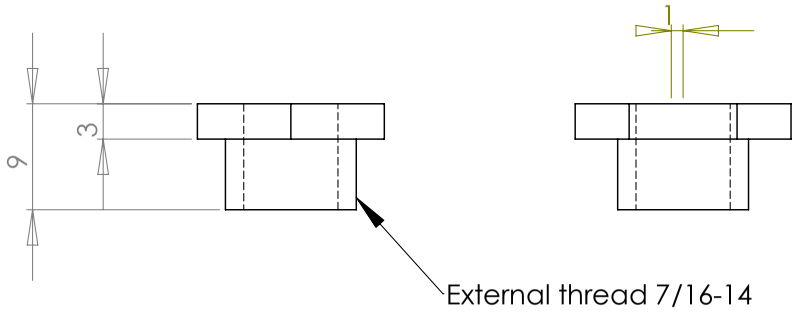

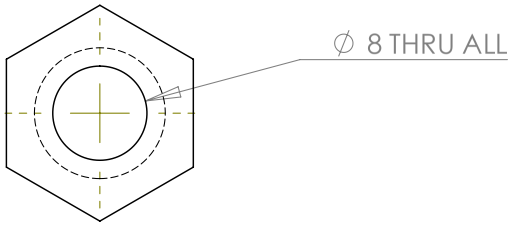

	NAME	DATE
DRAWN	Bob Lansdorp	
CHECKED		

COMMENTS:

This can be a 7/16-14 hex bolt milled down to size

UNLESS OTHERWISE SPECIFIED:
DIMENSIONS ARE IN MM

MATERIAL

FINISH

TITLE:

magnet holder

SCALE: 2:1 | SHEET 7 OF 9

The Saleh Lab at UCSB

5 4 3 2 1

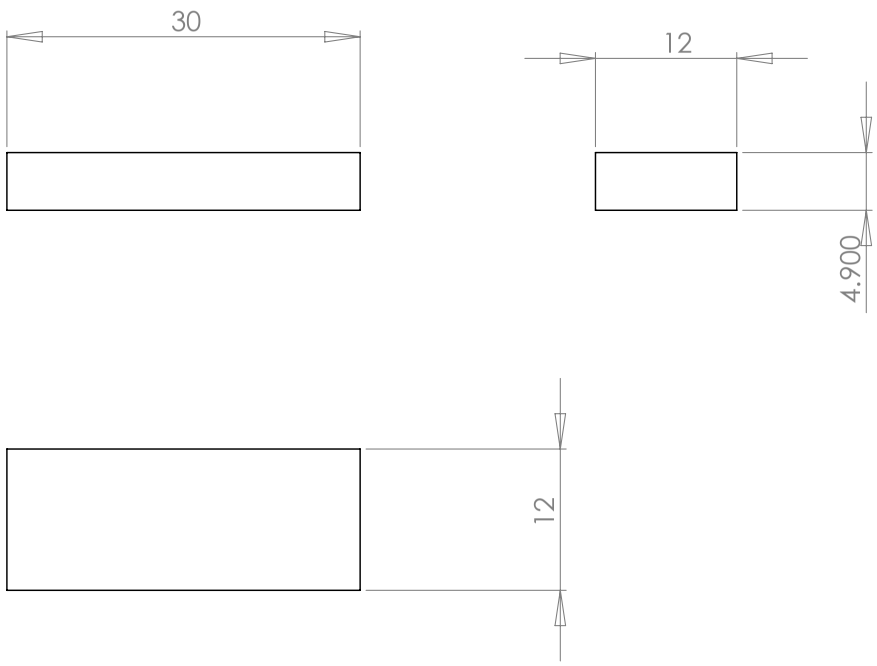

	NAME	DATE
DRAWN	Bob Lansdorp	
CHECKED		
COMMENTS:		

UNLESS OTHERWISE SPECIFIED:
DIMENSIONS ARE IN MM

MATERIAL High magnetic permeability Iron

FINISH

TITLE:

magnet holder

SCALE: 2:1 | SHEET 8 OF 9

The Saleh Lab at UCSB

5 4 3 2 1

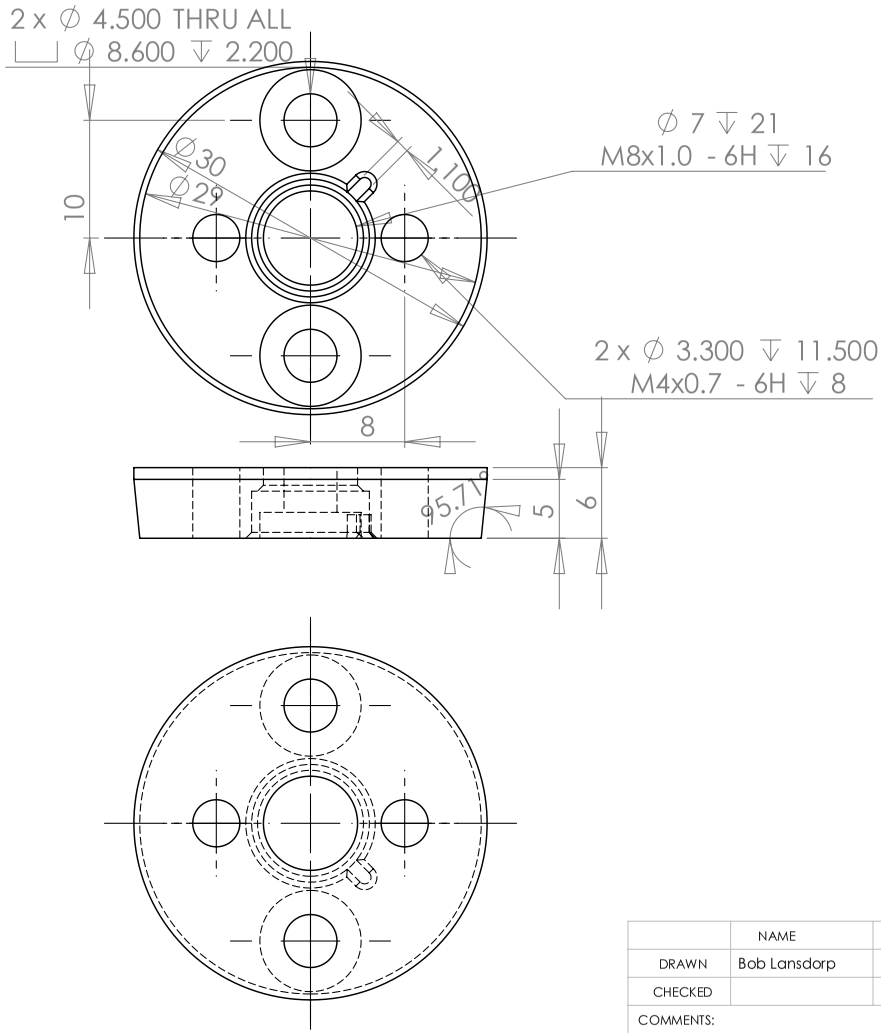

	NAME	DATE
DRAWN	Bob Lansdorp	
CHECKED		
COMMENTS:		

UNLESS OTHERWISE SPECIFIED:
DIMENSIONS ARE IN MM

MATERIAL

FINISH

TITLE:

magnet holder

SCALE: 2:1 | SHEET 9 OF 9

The Saleh Lab at UCSB

5 4 3 2 1

Pt spatial filter mask

Attached is a drawings of shadow mask, which is used in the manufacture a Pt spatial filter.

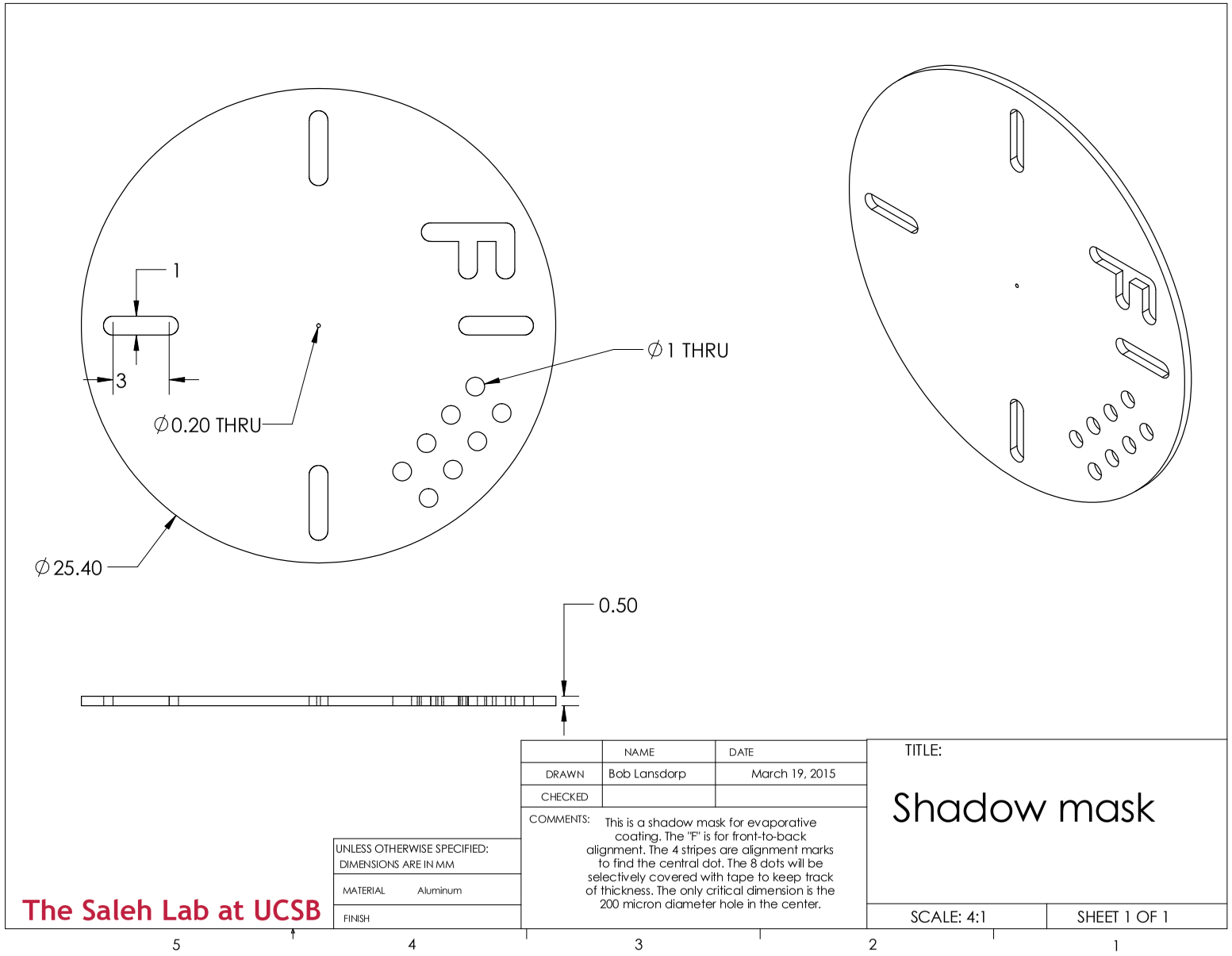
1
3
∅0.20 THRU
∅1 THRU
∅25.40
0.50
F
F
UNLESS OTHERWISE SPECIFIED:
DIMENSIONS ARE IN MM
MATERIAL Aluminum
FINISH
NAME
DATE
DRAWN
Bob Lansdorp
March 19, 2015
CHECKED
COMMENTS:
This is a shadow mask for evaporative coating. The "F" is for front-to-back alignment. The 4 stripes are alignment marks to find the central dot. The 8 dots will be selectively covered with tape to keep track of thickness. The only critical dimension is the 200 micron diameter hole in the center.
TITLE:
Shadow mask
SCALE: 4:1
SHEET 1 OF 1
The Saleh Lab at UCSB
5
4
3
2
1

Bibliography

[1] W. J. Greenleaf, M. T. Woodside, and S. M. Block, "High-resolution, single-molecule measurements of biomolecular motion," *Annu. Rev. Biophys. Biomol. Struct.*, vol. 36, p. 171, 2007.

[2] K. C. Neuman and A. Nagy, "Single-molecule force spectroscopy: optical tweezers, magnetic tweezers and atomic force microscopy," *Nature methods*, vol. 5, no. 6, pp. 491–505, 2008.

[3] I. De Vlaminck and C. Dekker, "Recent advances in magnetic tweezers," *Annual Review of Biophysics*, no. 0, 2012.

[4] Y. R. Chemla, "Revealing the base pair stepping dynamics of nucleic acid motor proteins with optical traps," *Phys. Chem. Chem. Phys.*, vol. 12, no. 13, pp. 3080–3095, 2010.

[5] E. A. Abbondanzieri, W. J. Greenleaf, J. W. Shaevitz, R. Landick, and S. M. Block, "Direct observation of base-pair stepping by rna polymerase," *Nature*, vol. 438, no. 7067, pp. 460–465, 2005.

[6] A. R. Carter, Y. Seol, and T. T. Perkins, "Precision surface-coupled optical-trapping assay with one-basepair resolution," *Biophysical Journal*, vol. 96, no. 7, pp. 2926–2934, 2009.

[7] M. Mahamdeh, E. Schäffer, *et al.*, "Optical tweezers with millikelvin precision of temperature-controlled objectives and base-pair resolution," *Optics Express*, vol. 17, no. 19, pp. 17190–17199, 2009.

[8] W. Cheng, S. G. Arunajadai, J. R. Moffitt, I. Tinoco Jr, and C. Bustamante, "Single–base pair unwinding and asynchronous rna release by the hepatitis c virus ns3 helicase," *Science*, vol. 333, no. 6050, pp. 1746–1749, 2011.

[9] R. Walder, D. H. Paik, M. S. Bull, C. Sauer, and T. T. Perkins, "Ultrastable measurement platform: sub-nm drift over hours in 3d at room temperature," *Opt. Express*, vol. 23, pp. 16554–16564, Jun 2015.

[10] N. Ribeck and O. Saleh, "Multiplexed single-molecule measurements with magnetic tweezers," *Review of Scientific Instruments*, vol. 79, p. 094301, 2008.

[11] N. Ribeck, D. L. Kaplan, I. Bruck, and O. A. Saleh, "Dnab helicase activity is modulated by dna geometry and force," *Biophysical journal*, vol. 99, no. 7, pp. 2170–2179, 2010.

[12] M. T. Woodside, W. M. Behnke-Parks, K. Larizadeh, K. Travers, D. Herschlag, and S. M. Block, "Nanomechanical measurements of the sequence-dependent folding landscapes of single nucleic acid hairpins," *Proc. Natl. Acad. Sci. USA*, vol. 103, no. 16, pp. 6190–6195, 2006.

[13] W. J. Greenleaf, M. T. Woodside, E. A. Abbondanzieri, and S. M. Block, "Passive all-optical force clamp for high-resolution laser trapping," *Physical Review Letters*, vol. 95, no. 20, p. 208102, 2005.

[14] J. R. Moffitt, Y. R. Chemla, S. B. Smith, and C. Bustamante, "Recent advances in optical tweezers," *Annu. Rev. Biochem.*, vol. 77, pp. 205–228, 2008.

[15] Y.-F. Chen, G. A. Blab, and J.-C. Meiners, "Stretching submicron biomolecules with constant-force axial optical tweezers," *Biophysical journal*, vol. 96, no. 11, pp. 4701–4708, 2009.

[16] M. J. Lang, C. L. Asbury, J. W. Shaevitz, and S. M. Block, "An automated two-dimensional optical force clamp for single molecule studies," *Biophysical Journal*, vol. 83, no. 1, pp. 491 – 501, 2002.

[17] K. Kim and O. A. Saleh, "A high-resolution magnetic tweezer for single-molecule measurements," *Nucleic acids research*, vol. 37, no. 20, pp. e136–e136, 2009.

[18] W. P. Wong and K. Halvorsen, "Beyond the frame rate: measuring high-frequency fluctuations with light-intensity modulation," *Opt. Lett.*, vol. 34, pp. 277–279, Feb 2009.

[19] O. Otto, F. Czerwinski, J. Gornall, G. Stober, L. Oddershede, R. Seidel, and U. Keyser, "Real-time particle tracking at 10,000 fps using optical fiber illumination," *Optics Express*, vol. 18, no. 22, pp. 22722–22733, 2010.

[20] D. Dulin, S. Barland, X. Hachair, and F. Pedaci, "Efficient illumination for microsecond tracking microscopy," *PLoS ONE*, vol. 9, p. e107335, 09 2014.

[21] F. Czerwinski, A. C. Richardson, and L. B. Oddershede, "Quantifying noise in optical tweezers by allan variance," *Opt. Express*, vol. 17, pp. 13255–13269, Jul 2009.

[22] G. M. Gibson, J. Leach, S. Keen, A. J. Wright, and M. J. Padgett, "Measuring the accuracy of particleposition and force in optical tweezersusing high-speed video microscopy," *Opt. Express*, vol. 16, pp. 14561–14570, Sep 2008.

[23] O. Otto, J. L. Gornall, G. Stober, F. Czerwinski, R. Seidel, and U. F. Keyser, "High-speed video-based tracking of optically trapped colloids," *Journal of Optics*, vol. 13, p. 044011, 2011.

[24] G. M. Gibson, R. W. Bowman, A. Linnenberger, M. Dienerowitz, D. B. Phillips, D. M. Carberry, M. J. Miles, and M. J. Padgett, "A compact holographic optical tweezers instrument," *Review of Scientific Instruments*, vol. 83, no. 11, pp. 113107–113107, 2012.

[25] S.-H. Lee, Y. Roichman, G.-R. Yi, S.-H. Kim, S.-M. Yang, A. van Blaaderen, P. van Oostrum, and D. G. Grier, "Characterizing and tracking single colloidal particles with video holographic microscopy," *Optics Express*, vol. 15, no. 26, pp. 18275–18282, 2007.

[26] M. T. J. van Loenhout, J. W. J. Kerssemakers, I. De Vlaminck, and C. Dekker, "Non-bias-limited tracking of spherical particles, enabling nanometer resolution at low magnification," *Biophysical Journal*, vol. 102, no. 10, pp. 2362–2371, 2012.

[27] J. C. Crocker and D. G. Grier, "Methods of digital video microscopy for colloidal studies," *Journal of Colloid and Interface Science*, vol. 179, no. 1, pp. 298 – 310, 1996.

[28] S. J. Tabrizi, "Identifying the limits of magnetic tweezers tracking error," bachelor thesis, University of California, Santa Barbara, June 2014.

[29] S. Prahl, "Mie scattering calculator." http://omlc.org/calc/mie_calc.html, June 2012.

[30] P. Lebel, A. Basu, F. C. Oberstrass, E. M. Tretter, and Z. Bryant, "Gold rotor bead tracking for high-speed measurements of dna twist, torque and extension," *Nature methods*, vol. 11, no. 4, pp. 456–462, 2014.

[31] A. J. Cox, A. J. DeWeerd, and J. Linden, "An experiment to measure mie and rayleigh total scattering cross sections," *American Journal of Physics*, vol. 70, no. 6, pp. 620–625, 2002.

[32] W. A. Edelstein, J. Hough, J. R. Pugh, and W. Martin, "Limits to the measurement of displacement in an interferometric gravitational radiation detector," *Journal of Physics E: Scientific Instruments*, vol. 11, no. 7, p. 710, 1978.

[33] R. P. Feynman, "There's plenty of room at the bottom," *Engineering and science*, vol. 23, no. 5, pp. 22–36, 1960.

[34] M. vanLoenhout, J. W. Kerssemakers, I. DeVlaminck, and C. Dekker, "Non-bias-limited tracking of spherical particles, enabling nanometer resolution at low magnification," *Biophysical Journal*, vol. 102, no. 10, pp. 2362 – 2371, 2012.

[35] B. M. Lansdorp and O. A. Saleh, "Power spectrum and allan variance methods for calibrating single-molecule video-tracking instruments," *Review of Scientific Instruments*, vol. 83, no. 2, pp. 025115–025115, 2012.

[36] D. Klaue and R. Seidel, "Torsional stiffness of single superparamagnetic microspheres in an external magnetic field," *Physical review letters*, vol. 102, no. 2, p. 28302, 2009.

[37] M. M. van Oene, L. E. Dickinson, F. Pedaci, M. Köber, D. Dulin, J. Lipfert, and N. H. Dekker, "Biological magnetometry: Torque on superparamagnetic beads in magnetic fields," *Physical Review Letters*, vol. 114, no. 21, p. 218301, 2015.

[38] P. Daldrop, H. Brutzer, A. Huhle, D. Kauert, and R. Seidel, "Extending the range for force calibration in magnetic tweezers," *Biophysical Journal*, vol. 108, no. 10, pp. 2550 – 2561, 2015.

[39] J. Lipfert, J. J. Kerssemakers, M. Rojer, and N. H. Dekker, "A method to track rotational motion for use in single-molecule biophysics," *Review of Scientific Instruments*, vol. 82, no. 10, p. 103707, 2011.

[40] P. Langevin, "Sur la théorie du mouvement brownien," *CR Acad. Sci. Paris*, vol. 146, no. 530-533, 1908.

[41] R. Huang, I. Chavez, K. M. Taute, B. Lukić, S. Jeney, M. G. Raizen, and E.-L. Florin, "Direct observation of the full transition from ballistic to diffusive brownian motion in a liquid," *Nature Physics*, vol. 7, no. 7, pp. 576–580, 2011.

[42] B. Lukić, S. Jeney, C. Tischer, A. J. Kulik, L. Forró, and E.-L. Florin, "Direct observation of nondiffusive motion of a brownian particle," *Phys. Rev. Lett.*, vol. 95, p. 160601, Oct 2005.

[43] W. P. Wong and K. Halvorsen, "The effect of integration time on fluctuation measurements: calibrating an optical trap in the presence of motion blur," *Opt. Express*, vol. 14, pp. 12517–12531, Dec 2006.

[44] F. Harris, "On the use of windows for harmonic analysis with the discrete fourier transform," *Proceedings of the IEEE*, vol. 66, no. 1, pp. 51–83, 1978.

[45] P. Welch, "The use of fast fourier transform for the estimation of power spectra: a method based on time averaging over short, modified periodograms," *Audio and Electroacoustics, IEEE Transactions on*, vol. 15, no. 2, pp. 70–73, 1967.

[46] S. F. Nørrelykke and H. Flyvbjerg, "Power spectrum analysis with least-squares fitting: Amplitude bias and its elimination, with application to optical tweezers and atomic force microscope cantilevers," *Review of Scientific Instruments*, vol. 81, no. 7, p. 075103, 2010.

[47] A. Te Velthuis, J. Kerssemakers, J. Lipfert, and N. Dekker, "Quantitative guidelines for force calibration through spectral analysis of magnetic tweezers data," *Biophysical journal*, vol. 99, no. 4, pp. 1292–1302, 2010.

[48] K. Berg-Sørensen and H. Flyvbjerg, "Power spectrum analysis for optical tweezers," *Review of Scientific Instruments*, vol. 75, no. 3, pp. 594–612, 2004.

[49] N. van Kampen, *Stochastic processes in physics and chemistry*. North Holland, 2007.

[50] R. Castberg, *Characterisation and calibration of Optical tweezers*. PhD thesis, University of Oslo, 2008.

[51] J. Von Neumann, "Distribution of the ratio of the mean square successive difference to the variance," *The Annals of Mathematical Statistics*, vol. 12, no. 4, pp. 367–395, 1941.

[52] J. A. Barnes, A. R. Chi, L. S. Cutler, D. J. Healey, D. B. Leeson, T. E. McGunigal, J. A. Mullen, W. L. Smith, R. L. Sydnor, R. F. C. Vessot, and G. M. R. Winkler, "Characterization of frequency stability," *Instrumentation and Measurement, IEEE Transactions on*, vol. IM-20, pp. 105 –120, may 1971.

[53] T. Walter, "A multi-variance analysis in the time domain," in *24th Annual Precise Time and Time Interval (PTTI) Applications and Planning Meeting*, vol. 1, pp. 413–426, 1993.

[54] M. Andersson, F. Czerwinski, and L. B. Oddershede, "Optimizing active and passive calibration of optical tweezers," *Journal of Optics*, vol. 13, no. 4, p. 044020, 2011.

[55] G. Gibson, J. Leach, S. Keen, A. Wright, and M. Padgett, "Measuring the accuracy of particle position and force in optical tweezers using high-speed video microscopy," *Optics express*, vol. 16, no. 19, pp. 14561–14570, 2008.

[56] C. Gosse and V. Croquette, "Magnetic tweezers: Micromanipulation and force measurement at the molecular level," *Biophysical Journal*, vol. 82, no. 6, pp. 3314 – 3329, 2002.

[57] D. Allan, "Statistics of atomic frequency standards," *Proceedings of the IEEE*, vol. 54, no. 2, pp. 221–230, 1966.

[58] W. Riley, *Handbook of Frequency Stability Analysis*. Hamilton Technical Services, 2007.

[59] P. Lesage and C. Audoin, "Effect of dead-time on the estimation of the two-sample variance," *Instrumentation and Measurement, IEEE Transactions on*, vol. 28, no. 1, pp. 6–10, 1979.

[60] J. Barnes, "Variances based on data with dead time between the measurements," in *19th Annual Precise Time and Time Interval (PTTI) Applications and Planning Meeting*, pp. 227–234, 1987.

[61] C. M. V. Vliet and P. H. Handel, "A new transform theorem for stochastic processes with special application to counting statistics," *Physica A: Statistical Mechanics and its Applications*, vol. 113, no. 12, pp. 261 – 276, 1982.

[62] D. Howe, D. Allan, and J. Barnes, "Properties of signal sources and measurement methods," in *Annual Frequency Control Symposium, 35 th, Philadelphia, PA*, 1981.

[63] T. Walter, "Characterizing frequency stability: a continuous power-law model with discrete sampling," *Instrumentation and Measurement, IEEE Transactions on*, vol. 43, pp. 69 –79, feb 1994.

[64] B. M. Lansdorp and O. A. Saleh, "Erratum:power spectrum and allan variance methods for calibrating single-molecule video-tracking instruments[rev. sci. instrum. 83, 025115 (2012)]," *The Review of scientific instruments*, vol. 85, no. 1, 2014.

[65] D. Allan, M. Weiss, and J. Jespersen, "A frequency-domain view of time-domain characterization of clocks and time and frequency distribution systems," in *Proceedings of the 45th Annual Symposium on Frequency Control*, pp. 667–678, IEEE, 1991.

[66] A. Makdissi, F. Vernotte, and E. Clercq, "Stability variances: a filter approach," *Ultrasonics, Ferroelectrics and Frequency Control, IEEE Transactions on*, vol. 57, pp. 1011 –1028, may 2010.

[67] E. Schäffer, S. Nørrelykke, and J. Howard, "Surface forces and drag coefficients of microspheres near a plane surface measured with optical tweezers," *Langmuir*, vol. 23, no. 7, pp. 3654–3665, 2007.

[68] C. Bouchiat, M. Wang, J. Allemand, T. Strick, S. Block, and V. Croquette, "Estimating the persistence length of a worm-like chain molecule from force-extension measurements," *Biophysical journal*, vol. 76, no. 1, pp. 409–413, 1999.

[69] B. M. Lansdorp, S. J. Tabrizi, A. Dittmore, and O. A. Saleh, "A high-speed magnetic tweezer beyond 10,000 frames per second," *Review of Scientific Instruments*, vol. 84, no. 4, pp. –, 2013.

[70] O. Svelto and D. C. Hanna, *Principles of lasers*. Springer, 1976.

[71] J. Lin and M. T. Valentine, "High-force ndfeb-based magnetic tweezers device optimized for microrheology experiments," *Review of Scientific Instruments*, vol. 83, no. 5, pp. 053905–053905, 2012.

[72] J. Sanders and E. Kandrot, *CUDA by example: an introduction to general-purpose GPU programming*. Addison-Wesley Professional, 2010.

[73] J. Gal, R. Schnell, S. Szekeres, and M. Kalman, "Directional cloning of native pcr products with preformed sticky ends (autosticky pcr)," *Molecular and General Genetics MGG*, vol. 260, no. 6, pp. 569–573, 1999.

[74] H. Gumpp, S. Stahl, M. Strackharn, E. Puchner, and H. Gaub, "Ultrastable combined atomic force and total internal fluorescence microscope," *Review of scientific instruments*, vol. 80, no. 6, p. 063704, 2009.

[75] K. Goto and Y. Hayasaki, "Three-dimensional motion detection of a 20-nm gold nanoparticle using twilight-field digital holography with coherence regulation," *Opt. Lett.*, vol. 40, pp. 3344–3347, Jul 2015.

[76] N. Ribeck, *Single-molecule Measurements of the Helicase DnaB with Magnetic Tweezers*. University of California, Santa Barbara, 2011.

[77] S. S. Shevkoplyas, A. C. Siegel, R. M. Westervelt, M. G. Prentiss, and G. M. Whitesides, "The force acting on a superparamagnetic bead due to an applied magnetic field," *Lab Chip*, vol. 7, pp. 1294–1302, 2007.

[78] A. Bijamov, F. Shubitidze, P. M. Oliver, and D. V. Vezenov, "Quantitative modeling of forces in electromagnetic tweezers," *Journal of applied physics*, vol. 108, no. 10, p. 104701, 2010.

[79] T. Fallesen, D. B. Hill, M. Steen, J. C. Macosko, K. Bonin, and G. Holzwarth, "Magnet polepiece design for uniform magnetic force on

superparamagnetic beads," *Review of scientific instruments*, vol. 81, no. 7, p. 074303, 2010.

[80] J. Lipfert, X. Hao, and N. H. Dekker, "Quantitative modeling and optimization of magnetic tweezers," *Biophysical journal*, vol. 96, no. 12, pp. 5040–5049, 2009.

[81] D. E. Humphries, S.-C. Hong, M. J. Pollard, *et al.*, "Hybrid magnet devices for molecule manipulation and small scale high gradient-field applications," Jan. 6 2009. US Patent 7,474,184.

[82] N. A. Zacchia and M. T. Valentine, "Design and optimization of arrays of neodymium iron boron-based magnets for magnetic tweezers applications," *Review of Scientific Instruments*, vol. 86, no. 5, p. 053704, 2015.

[83] W. Brown, "Magnetic materials, ch 8 in the handbook of chemistry and physics, condon and odishaw, eds," 1958.

[84] C.-Y. Park and O. A. Saleh, "Image-based synchronization of force and bead motion in active electromagnetic microrheometry," *Measurement Science and Technology*, vol. 25, no. 12, p. 125010, 2014.

[85] M. R. Jolly, J. D. Carlson, and B. C. Muoz, "A model of the behaviour of magnetorheological materials," *Smart Materials and Structures*, vol. 5, no. 5, p. 607, 1996.

[86] B. Redding, P. Ahmadi, V. Mokan, M. Seifert, M. A. Choma, and H. Cao, "Low-spatial-coherence high-radiance broadband fiber source for speckle free imaging," *Opt. Lett.*, vol. 40, pp. 4607–4610, Oct 2015.

[87] J. W. Goodman, *Speckle phenomena in optics: theory and applications*. Roberts and Company Publishers, 2007.

[88] R. Dändliker, "Concept of modes in optics and photonics," in *Education and Training in Optics and Photonics (ETOP'99)*, pp. 193–198, International Society for Optics and Photonics, 2000.

[89] A. Huhle, D. Klaue, H. Brutzer, P. Daldrop, S. Joo, O. Otto, U. F. Keyser, and R. Seidel, "Camera-based three-dimensional real-time particle tracking at khz rates and ångström accuracy," *Nature communications*, vol. 6, 2015.

[90] D. Dulin, T. J. Cui, J. Cnossen, M. W. Docter, J. Lipfert, and N. H. Dekker, "High spatiotemporal-resolution magnetic tweezers: Calibration and applications for dna dynamics," *Biophysical Journal*, vol. 109, no. 10, pp. 2113–2125, 2015.

[91] G.-M. Nam and D. E. Makarov, "Extracting intrinsic dynamic parameters of biomolecular folding from single-molecule force spectroscopy experiments," *Protein Science*, pp. n/a–n/a, 2015.

[92] O. Itsathitphaisarn, R. A. Wing, W. K. Eliason, J. Wang, and T. A. Steitz, "The hexameric helicase dnab adopts a nonplanar conformation during translocation," *Cell*, vol. 151, no. 2, pp. 267–277, 2012.

[93] E. Enemark and L. Joshua-Tor, "Mechanism of dna translocation in a replicative hexameric helicase," *Nature*, vol. 442, no. 7100, pp. 270–275, 2006.

[94] T. Lionnet, M. Spiering, S. Benkovic, D. Bensimon, and V. Croquette, "Real-time observation of bacteriophage t4 gp41 helicase reveals an unwinding mechanism," *Proceedings of the National Academy of Sciences*, vol. 104, no. 50, pp. 19790–19795, 2007.

[95] D. Johnson, L. Bai, B. Smith, S. Patel, and M. Wang, "Single-molecule studies reveal dynamics of dna unwinding by the ring-shaped t7 helicase," *Cell*, vol. 129, no. 7, pp. 1299–1309, 2007.

[96] R. Galletto, M. Jezewska, and W. Bujalowski, "Unzipping mechanism of the double-stranded dna unwinding by a hexameric helicase: Quantitative analysis of the rate of the dsdna unwinding, processivity and kinetic step-size of the escherichia coli dnab helicase using rapid quench-flow method," *Journal of molecular biology*, vol. 343, no. 1, pp. 83–99, 2004.

[97] M. Schlierf and T. Ha, "A helicase with an extra spring in its step," *Cell*, vol. 151, no. 2, pp. 244–246, 2012.

[98] D. McIntosh and O. Saleh, "Salt species-dependent electrostatic effects on ssdna elasticity," *Macromolecules*, vol. 44, no. 7, pp. 2328–2333, 2011.

[99] O. Saleh, D. McIntosh, P. Pincus, and N. Ribeck, "Nonlinear low-force elasticity of single-stranded dna molecules," *Physical review letters*, vol. 102, no. 6, p. 68301, 2009.

[100] D. J. Kauert, T. Kurth, T. Liedl, and R. Seidel, "Direct mechanical measurements reveal the material properties of three-dimensional dna origami," *Nano letters*, vol. 11, no. 12, pp. 5558–5563, 2011.

[101] M. Akiba, K. P. Chan, and N. Tanno, "Real-time, micrometer depth-resolved imaging by low-coherence reflectometry and a two-dimensional heterodyne detection technique," *Japanese Journal of Applied Physics*, vol. 39, no. 11B, p. L1194, 2000.

[102] C. Fang-Yen, M. C. Chu, H. S. Seung, R. R. Dasari, and M. S. Feld, "Noncontact measurement of nerve displacement during action potential with a dual-beam low-coherence interferometer," *Optics letters*, vol. 29, no. 17, pp. 2028–2030, 2004.

[103] E. Pfitzner, C. Wachauf, F. Kilchherr, B. Pelz, W. M. Shih, M. Rief, and H. Dietz, "Rigid dna beams for high-resolution single-molecule mechanics," *Angewandte Chemie International Edition*, vol. 52, no. 30, pp. 7766–7771, 2013.

[104] B. Redding, Y. Bromberg, M. A. Choma, and H. Cao, "Full-field interferometric confocal microscopy using a vcsel array," *Optics letters*, vol. 39, no. 15, pp. 4446–4449, 2014.

[105] B. Redding, M. A. Choma, and H. Cao, "Speckle-free laser imaging using random laser illumination," *Nature photonics*, vol. 6, no. 6, pp. 355–359, 2012.

[106] D. S. Mehta, D. N. Naik, R. K. Singh, and M. Takeda, "Laser speckle reduction by multimode optical fiber bundle with combined temporal, spatial, and angular diversity," *Appl. Opt.*, vol. 51, pp. 1894–1904, Apr 2012.